Scholars' Mine

Masters Theses

Student Theses and Dissertations

Fall 2013

The use of elemental powder mixes in laser-based additive manufacturing

Rodney Michael Clayton

Follow this and additional works at: https://scholarsmine.mst.edu/masters_theses

Part of the Materials Science and Engineering Commons

Department:

Recommended Citation

Clayton, Rodney Michael, "The use of elemental powder mixes in laser-based additive manufacturing" (2013). *Masters Theses*. 7194.
https://scholarsmine.mst.edu/masters_theses/7194

This thesis is brought to you by Scholars' Mine, a service of the Missouri S&T Library and Learning Resources. This work is protected by U. S. Copyright Law. Unauthorized use including reproduction for redistribution requires the permission of the copyright holder. For more information, please contact scholarsmine@mst.edu.

THE USE OF ELEMENTAL POWDER MIXES IN LASER-BASED ADDITIVE MANUFACTURING

by

RODNEY MICHAEL CLAYTON

A THESIS

Presented to the Faculty of the Graduate School of the

MISSOURI UNIVERSITY OF SCIENCE AND TECHNOLOGY

In Partial Fulfillment of the Requirements for the Degree

MASTER OF SCIENCE IN MATERIALS SCIENCE & ENGINEERING

2013

Approved by

Dr. Joseph Newkirk, Advisor
Dr. Frank Liou
Dr. F. Scott Miller

© 2013
Rodney Michael Clayton
All Rights Reserved

ABSTRACT

This study examines the use and functionality of laser depositing alloys from mixes of elemental metallic powders. Through the use of laser-based additive manufacturing (LAM), near net-shaped 3-Dimensional metallic parts can be produced in a layer-by-layer fashion. It is customary for pre-alloyed powders to be used in this process. However, mixes of elemental powders can be used to produce alloys that are formed during the deposition process. This alternative technique requires that the elemental powders adequately mix during deposition for a homogeneous deposit to be produced. Cost savings and versatility are among several of the advantages to using elemental powder mixes in LAM.

Representative alloys of 316 and 430 Stainless Steel (SS) and Ti-6Al-4V were produced with elemental powder mixes during this research. These deposits were then compared to deposits of the same material manufactured with pre-alloyed powder. Comparison between the two types of samples included; EDS analysis to examine chemical homogeneity, metallography techniques to compare microstructures, and finally hardness testing to observe mechanical properties. The enthalpy of mixing is also discussed as this can impact the resulting homogeneity of deposits produced with mixes of elemental powders. Some differences were observed between the two types of deposits for 430 SS and Ti-6Al-4V. Results indicate that deposits fabricated with mixes of elemental powders can be produced to an equivalent quality of pre-alloyed powder deposits for 316 SS. This research also proposes potential alloys that could be considered for use in an elemental powder mixing technique.

ACKNOWLEDGMENTS

I would like to express my sincerest gratitude to my advisor, Dr. Joseph Newkirk. His guidance, expertise, and encouragement were vital to the success of this work. I would also like to thank my committee members Dr. Frank Liou and Dr. F. Scott Miller for their time and advice on this work.

I would like to acknowledge the members of LAMP lab for their guidance with the experimental aspects of this work and for their willingness to help. Their suggestions and assistance were critical to the completion of this work.

Finally, I would like to thank my wife, Cassie, my parents, Michael and Jean Clayton, and my sister, Kelly Clayton for their endless love and support.

TABLE OF CONTENTS

LIST OF ILLUSTRATIONS

LIST OF TABLES

Page

1. INTRODUCTION

1.1. OBJECTIVE

Laser-based additive manufacturing (LAM) is an additive manufacturing technique capable of producing 3-D near-net shape metallic parts. The LAM process uses the energy from a laser beam to form a melt pool on a substrate material. Powder is then blown into the melt pool where it leaves behind a layer of deposited material upon solidification. By depositing multiple layers of material, a 3-D part can be built layer-by-layer using this technique. Conventionally, a pre-alloyed powder is used in the LAM technique. When a pre-alloyed powder is used, each individual powder particle has the composition of the desired alloy composition in the final part. With an elemental powder mix, each individual powder particle has an elemental composition of an element present in the desired final alloy composition. Upon mixing, the sum of all powder particles gives the desired alloy composition in the final part.

One of the alloys commonly used in LAM, and is also of focus in this study, is Ti-6Al-4V. Ti-6Al-4V is one of the most used Titanium alloys and accounts for more than 50% of Titanium usage around the world. Ti-6Al-4V has applications in marine products, surgical implants, powder metallurgy products, and automotive applications but is mostly widely used for aerospace applications, which account for more than 80% of all Ti-6Al-4V usage [1]. The ability to produce near-net shape parts with LAM leads to a manufacturing process with minimal material waste. Coupled with the high cost of raw titanium, the production of Ti-6Al-4V parts through LAM becomes an attractive option. The combination of high usage volume and cost benefits of using Ti-6Al-4V in a LAM process made the alloy a great choice for examination in this study.

316 and 430 Stainless Steel (SS) were also selected for examination during this research. Many studies have already been done on the microstructure and mechanical properties of laser deposited stainless steels due to their common usage in LAM [2-4]. The large number of different grades of stainless steels results in materials with similar compositions but a wide range of properties and uses. This versatility works well with LAM, since the process is compatible with many different materials.

Ultimately, this study hoped to produce deposits of 316 and 430 SS and also Ti-6Al-4V using elemental powder mixes that were of similar quality to deposits of the same material made with pre-alloyed powder. To confirm quality, chemical homogeneity, microstructure, and mechanical properties were examined and compared in the two types of deposits. Additionally, one of the goals of this study was to determine a potential number of alloys that could be produced through a small stock of element powders. Alloys systems containing Fe-Cr-Ni and Ti-Al-V were considered for selection.

1.2. BACKGROUND

Takeda et. al. investigated three possible methods of depositing Fe-Cr-Ni alloys with elemental powder mixes [5]. One of these methods was to deliver premixed powder with a single powder feeder and pipe, which is the same type of method that is used in this study. Ultimately, results of the study indicated that it was possible to deposit these Fe-Cr-Ni alloys with an elemental powder mix method. However, under certain process parameters a severe lack of homogeneity occurred. Takeda noted that when travel speed was greater than a critical value, a homogenous deposit was not possible and concluded this was a result of the melt time, or, the time the material was molten during deposition. The use of an elemental powder mix requires that the powder particles adequately mix during the deposition process or a homogeneous deposit cannot be produced. Results of this study indicate that, given appropriate process parameters, a homogeneous deposit can be produced using elemental powder mixes. Should any lack of homogeneity be observed during the course of this study, the travel speed and corresponding melt time may need to be considered.

Elemental powder mixes are also a direct benefit to the ability to laser deposit functionally graded materials (FGM's). FGM's are a material with a graded composition, microstructure, or mechanical properties that change from one end of the deposit to the other. When composition is graded, the deposit typically contains 100% material "A" at the start and 100% material "B" at the end, typically having a 50/50 A/B mixture in the middle. The most basic FGM is graded from one elemental material to another elemental material, however, much more complex FGM's could be imagined. These deposits are most often produced with multiple powder feed hoppers delivering the differing powders into the melt pool where the powders are mixed. The principles of successfully depositing an alloy through a mix of elemental powders are therefore very similar to successfully depositing a FGM.

Common production of FGM's involves grading from one metallic material to another, however this is not the only possibility. FGM's manufactured with elemental powder mixes also allows for the ability to produce composite materials using a LAM technique. Liu and DuPont showed that a TiC/Ti composite material that was graded from pure titanium to TiC could be produced using a LAM method [6]. This ability to grade from a ceramic to a metallic material bridges the gap between the toughness of metals and wear-resistance of ceramics. Materials with these types of properties are possible through the production of a FGM and the use of an elemental powder mixes in LAM. In work done by R. Banerjee et. al., Ti-6Al-4V-TiB composites were produced with the aid of elemental powder mixes [7]. This work involved mixing a pre-alloyed Ti-6Al-4V powder with elemental boron powder. Unlike the work done by Liu and DuPont, these composites had a homogenous mixture throughout the deposit. Results indicated that a deposit with an α/β matrix of Ti-6Al-4V with fine precipitates of TiB could be produced. These types of metal-matrix composites can be produced with other manufacturing methods, but the ability to produce them with LAM using elemental powder mixes has potential.

1.3. ENTHALPY OF MIXING

Previous experiments performed using elemental powders during laser deposition indicate that the enthalpy of mixing is critical in being able to make a homogenous deposit [8, 9] . The enthalpy of mixing of the alloy being deposited can be negative (exothermic) or positive (endothermic). In the case of a negative enthalpy of mixing, additional heat is supplied to the melt pool during the mixing of the elemental powders aiding in the homogenization of the resulting deposit. For the case of a positive enthalpy of mixing, heat is extracted from the melt pool making mixing and homogenization more difficult.

K. I. Schwendner et. al. examined the effect of enthalpy of mixing of two binary alloys produced with elemental powders. The two systems they chose were Ti-10%Cr with an enthalpy of mixing of -12.6 kJ/g atom and Ti-10%Nb with an enthalpy of mixing of +4.2 kJ/g atom. By using similar process parameters during deposition, a direct comparison of the enthalpy of mixing on the results could be determined. The results of the study indicate that a positive enthalpy of mixing leads to segregation of materials, while the negative enthalpy of mixing leads to a very homogenous mixture. K.I. Schwendner et. al. also examined the effect enthalpy of mixing had on the resulting microstructure of the deposit. By making a first approximation, they assumed the solidification rate to be proportional to the temperature difference between the melt pool and the surrounding substrate. Under this assumption, an alloy with a negative enthalpy of mixing would have a higher melt pool temperature and therefore a higher solidification rate. Microstructures of their deposits confirmed these results indicating that a negative enthalpy of mixing leads to a rapidly solidified microstructure.

In work done by P.C. Collins et. al. an elemental powder mix technique was used during the laser deposition of complex titanium alloys. Materials used in this study included Timetal 21S along with a modified Timetal 21S where molybdenum was replaced with chromium. The chromium modified Timetal 21S was chosen to increase the enthalpy of mixing in the alloy due to the more negative enthalpy of mixing value of titanium-chromium than titanium-molybdemum. While enthalpy of mixing was examined, the energy density used during deposition was of more focus. The results of this study indicate that with an adequate energy density, a homogeneous deposit can be produced. However, below a critical energy density, a deposit microstructure will show un-melted or segregated particles. A negative enthalpy of mixing is equivalent to increasing the energy density, in a sense that both lead to increased heat input into the melt pool. These observations confirm the idea that a negative enthalpy of mixing is likely required to produce a homogeneous deposit using mixes of elemental powders.

Enthalpies of mixing of the materials used in this study are summarized in Table 1.1. These enthalpy of mixing values were calculated based on an extended regular solution model developed by Takeuchi and Inoue [10, 11]. Equation (1) shows the equation upon which this model is based, where c_i and c_j are the composition of the i-th and j-th elements respectively.

$$\Delta H_{mix} = \sum_{\substack{i=1 \\ i \neq j}}^{3} \Omega_{ij} \, c_i \, c_j \tag{1}$$

From Meidema's macroscopic model, Ω_{ij} is the regular solution interaction parameter between i-th and j-th elements and has the relation $\Omega_{ij} = 4 \times \Delta H_{AB}^{mix}$. Of the alloys examined in this study, Ti-6Al-4V has the most negative enthalpy of mixing. This negative value is due to the impact of the ΔH^{mix} of titanium-aluminum being equal to -30 kJ/mol. The highly negative interaction between these two elements ultimately leads to a more negative enthalpy of mixing in the alloy. ΔH^{mix} of titanium-vanadium and aluminum-vanadium have values of -2 and -16 kJ/mol respectively. Stainless steel alloys on the other hand, have an enthalpy of mixing that is only slightly negative. This is the result of only slightly negative values of ΔH^{mix}, between elemental pairs, in stainless steel alloys. For perspective, ΔH^{mix} of iron-chromium, iron-nickel, and chromium-nickel have values of -1, -2, and -7 kJ/mol respectively. Examining these values it can be seen that a larger amount of chromium and nickel would further decrease the enthalpy of mixing in the alloy. However, the total weight percent of these two elements combined is 29 wt% for 316 SS and only 17 wt% for 430 SS and explains why the 316 SS enthalpy of mixing is lower than the 430 SS enthalpy of mixing. The only slightly negative enthalpy of mixing of 430 SS is due to its composition consisting solely of iron and chromium. The very small enthalpy of mixing value for this alloy could result in mixing and homogenization issues during deposition using mixes of elemental powders.

Table 1.1. Calculated Enthalpies of Mixing for Alloys Used in This Study

Material	**Enthalpy of Mixing (kJ/mol)**
316 SS	-1.72
430 SS	-0.59
Ti-6Al-4V	-11.0

2. EXPERIMENTAL PROCEDURE

2.1. POWDER CHARACTERIZATION

Pre-alloyed powders used in this study were 316L SS, 430 SS, and Ti-6Al-4V. These alloys were obtained from Carpenter Technology, Alloy Metals, Inc., and ASM powders respectively. Elemental powders consisted of iron, chromium, and nickel for representative stainless steel samples as well as titanium and an aluminum/vanadium master alloy for Ti-6Al-4V samples. The elemental powders used in this study were characterized to confirm information provided from suppliers but also to determine particle shape and/or size in some cases. By understanding the size distribution and shape of particles, observations and any findings in deposits could potentially be correlated with particle shape or size. Images were taken using a Hitachi S4700 SEM and image analysis was performed using ImageJ software.

2.1.1. Elemental Iron Powder. Iron powder, grade ASC100.29, used in the deposition of stainless steel alloys was purchased from North American Hoganas and was listed as 99.9% pure. Table 2.1 shows the manufacturers specifications for the size of the iron powder. This shows that the majority of iron particles should have a size less than -70 mesh (<210 μm) size. Figure 2.1 shows an SEM micrograph used in the analysis of the iron powder. To determine particle size, particles were analyzed using automatic particle analysis software included with ImageJ. By adjusting the image properties, the software only calculated the area of the individual powder particles. From the area calculation, a particle diameter was determined based on a spherical shape. As seen in Figure 2.1 the iron particles have more of an irregular shape than a spherical shape, but this calculation allowed for the determination of an approximate particle size. Analysis of 23 particles from Figure 2.1 and similar micrographs, found an average particle size of -200/+325 mesh (74-44 μm) size. The particles had a distribution of 4 particles -140/+200 mesh (105-74 μm) size, 14 particles -200/+325 mesh (74-44 μm) size, and 5 particles -325 mesh (<44 μm) size. Even though this analysis was only a small sample of the iron powder, it is clear that the powder has a relatively small size, which correlates well with the manufacture’s size designations.

Table 2.1. North American Hoganas Specifications for Iron Powder

Mesh Size	Percentage	Physical Size (µm)
-70/+80	1.5%	-210/+177
-80/+100	6.2%	-177/+149
-70/+100	7.7%	-210/+149
-100/+140	15.6%	-149/+105
-140/+200	18.6%	-105/+74
-200/+325	28.4%	-74/+44
-325	29.7%	-44

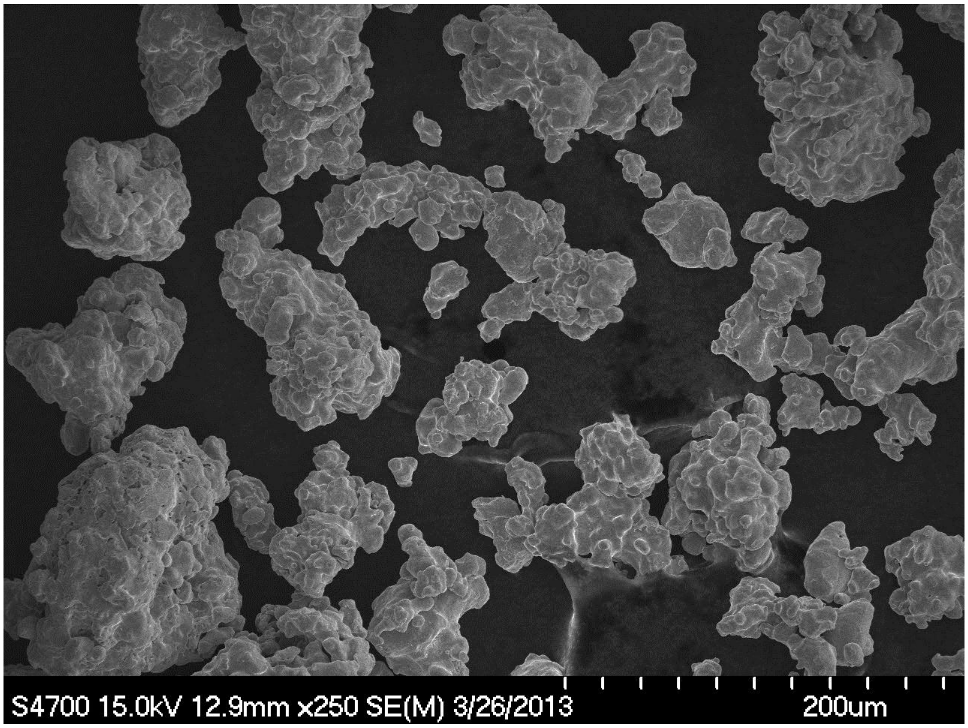

Figure 2.1. SEM Micrograph of Multiple Iron Powder Particles

2.1.2. Elemental Nickel Powder. Nickel powder, purchased from Alfa Aesar, was listed as having a -100/+200 mesh (149-74 µm) size and 99.9% purity. Measurements were done on an isolated particle, which can be seen in Figure 2.2, to determine the particle size. Measurements were taken in the vertical, horizontal, and two diagonal directions, which resulted in an average length of 130 µm. This size is well within the designated -100/+200 mesh (100-74 µm) size. To get a better idea of the average particle size, several images similar to that of Figure. 2.3 were taken of nickel powder particles. The automatic particle analysis software in ImageJ was again used to calculate the area of individual powder particles. After analysis of these images, an average particle diameter of 105 µm was determined. Again this particle size fits within the manufacturers designated mesh size. It should also be noted that nickel powder particles have a mostly spherical shape when compared to the iron powder particles.

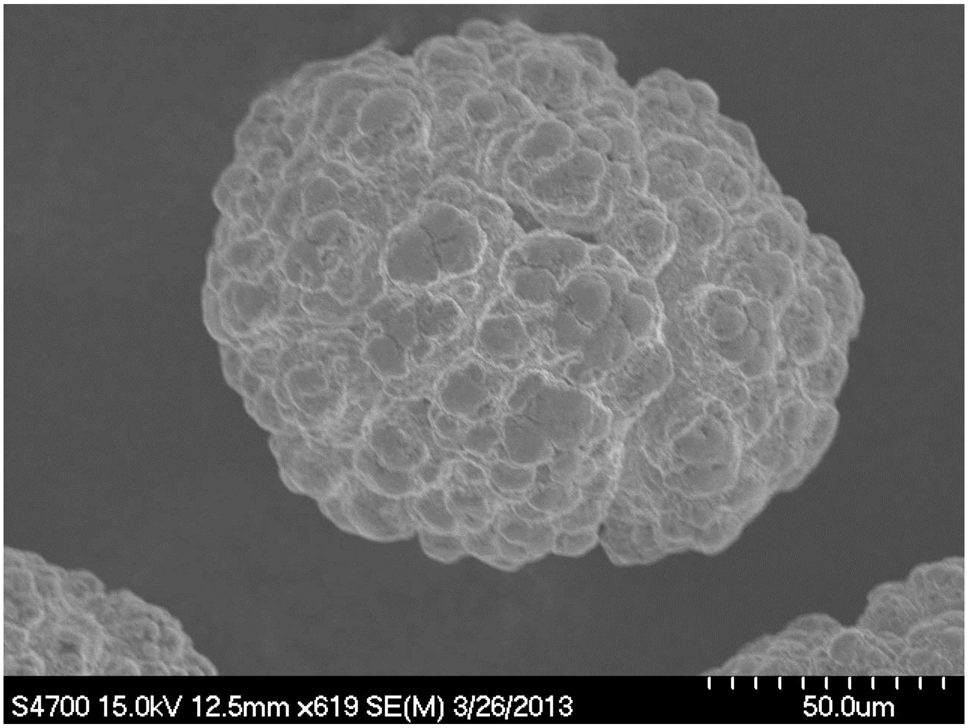

Figure 2.2. SEM Micrograph of an Isolated Nickel Powder Particle

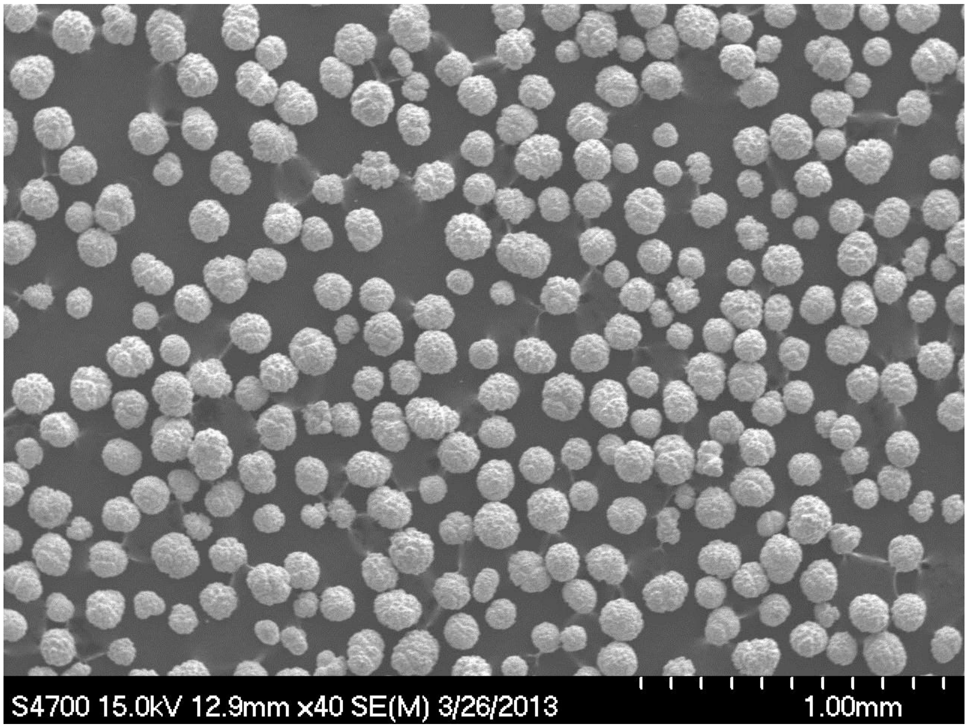

Figure 2.3. SEM Micrograph of Multiple Nickel Powder Particles

2.1.3. Elemental Chromium Powder. Chromium powder, grade ATCR-S9-74XD, was purchased from F.W. Winter Inc. and manufactured using an aluminothermic technique to produce chromium powder of 99% purity. As seen in Figure 2.4 this results in chromium particles with a very angular shape. The chromium powder was designated as being 100% -60 mesh (<250 μm) size and 25% maximum -325 mesh (<44 μm) size. From Figure 2.4 this can be seen with the range of very small particles to much larger particles. A plot of the size distribution can be seen in Figure 2.5 and shows that particles in the -140/+170 mesh (105-88 μm) size have the highest frequency. Confirming this observation, the average particle size was determined to be 96 μm, which falls in the size range of a -140/+170 mesh (105-88 μm) size. The mesh size distribution also shows that there are some particles with a -325 mesh (<44 μm) size, but only a small quantity of particles fall in this size range. Further analysis of the particle distribution proved that only about 7% of particles analyzed were below a 325 mesh (<44 μm) size. This result confirmed the manufacturer's specifications that less than 25% of particles could be below a 325 mesh (<44 μm) size.

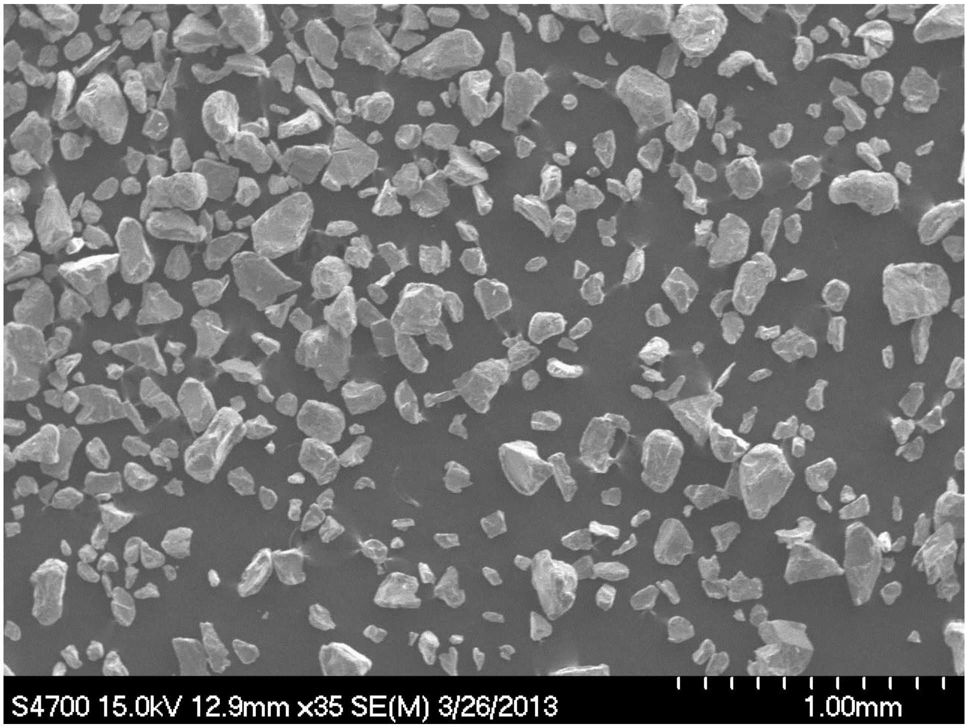

Figure 2.4. SEM Micrograph of Chromium Powder Particles

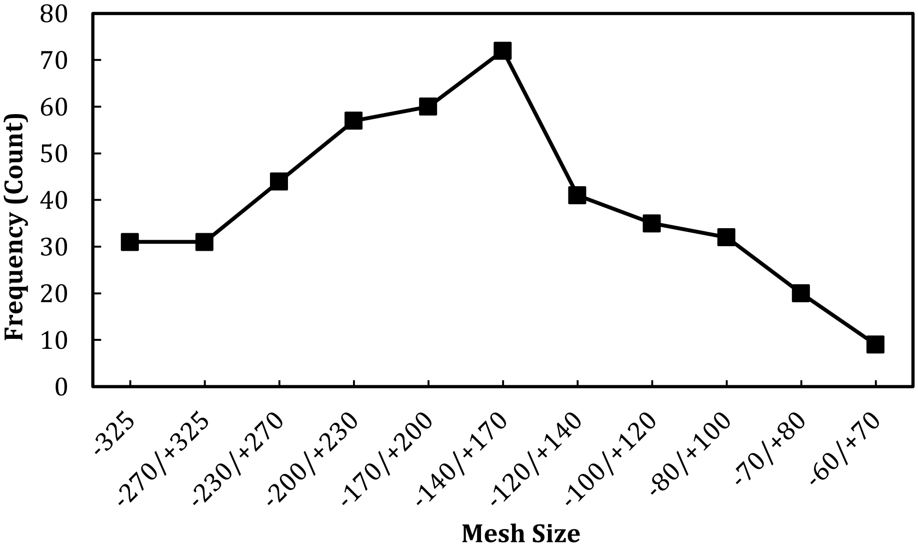

Figure 2.5. Size Distribution of Chromium Powder Particles

2.1.4. Elemental Titanium Powder. Titanium powder, grade Ti-109, was purchased from Atlantic Equipment Engineers for use in deposition of Ti-6Al-4V alloys. This powder was listed as being 99.7% and of -100 mesh (<149 µm) size. A SEM micrograph of the titanium powder can be seen in Figure 2.6 and a very complex particle shape is observed. This complex shape makes it difficult for the automatic particle analysis software in ImageJ to accurately outline individual particles and calculate a correct area. The outline of individual particles after image analysis can be seen in Figure 2.7. Comparing Figure 2.6 and Figure 2.7, there are instances where particles are not correctly outlined or one particle is believed to be multiple particles by the software. Although the analysis may not give precise measurements, trends in particle size and distribution can be observed. From the resulting software analysis, an average particle size of 64 µm was determined. Figure 2.8 shows the titanium powder distribution by mesh size and confirms that the powder is -100 mesh (<149 µm) size. An average particle size of 64 µm is indicative of a -200/+230 mesh (74-63 µm) size and correlates well with the particle distribution. With the slight errors of the image analysis software during analysis of titanium powder, it is reasonable to believe that the average particle size is slightly larger than 64 µm and the number of particles below a 325 mesh (<44 µm) size is not as high.

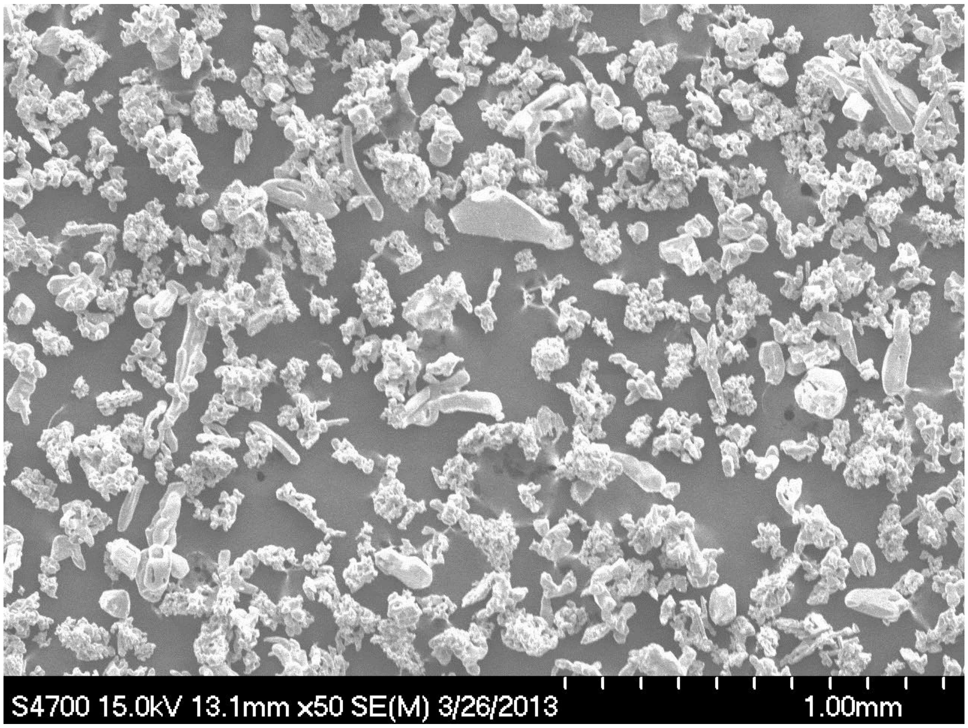

Figure 2.6. SEM Micrograph of Titanium Powder Particles

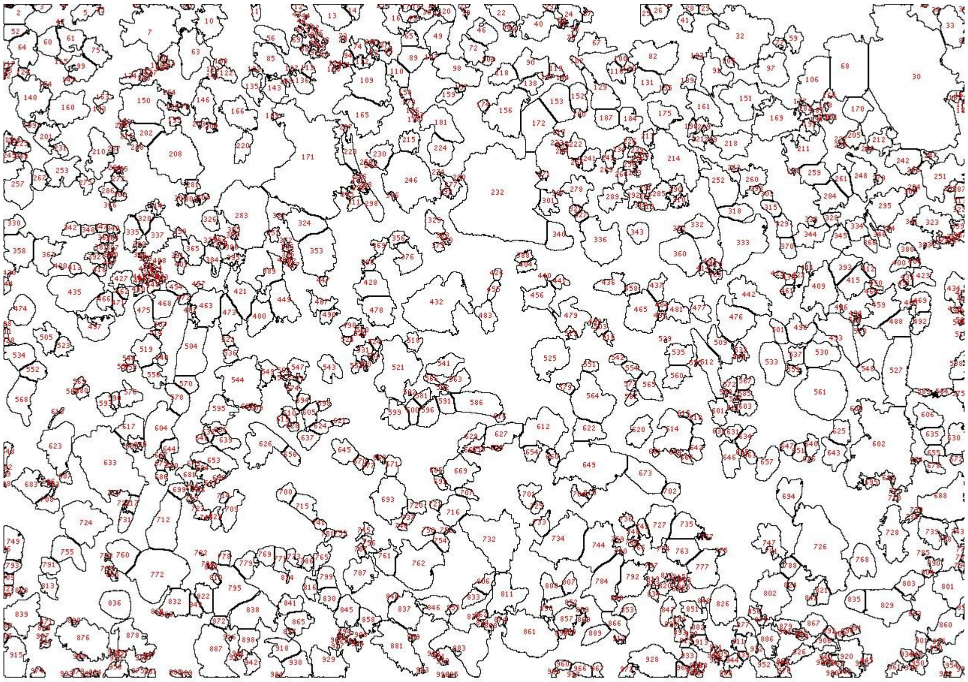

Figure 2.7. Outlined Titanium Powder Particles After Automatic Particle Analysis in ImageJ

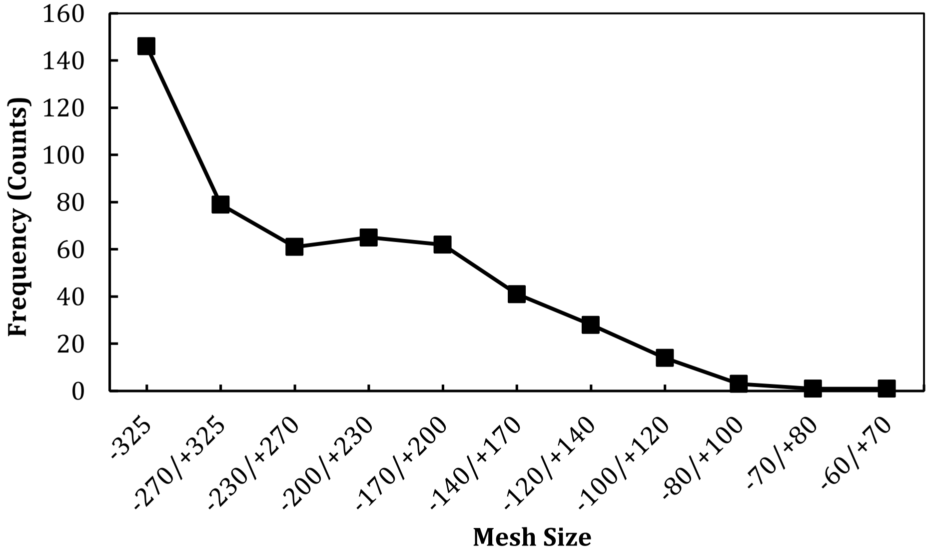

Figure 2.8. Size Distribution of Titanium Powder Particles

2.1.5. Aluminum/Vanadium Master Alloy Powder. A 60Al/40V master alloy powder was purchased from Reading Alloys with a size designation of -60/+120 mesh (250-125 µm) size. This master alloy, grade ES074-1, is the product of a thermite reaction and therefore has a very angular shape, which can be seen in Figure 2.9. The powder was listed as having a chemical composition of 58.18% aluminum and 41.31% vanadium from the manufacturer. From Figure 2.10, it can be seen that of the particles analyzed, the majority are +140 mesh (>105 µm) size. However, this indicates that at least some particles are in the -120/+140 mesh (125-105 µm) range, which is below the manufacturers size designation. The range between a 120 and 140 mesh particle is just 20 µm. This is a very tight tolerance and a small error or fluctuation in the analysis software could lead to some -120 mesh (<120 µm) size particles. It is also important to note that number of particles below -140 mesh size significantly decreases. Therefore, even if a small percentage of -120/+140 mesh size particles do exist they should not have an impact on the experiment.

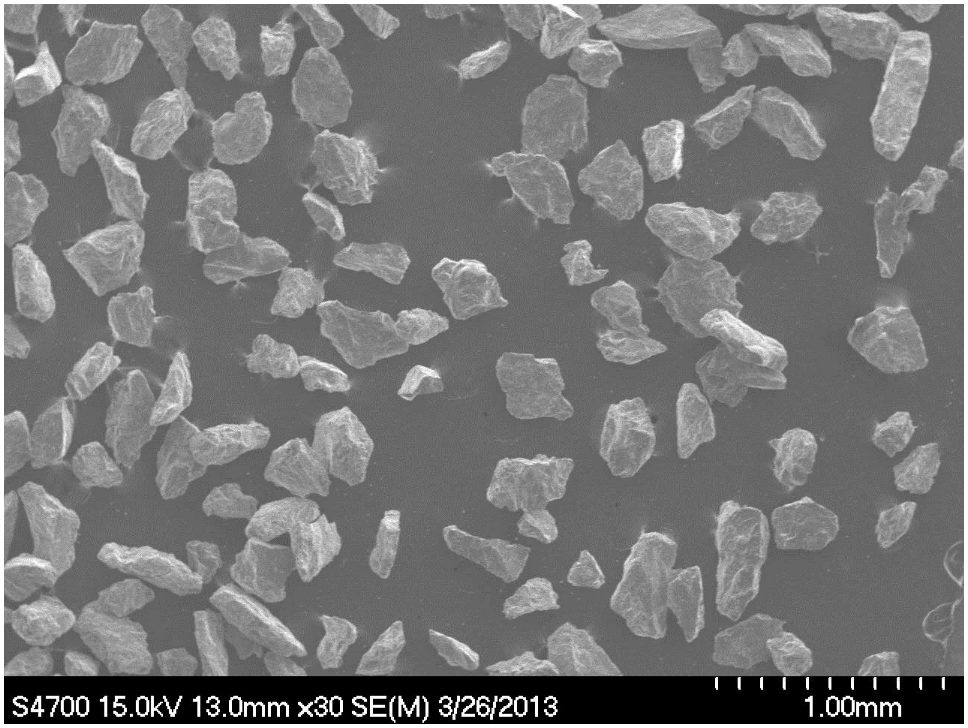

Figure 2.9. SEM Micrograph of Al/V Master Alloy Powder Particles

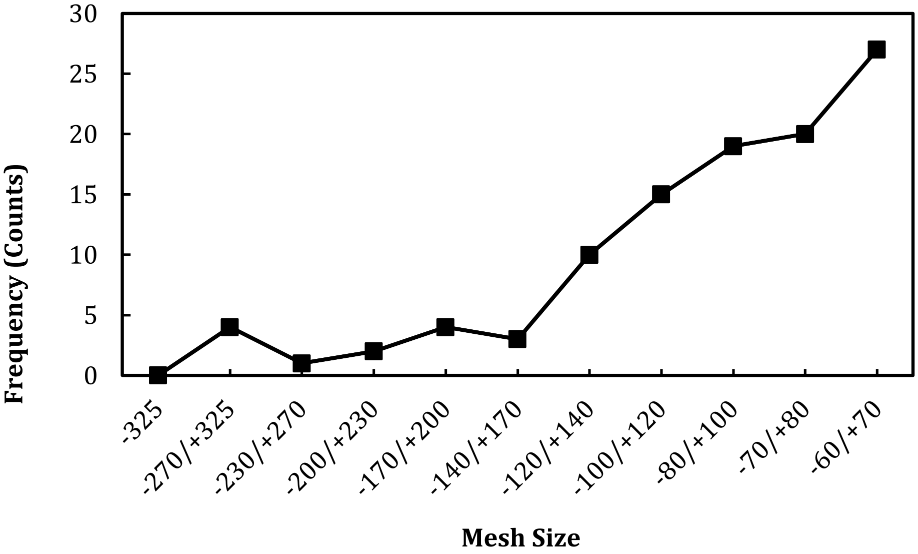

Figure 2.10. Size Distribution of Al/V Master Alloy Powder Particles

2.2 PRE-DEPOSITION

The three alloys of focus were a representative 316 SS (Fe-17Cr-12Ni), a representative 430 SS (Fe-17Cr), and Ti-6Al-4V. To serve as a control and comparison in the experiments, deposits were also made using a pre-alloyed powder of each of the alloys of interest. Before the deposition process began, the elemental powder mixes were prepared. Powders were weighed out according to desired alloy composition in a glove box under an argon atmosphere and placed in a sealed bottle. After the desired composition was obtained, the bottle was placed in a turbula mixer and mixed for 20 minutes.

2.3. DEPOSITION

The deposition of alloys studied in this work was performed using a 1kW Nd:Yag laser with a wavelength of 1024 nm and a spot size of approximately 1mm at a 750 mm focal length. A schematic of the laser deposition process can be seen in Figure 2.11. For this study thin wall samples were deposited on a substrate material. Stainless steel alloys and Ti-6Al-4V deposits were made on 304 SS substrates and Ti-6Al-4V substrates respectively. All substrates were 2” long, ½” wide, and ¼” thick. Track length for each deposit was 25 mm. Prior to deposition with powder, a cleaning pass was made with the laser on at full power with no powder flow. This cleaning pass served to remove any contaminants on the surface of the substrate. The deposition process, with powder, began immediately following the cleaning pass.

It had previously been determined, that to produce deposits of relatively uniform dimensions from top to bottom using this laser deposition system, laser power must be varied during the deposition process. To accurately control laser power, a system using a feedback sensor was developed. The system operates by first detecting the number of photons coming off of the orange colored region near the melt pool. Although the photons could be measured coming directly off the melt pool, this region is much smaller than the orange colored region and potentially could lead to inconsistencies with the sensor. By focusing on the orange colored region, a larger region that is still proportional to melt pool size can be detected. The number of photons detected is converted to an integer value between 0 and 1024. Before deposition begins, the system is given a desired set-point also in the range of 0 to 1024. During deposition, the feedback sensor will turn up laser power if a reading less than the set-point is determined or alternatively, turn down laser power if a higher value is found. Since a larger orange colored region is proportional to a larger melt pool, the set-point served as an excellent experiment variable. Therefore, to either promote or inhibit mixing in deposits using mixes of elemental powders, the set-point was either increased or decreased respectively.

With the feedback sensor set-point serving as a quality experimental variable, efforts were made to minimize any other experimental variables between the deposition of pre-alloyed and mixed elemental powders. Therefore, while depositing the same material, every effort was made to keep deposition parameters of travel speed, powder feed rate, and layer thickness constant from test to test. This would allow for the best comparison between a deposit produced using pre-alloyed powder and a deposit produced through an elemental powder mix. In some cases slight variations had to be made to one or more of the deposition parameters but changes were kept to a minimum. When changing from material to material (i.e. 316 SS to 430 SS), the deposition parameters were required to change to produce successful deposits. The exact parameters used for each sample produced can be found in the results section for each material (Section 3.1, 3.2, and 3.3).

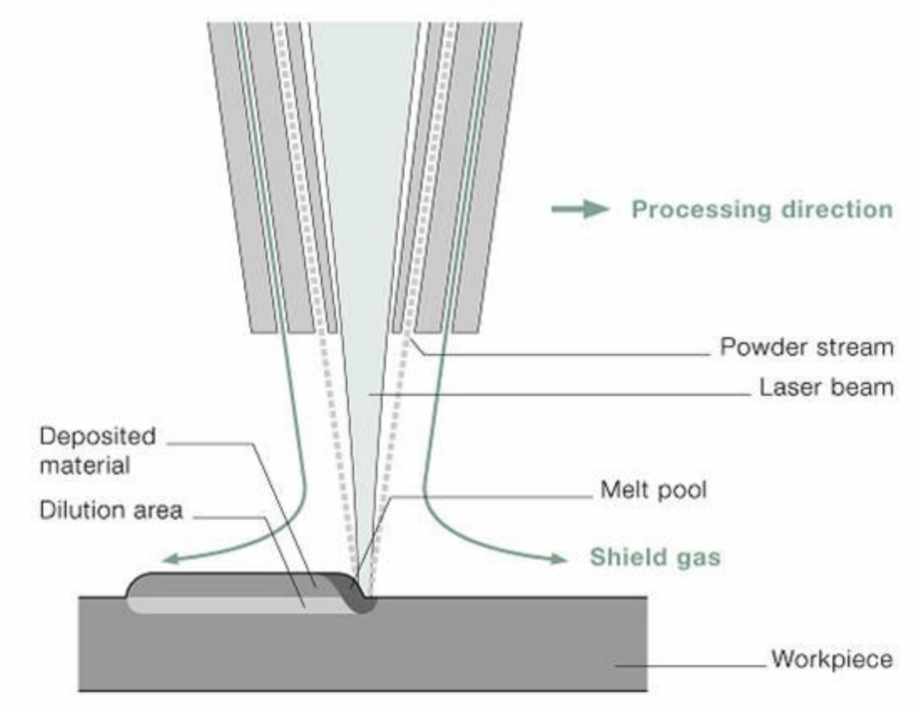

Figure 2.11. Schematic Diagram Used to Represent the LAM Process

2.4. POST DEPOSITION

After deposition, deposited material was sectioned from the substrates using a precision cut-off saw and then sectioned in half to make analysis easier. Following a Struers metallography guide, samples were surface mounted for grinding and polishing procedures. To examine microstructure characteristics in stainless steel samples, a Methanolic Aqua Regia etchant was used consisting of 27 ml HCl, 9 ml HNO_3, and 12 ml Methanol. For Ti-6Al-4V samples, Kroll's Reagent consisting of 92 ml distilled H_2O, 6 ml HNO_3, and 2 ml HF was used for etching. Using a Hitachi S4700 and FEI Helios 600 scanning electron microscopes (SEM), energy dispersive spectroscopy (EDS) line scans were performed to examine composition in both pre-alloyed and mixed elemental powder deposits. Optical micrographs were also taken of samples to compare microstructure features in pre-alloyed and mixed elemental powder samples. To examine and compare mechanical properties between the two types of samples, Vickers hardness measurements were taken with a Struers Duramin micro-hardness tester. Loads of 50 g and 500 g were used during testing with a dwell time of 5 seconds.

3. RESULTS AND DISCUSSION

3.1. 316 STAINLESS STEEL

Using parameters that were known to produce successful 316 SS deposits, two deposits were made using pre-alloyed powder. These two deposits would serve as controls during testing and it was hoped to match mixed elemental powder deposits to these samples. Table 3.1 summarizes physical dimensions, process parameters used, and powder type for each 316 SS sample produced. Measurements did not include any influence from the substrate material and were only based on the size of the deposit. The height of the deposit was measured in the vertical direction and width was measured in the horizontal direction. Figure 3.1 (a-f) and Figure 3.2 (a-f) show plots of Laser Power vs. Time during the deposition process and the Average Laser Power per Layer vs. Layer Number during the deposition process, respectively. These plots all show that initially the laser power starts off at maximum power but slowly starts to decrease until a near steady-state laser power is reached.

The first noticeable difference between pre-alloyed and mixed elemental powder deposits is that the same set-point produces a deposit of much different physical dimensions. Using the same set-point of 175 with an elemental powder mix produces a deposit that is shorter and much thinner than a deposit using a pre-alloyed powder at the same set-point. When comparing plots in Figure 3.1 and 3.2 (a and b) (pre-alloyed deposits) to plots in Figure 3.1 and 3.2 (c) (elemental powder mix deposits) a much lower steady-state laser power is reached for the mixed elemental powder deposits. This lower laser power would lead to less energy input into the deposit and therefore a shorter and thinner deposit would be produced. It should be noted that under ideal conditions a higher energy input into the deposit would be desired than what was observed in Sample #3.

With an energy input this low, the deposition quality becomes poor. It is likely that the difference in powder types is leading to the change in laser power between mixed elemental powder deposits and pre-alloyed deposits. As mentioned in the powder characterization section, the iron, chromium, and nickel powder particles had an irregular shape. This irregular shape may lead to more reflection of laser light than what was observed in pre-alloyed powders. The higher reflection of laser light would have resulted in the feedback sensor thinking the deposit was hotter than it actually was, i.e. larger orange colored region, resulting in a decreased laser power to reach the desired set-point.

As the set-point was increased with mixed elemental powder deposits, physical dimensions became similar to those of the pre-alloyed control tests. Sample #5 with a set-point of 300 produced a mixed elemental powder deposit with the closest dimensions to those of the pre-alloyed deposits. Not surprisingly, the steady-state laser power reached in Sample #5 is very similar to the steady-state laser power reached in Samples #1 and #2. It is interesting to note that Sample #6 with the highest set-point actually had a shorter height but was much thicker than the pre-alloyed deposits. The set-point used in this test was likely too high, causing the deposit to become too hot. As the temperature of the deposit increases, more and more previously deposited layers are re-melted and it becomes difficult to increase deposit height. This leads to a deposit that is thicker and shorter than the same deposit that did not reach as high of a temperature. To produce a deposit of similar physical dimensions of Sample #1 and #2 using an elemental powder mix technique, a set-point of approximately 300 should be used.

Table 3.1. Process Parameters and Deposit Dimensions for 316 SS

	Sample #1	**Sample #2**	**Sample #3**	**Sample #4**	**Sample #5**	**Sample #6**
Powder Type:	Pre-Alloyed	Pre-Alloyed	Mixed	Mixed	Mixed	Mixed
Set-Point:	175	175	175	190	300	500
# of Layers:	70	70	70	70	90	70
Layer Thickness: (mm)	0.25	0.25	0.25	0.25	0.25	0.25
Travel Speed: (mm/s)	7.5	7.5	7.5	7.5	7.2	7.5
Powder Feed Rate: (RPM)	2.5	2.5	2.5	2.5	2.5	2.5
Height: (mm)	19.22	19.17	18.87	19.32	19.12	18.69
Width: (mm)	25.07	24.86	24.25	24.62	24.7	25.2
Thickness: (mm)	1.95	1.89	1.57	1.64	1.94	2.4

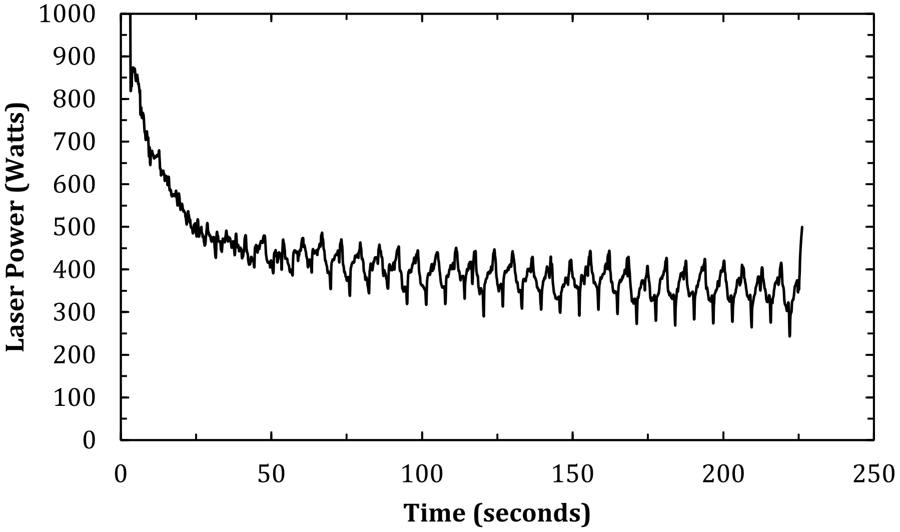

(a)

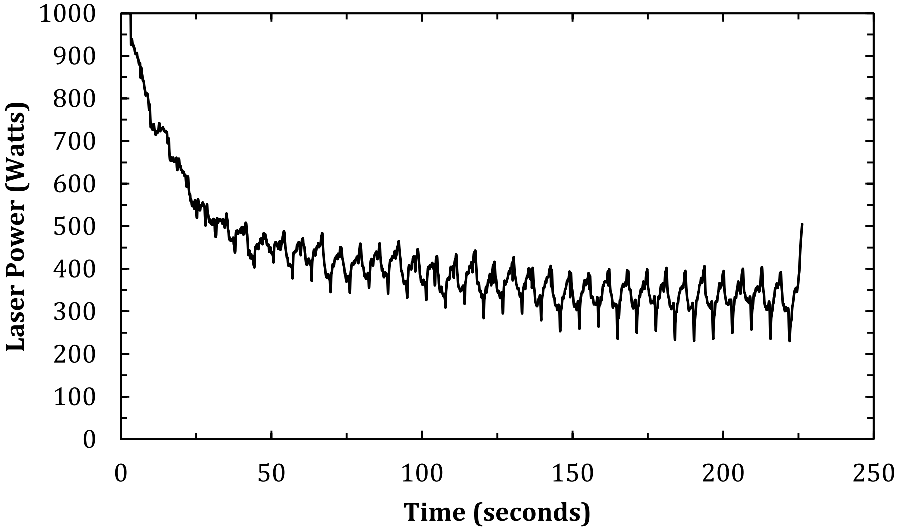

(b)

Figure 3.1. Plots of Laser Power vs. Time for 316 SS Deposits (Figures (a-f) represent 316 SS sample # 1-6 respectively)

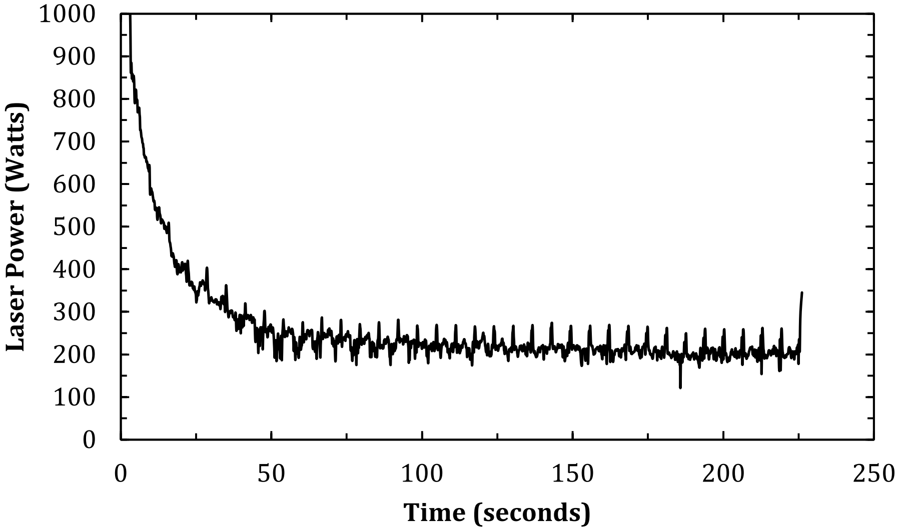

(c)

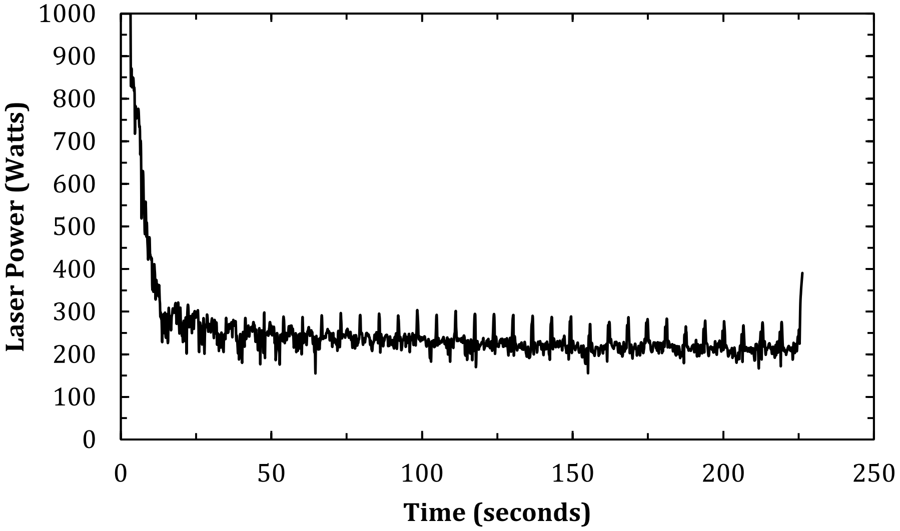

(d)

Figure 3.1. Plots of Laser Power vs. Time for 316 SS Deposits (Figures (a-f) represent 316 SS sample # 1-6 respectively) (cont.)

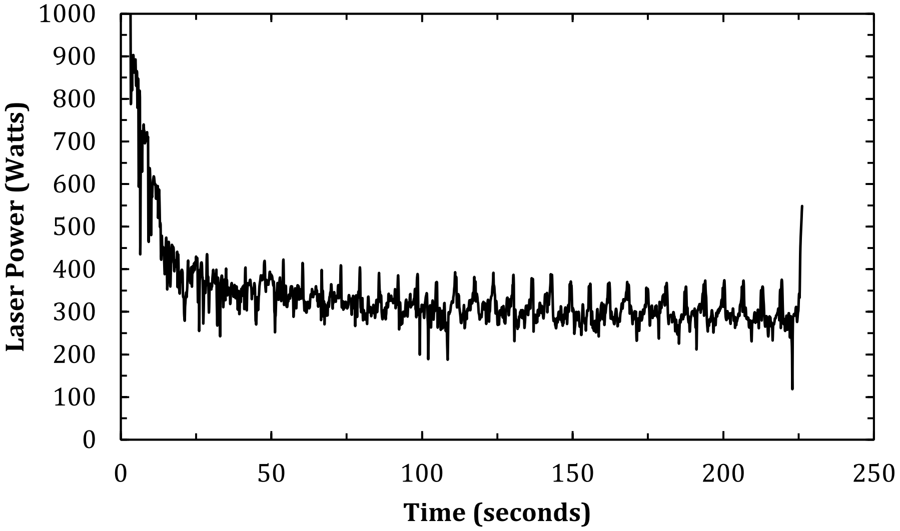

(e)

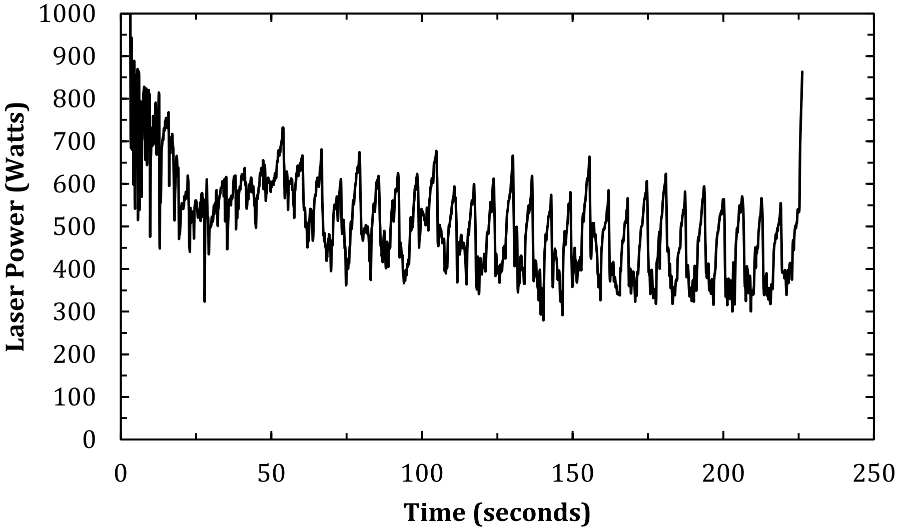

(f)

Figure 3.1. Plots of Laser Power vs. Time for 316 SS Deposits (Figures (a-f) represent 316 SS sample # 1-6 respectively) (cont.)

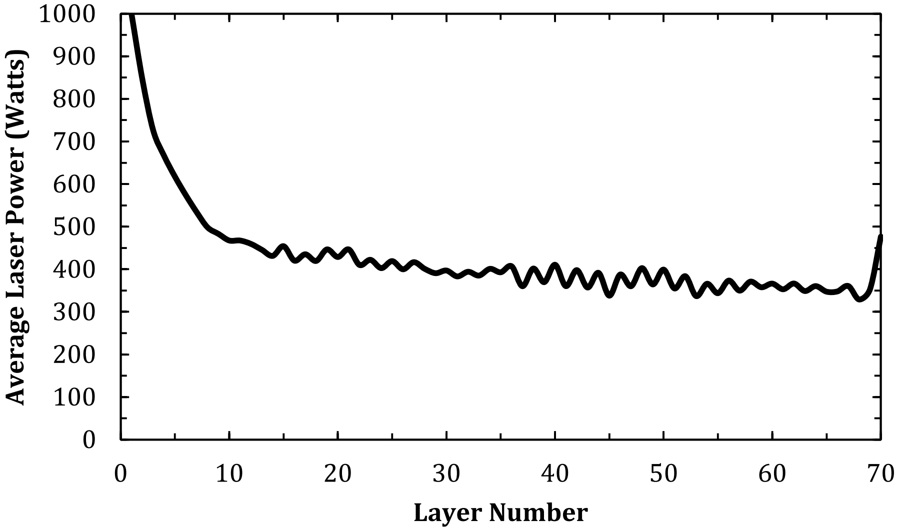

(a)

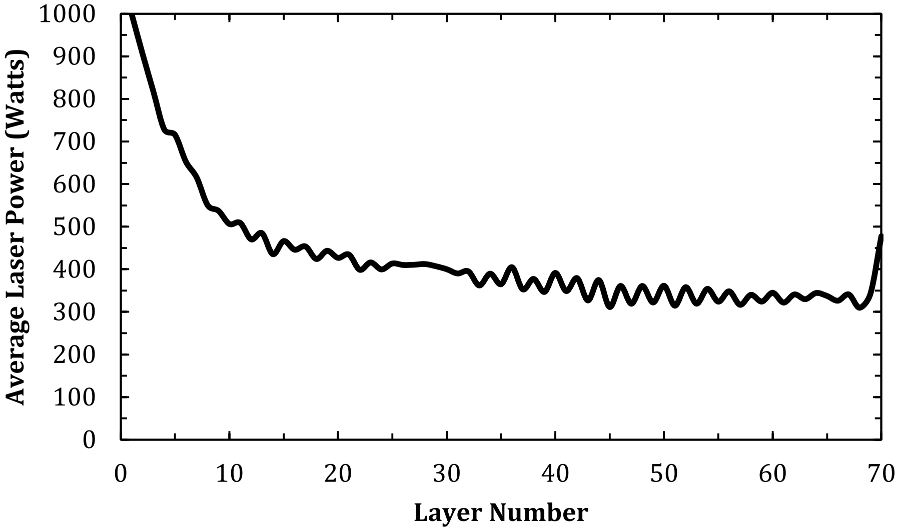

(b)

Figure 3.2. Plots of Average Laser Power per Layer vs. Layer Number for 316 SS Deposits (Figures (a-f) represent 316 SS samples # 1-6 respectively)

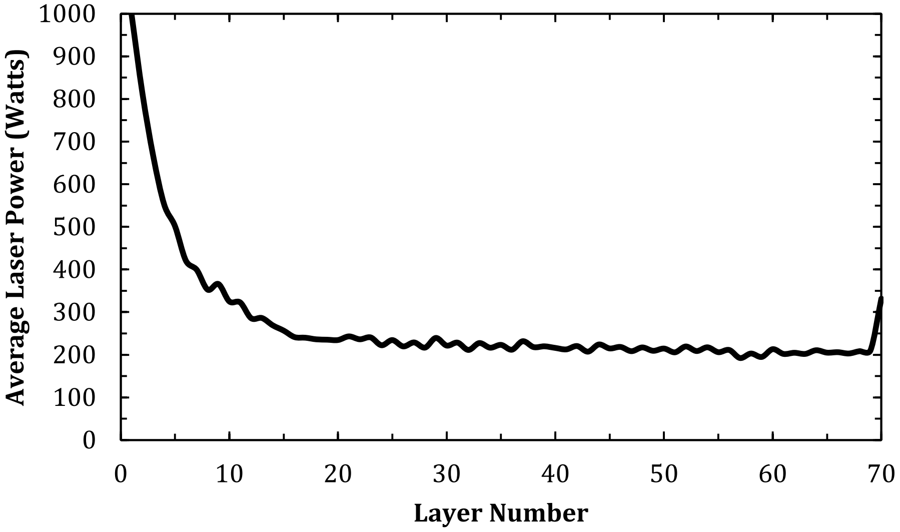

(c)

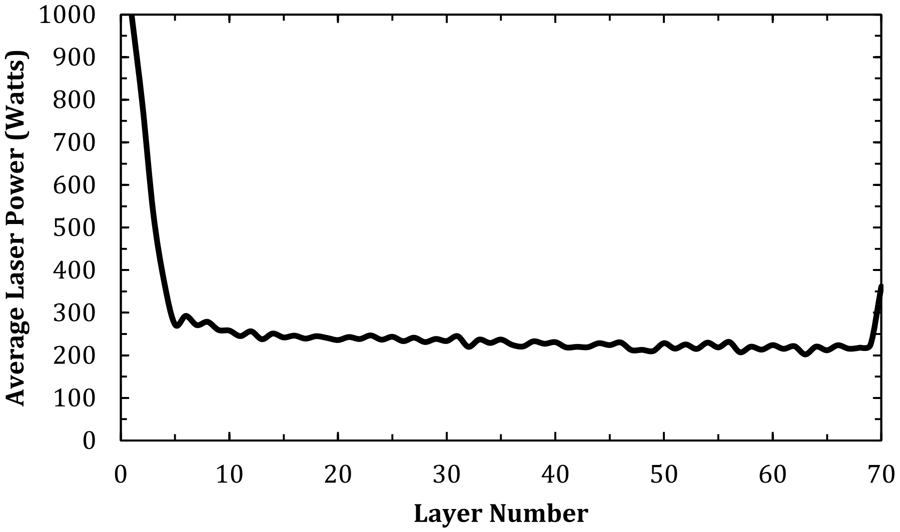

(d)

Figure 3.2. Plots of Average Laser Power per Layer vs. Layer Number for 316 SS Deposits (Figures (a-f) represent 316 SS samples # 1-6 respectively) (cont.)

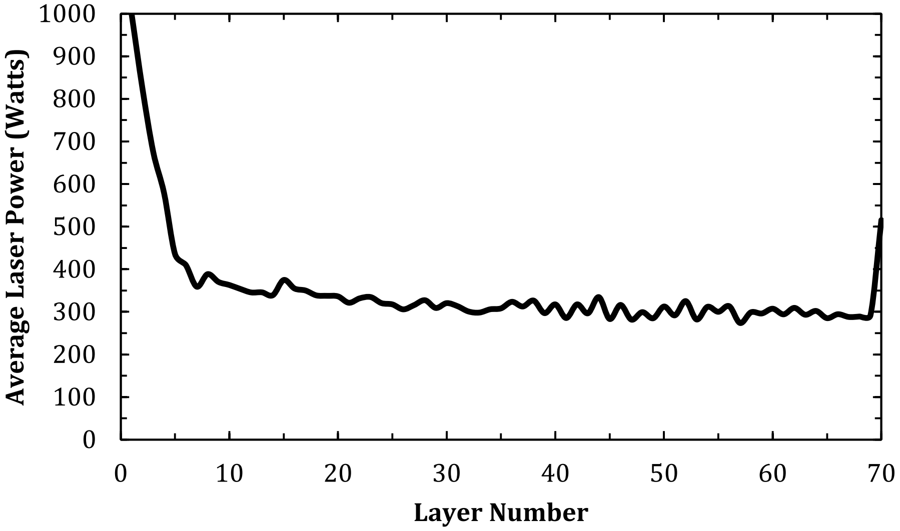

(e)

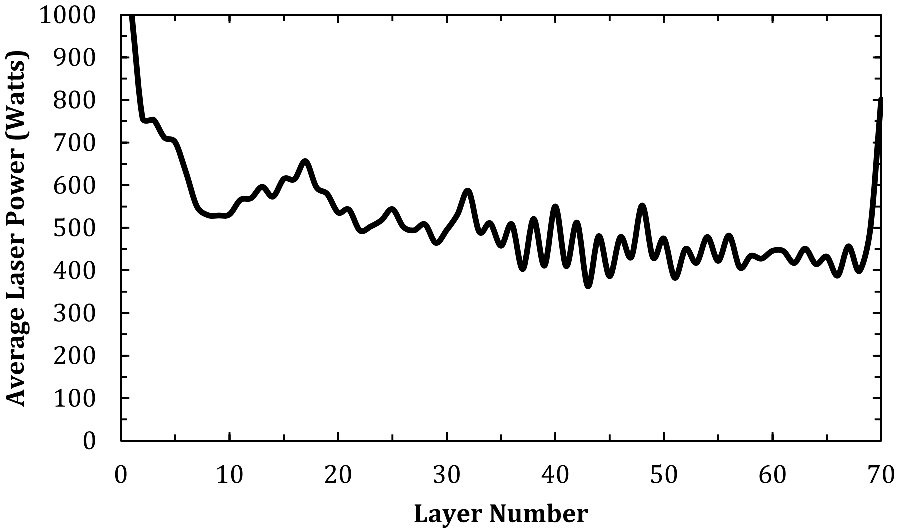

(f)

Figure 3.2. Plots of Average Laser Power per Layer vs. Layer Number for 316 SS Deposits (Figures (a-f) represent 316 SS samples # 1-6 respectively) (cont.)

3.1.1. EDS Analysis. The next step in evaluating the success of deposits using an elemental powder mix technique was to confirm chemical homogeneity. EDS line scans were performed across different areas of samples to examine the fluctuation in chemical composition. Figures 3.3 – 3.5 show the results of EDS line scans for 316 SS deposits. Image (a) in these Figures shows the area where the line scan was performed, while (b) shows the results of the EDS analysis. A homogeneous chemical composition was indicated by a line scan that showed minimal fluctuation in counts for each element. In the 316 SS deposits, only counts of iron, chromium, and nickel were examined since they would be the only elements present in the deposits produced with elemental powder mixes.

As expected, the pre-alloyed deposits (Figure 3.3) had a consistent number of counts indicating a homogeneous composition. As previously mentioned, the energy input into Sample #3 was quite low with the set-point used. This led to a sample with very poor deposition quality and deposition with an even lower set-point likely would have led to deposition failure. Since the energy input was low, it is very possible that this would have made it difficult for all of the elemental powders to adequately mix. Of all the samples deposited using mixed elemental powders, this would have been the sample that produced an inhomogeneous mixture. However, as Figure 3.4 shows, the results of the EDS line scan on Sample #3 appear to indicate a homogeneous composition throughout the deposit. There is more variation in counts for each element than what was observed with the pre-alloyed deposit, but this variation is not enough to say that an inhomogeneous deposit was produced. As Figure 3.5 shows, as the set-point is increased further even less variation in composition can be observed and the results resemble that of a pre-alloyed deposit.

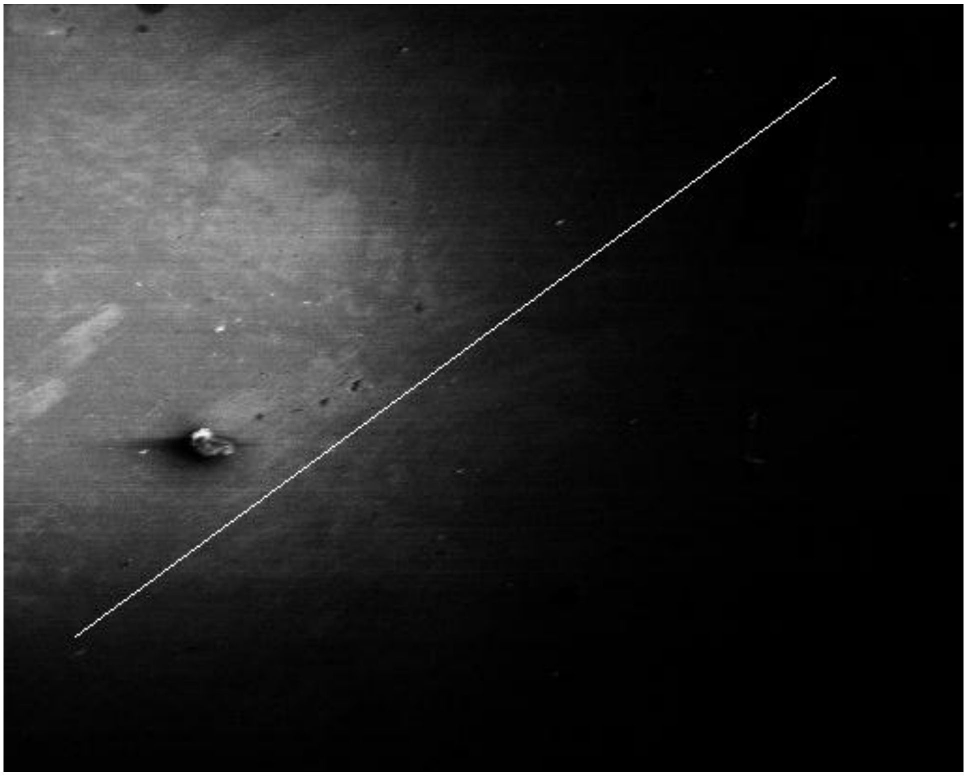

(a)

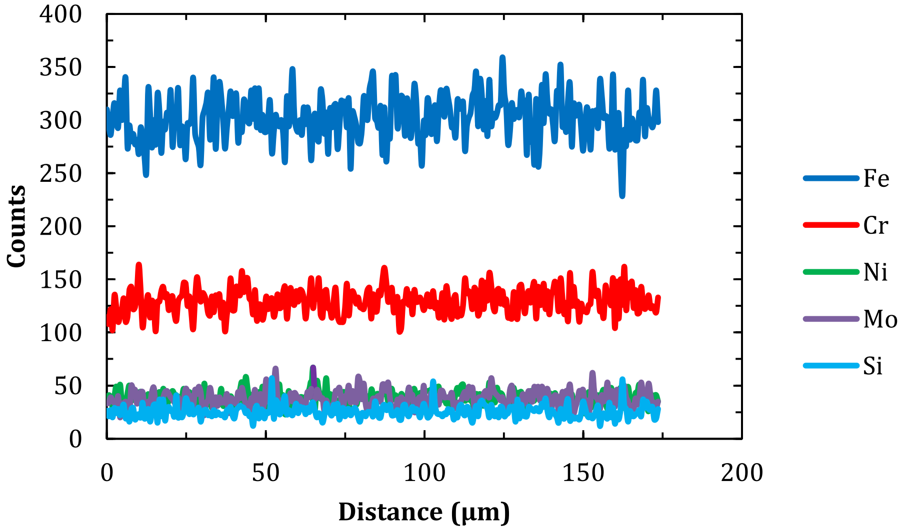

(b)

Figure 3.3. (a) EDS Line Scan Area and (b) Line Scan Results from 316 SS Sample #1

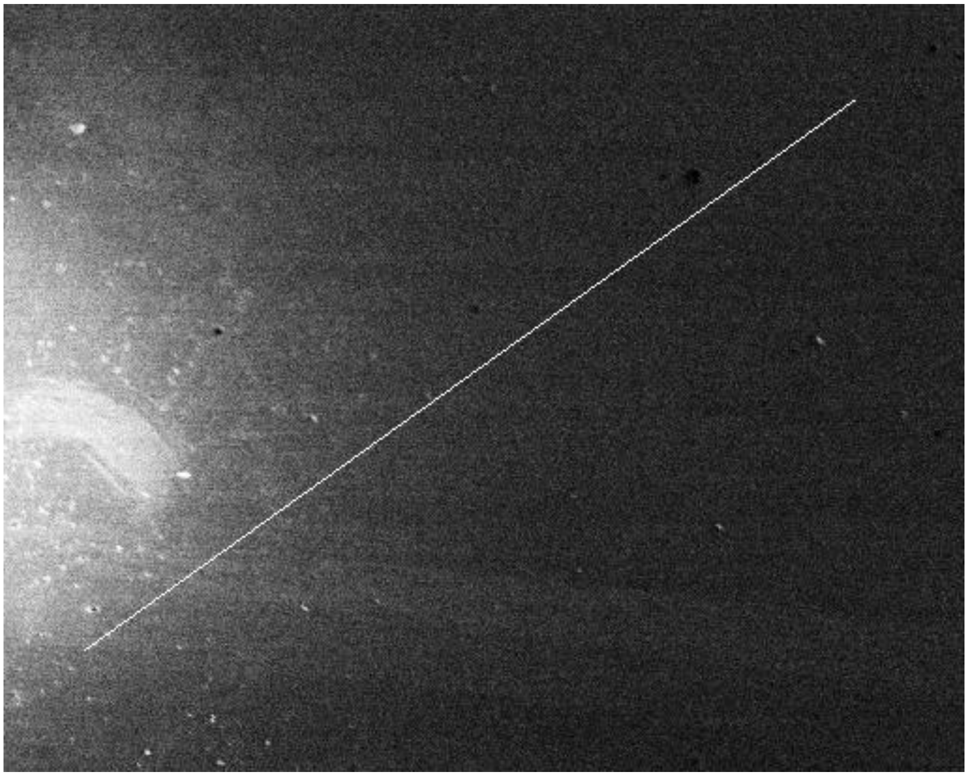

(a)

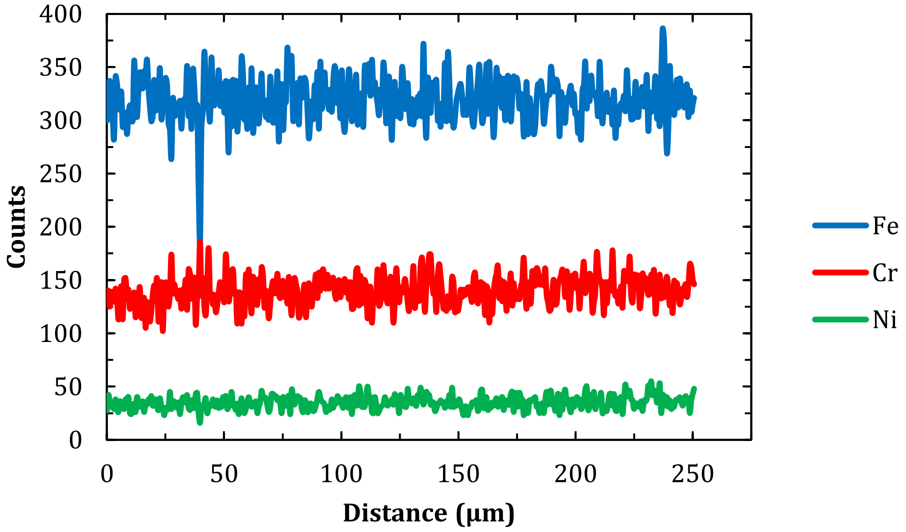

(b)

Figure 3.4. (a) EDS Line Scan Area and (b) Line Scan Results from 316 SS Sample #3

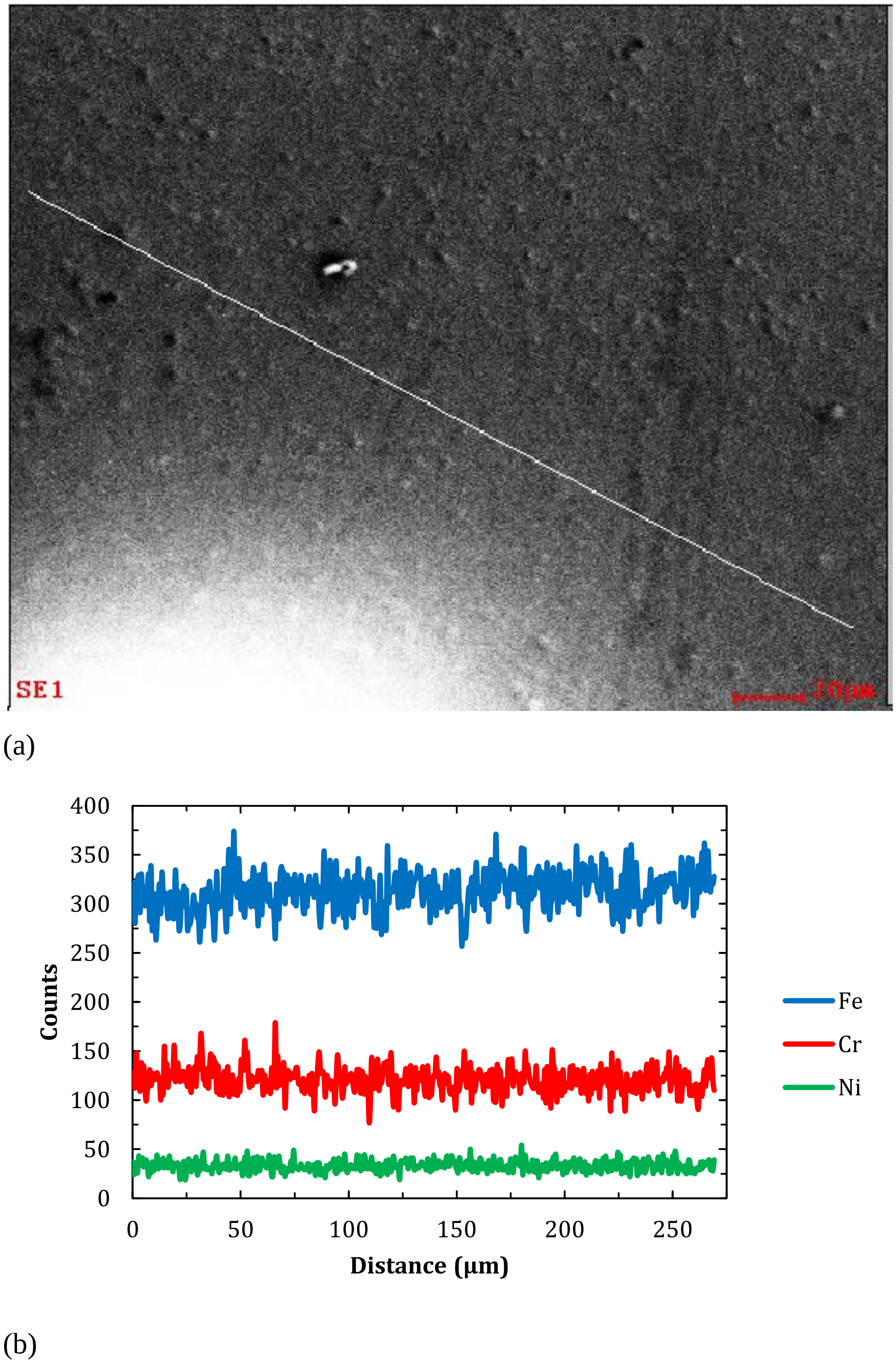

Figure 3.5. (a) EDS Line Scan Area and (b) Line Scan Results from 316 SS Sample #6

3.1.2. Microstructure Analysis. Once it was confirmed that both pre-alloyed and mixed elemental powder deposits contained a homogeneous composition, a microstructure analysis was performed. As described in Section 2.4 the samples were polished, etched, and then examined under an optical microscope. Figure 3.6 shows the microstructure observed (a) in a pre-alloyed 316 SS deposit and (b) in a mixed elemental powder deposit. A cellular structure is present in the microstructure of both types of deposits, which is consistent with literature results [12].

The 17-12 Cr-Ni ratio in 316 SS leads to either a single-phase austenite or a primary austenite with second-phase ferrite solidification mode. Under high cooling rates, single-phase austenite solidification is characterized by the formation of arrays of austenite cells. Under low cooling rates, single-phase austenite solidification can also occur but is characterized by the formation of a dendritic structure. Given that solidification rates in laser-based additive manufacturing are much higher than conventional manufacturing methods, the presence of arrays of austenite cells in the microstructure of both types of deposits is as expected.

Consistent microstructures in both types of samples are indicative of similar compositions, temperature profiles, and cooling rates. By carefully weighing out the elemental powder mixes, efforts were made to maintain similar compositions. Although it was more difficult to control temperature profiles and cooling rates between the two samples, it would appear that similar conditions were present. This control was possible through making slight changes in the set-point of the deposition system between the two types of powder. The similar microstructure between the pre-alloyed deposits and the mixed elemental powder deposits confirms control of composition, temperature profiles, and cooling rates in 316 SS experiments.

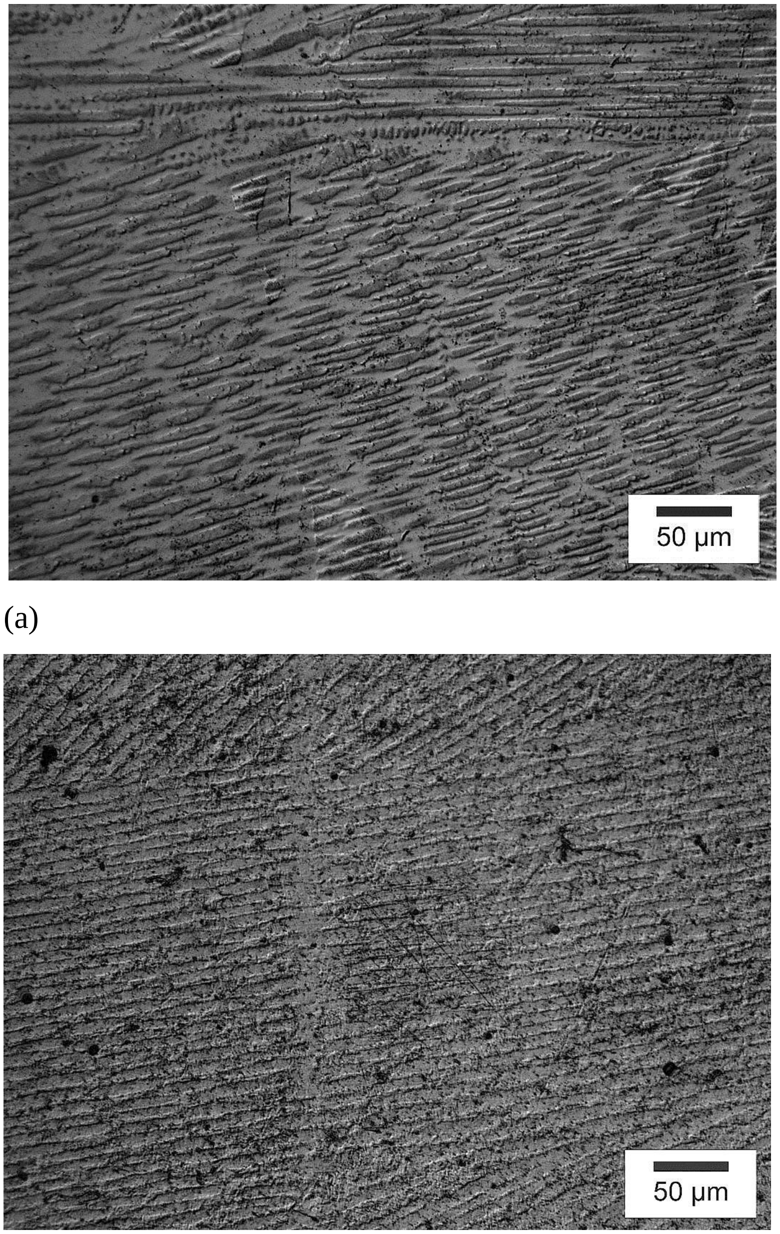

(a)

(b)

Figure 3.6. (a) Optical Micrograph of 316 SS Pre-Alloyed Powder Deposit and (b) Mixed Elemental Powder Deposit Microstructure

3.1.3. Mechanical Properties. To examine mechanical properties of deposits made with elemental powder mixes, Vickers microhardness measurements were made and compared to measured values from pre-alloyed deposits. Figure 3.7 is a representative image of the various positions where microhardness measurements were taken in the deposits. Given the variation in deposit size from material to material, this image only shows approximate locations. Figure 3.8 (a) and (b) shows plots of microhardness values with respect to position in the deposit when measured with a (a) 500 g load and (b) 50 g load, both with dwell times of 5 seconds. Pre-alloyed deposits had a microhardness of 155±4 VHN and mixed elemental powder deposits had a microhardness of 235±50 VHN when measured with a 500 g load and a dwell time of 5 seconds. When microhardness with a 50 g load was measured, the hardness of the "cellular" structure and "matrix" was examined. In pre-alloyed deposits, the cellular structure had a hardness of 183±24 VHN and the matrix had a hardness of 184±16 VHN. The cellular structure in mixed elemental powder deposits had a hardness of 235±40 VHN while the matrix had a hardness of 230±60 VHN. These values are similar to values reported in previous studies of laser deposited 316 SS [13].

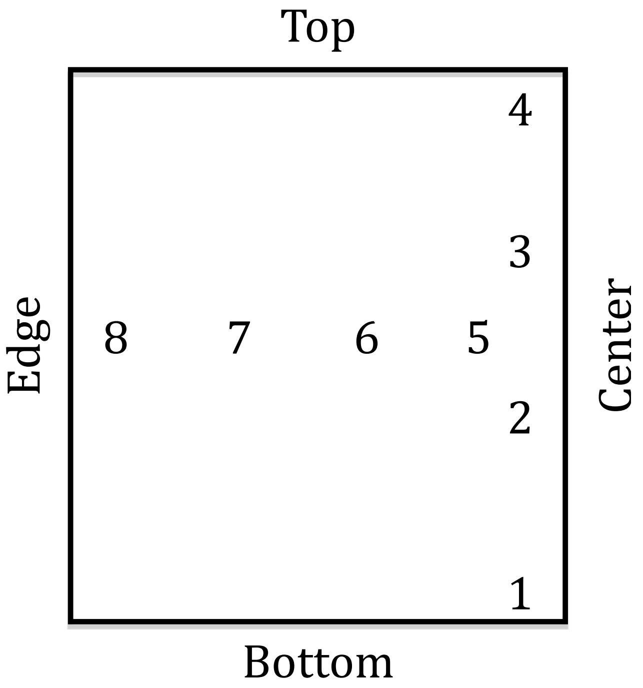

Figure 3.7. Diagram Showing the Locations Where Hardness Measurements Were Taken

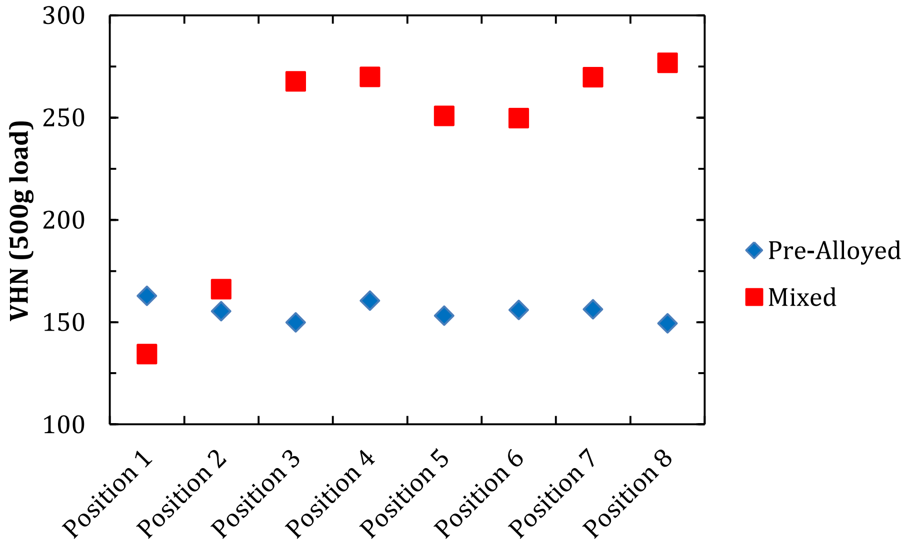

(a)

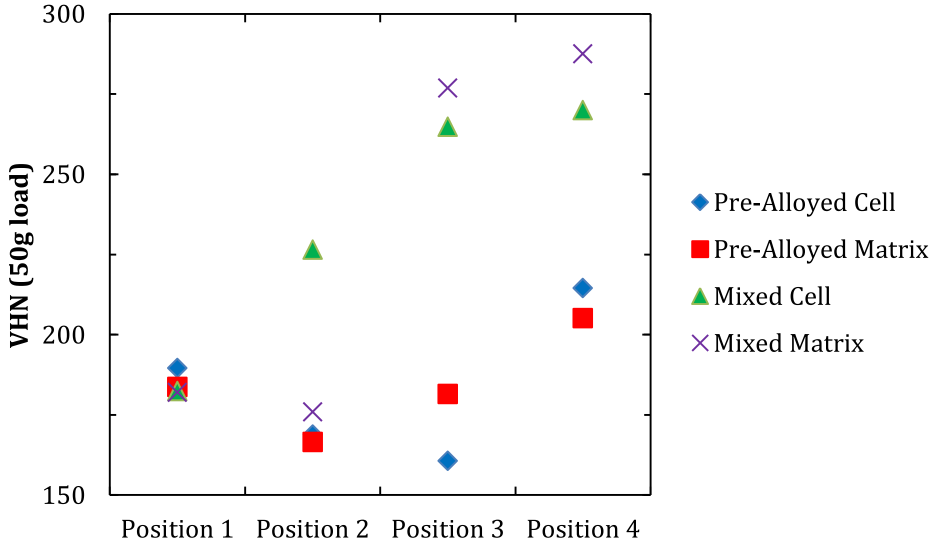

(b)

Figure 3.8. (a) Plot of Vickers Hardness vs. Position for Pre-Alloyed and Mixed Elemental Powder 316 SS Deposits Measured with a 500 g Load and (b) 50 g Load

Neither pre-alloyed deposits nor mixed elemental deposits showed trends to indicate that hardness changed with respect to location in deposit. The variation in hardness values between the two types of deposits can be attributed to slight differences in processing conditions. Although efforts were made to insure that deposits with both types of powder saw similar heat inputs, the different powders may have had differing absorption rates of laser power. This difference could lead to variations in cooling rate and ultimately, to the slight variations observed in hardness values between pre-alloyed and mixed elemental deposits. To combat possible variations in processing temperatures, deposits made with both types of powder were subjected to an annealing treatment following ASTM standards at 1075 °C for 1 hour and a subsequent water quench. Assuming similar compositions in the deposits, both types of deposits would exhibit similar hardness values following the annealing treatment. Figure 3.9 shows the hardness values for the post-processed pre-alloyed deposits and mixed elemental powder deposits. Following the annealing treatment, pre-alloyed deposits exhibited a hardness of 154±5 VHN while mixed elemental powder deposits exhibited a hardness of 152±9 VHN. In a worst-case scenario, these results indicate that pre-alloyed and mixed elemental 316 SS deposits can be post-processed to exhibit similar mechanical properties.

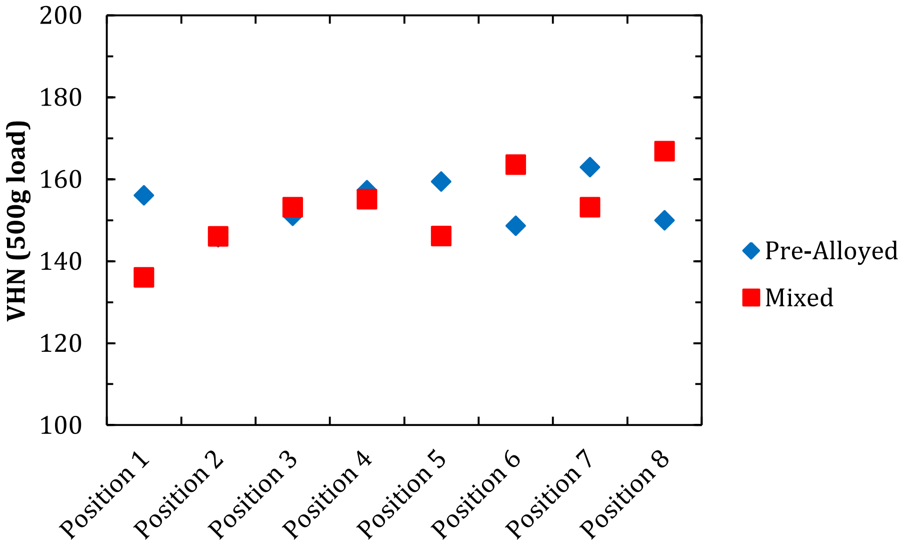

Figure 3.9. Plot of Vickers Hardness vs. Position for Pre-Alloyed and Mixed Elemental Powder 316 SS Deposits Following an Annealing Treatment at 1075 °C for 1 Hour and a Water Quench

3.2. 430 STAINLESS STEEL

As with 316 SS experiments, two pre-alloyed 430 SS deposits were made to serve as experimental controls. Table 3.2 lists the set-point, process parameters used, and deposit dimensions for five samples of pre-alloyed and mixed elemental powder 430 SS. It should be noted that measurements for Sample #3 are not present. The parameters used during that deposition lead to a poor quality deposit and measurements were not taken. The low set-point that was used, lead to a laser power that did not input enough energy into the deposit. This made it difficult for powder to contact a very small melt pool and generate layer build up. One difference between 430 SS experiments and 316 SS experiments is that the number of layers of deposited material changed from pre-alloyed to mixed elemental powder deposits. The desired deposit height was approximately 22 mm. With the pre-alloyed powder, this was achieved with 100 layers of deposited material. However, only 90 layers were required to achieve this same deposit height with an elemental powder mix. The mixed elemental powder deposits also had a tendency to be much thicker than the pre-alloyed deposits. This could be a result of the higher set-point used but comparing the plots in Figure 3.10 and Figure 3.11 (a-d), the steady-state laser power reached at the highest set-point with an elemental powder mix (d) does not exceed the steady-state laser power reached in the pre-alloyed powder deposits (a and b). Therefore, it is unlikely that the higher set-point is causing the deposit to reach a higher temperature and produce a thicker deposit.

Figure 3.12 shows a visual comparison between a pre-alloyed 430 SS deposit and a deposit produced using an elemental powder mix. The deposit produced using an elemental powder mix has a darker color due to a slightly larger oxide layer on its surface than what was observed with a pre-alloyed deposit. This larger oxide layer leads to mixed elemental powder deposits that are thicker than deposits made using pre-alloyed powder. Although there is some oxide on the surface, any part produced in an additive manufacturing technique will require some minimal amount of machining. The surface oxide observed on the mixed elemental powder deposits would be removed during this process and no decrease in part quality would be observed.

Table 3.2. Process Parameters and Deposit Dimensions for 430 SS

	Sample #1	**Sample #2**	**Sample #3**	**Sample #4**	**Sample #5**
Powder Type:	Pre-Alloyed	Pre-Alloyed	Mixed	Mixed	Mixed
Set-Point:	125	125	125	200	300
# of Layers:	120	100	90	90	90
Layer Thickness: (mm)	0.2	0.2	0.2	0.2	0.2
Travel Speed: (mm/s)	7.2	7.2	7.2	7.2	7.2
Powder Feed Rate: (RPM)	3.5	3.5	3.5	3.5	3.5
Height: (mm)	24.95	22	N/A	21.45	22.04
Width: (mm)	24.92	24.35	N/A	24.74	24.91
Thickness: (mm)	2.1	1.98	N/A	2.52	2.3

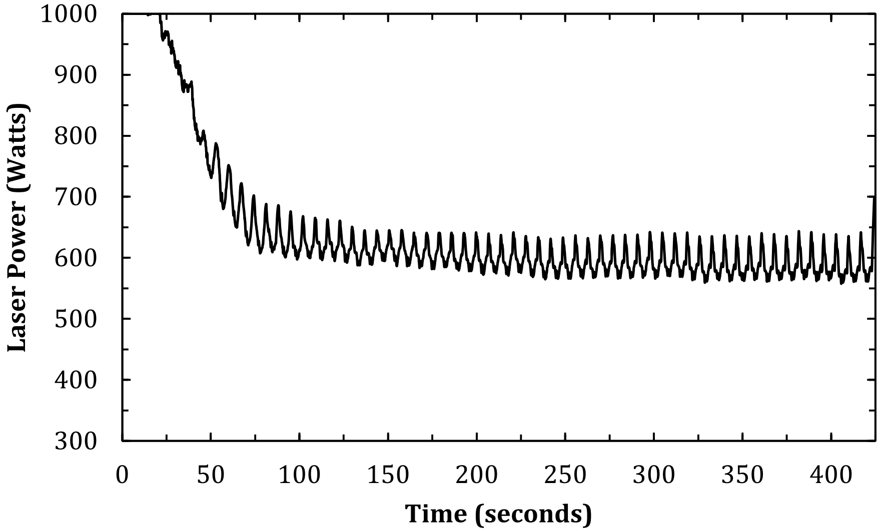

(a)

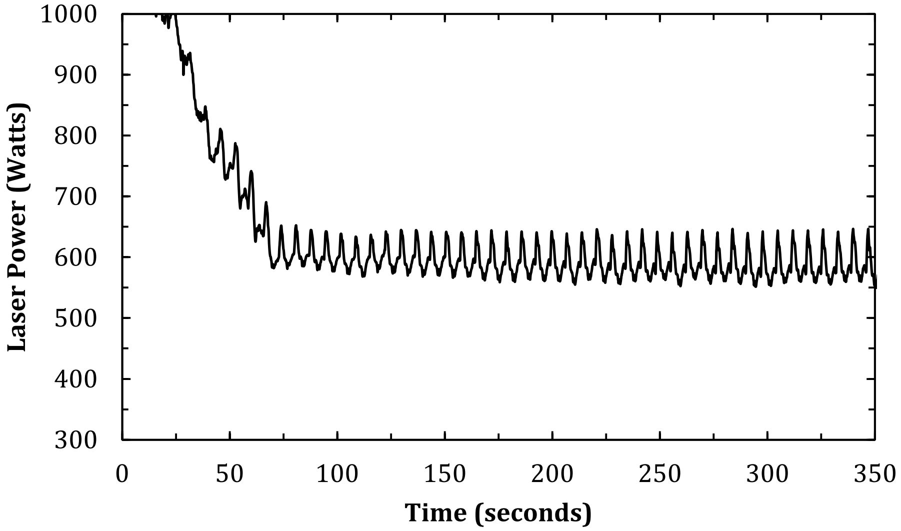

(b)

Figure 3.10. Plots of Laser Power vs. Time for 430 SS Deposits (Figure (a-d) represent 430 SS samples # 1-5 respectively) Note: Sample #3 is not included due to deposition failure

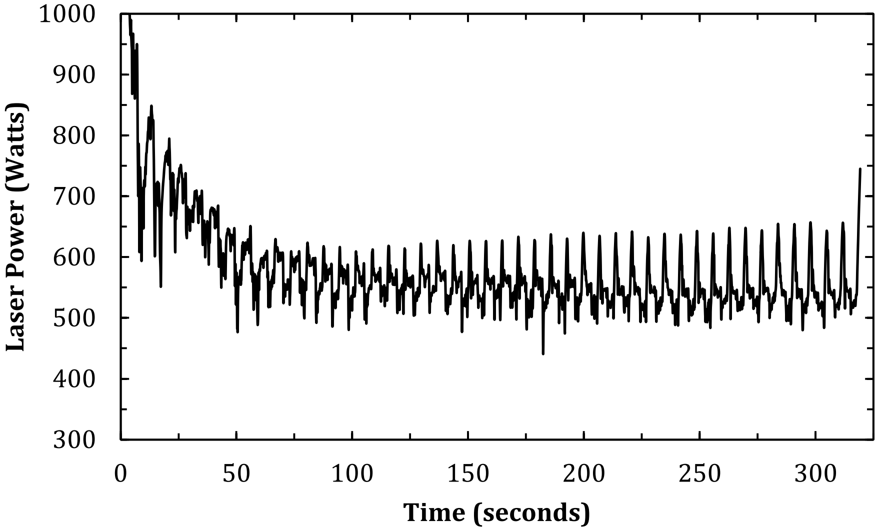

(c)

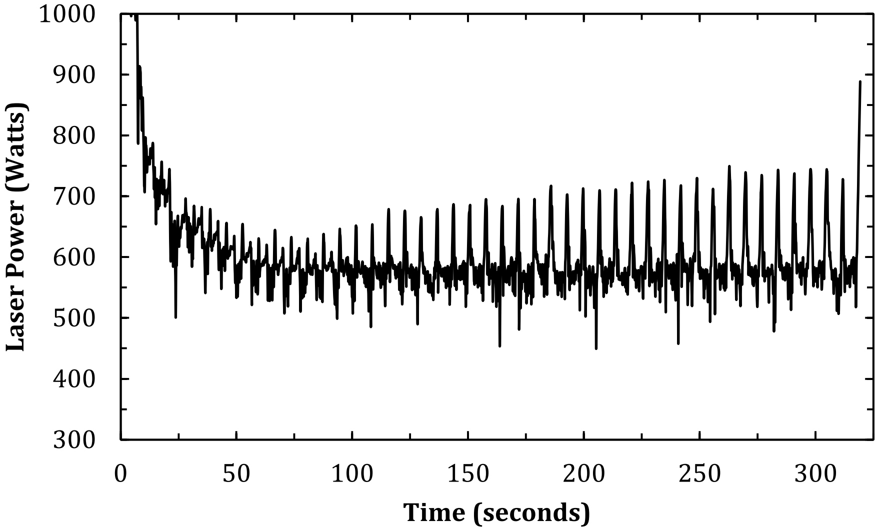

(d)

Figure 3.10. Plots of Laser Power vs. Time for 430 SS Deposits (Figure (a-d) represent 430 SS samples # 1-5 respectively) Note: Sample #3 is not included due to deposition failure (cont.)

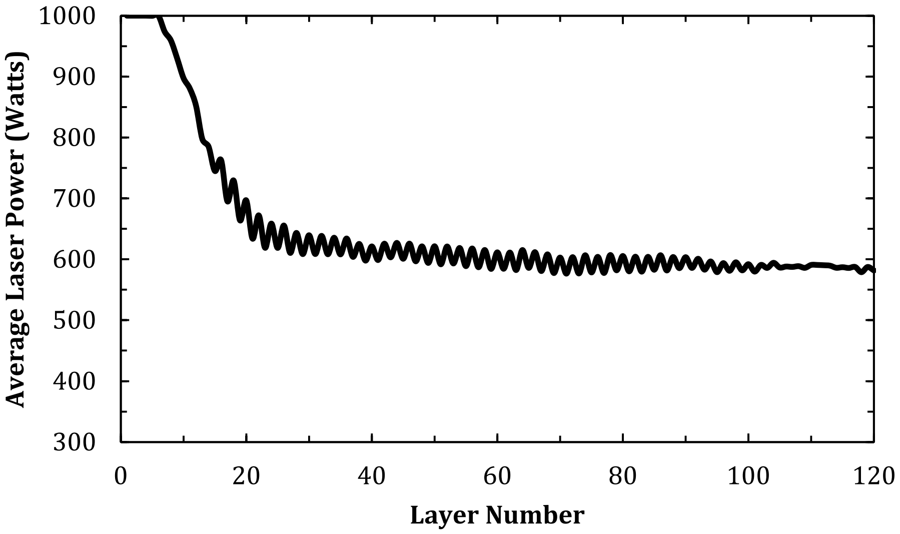

(a)

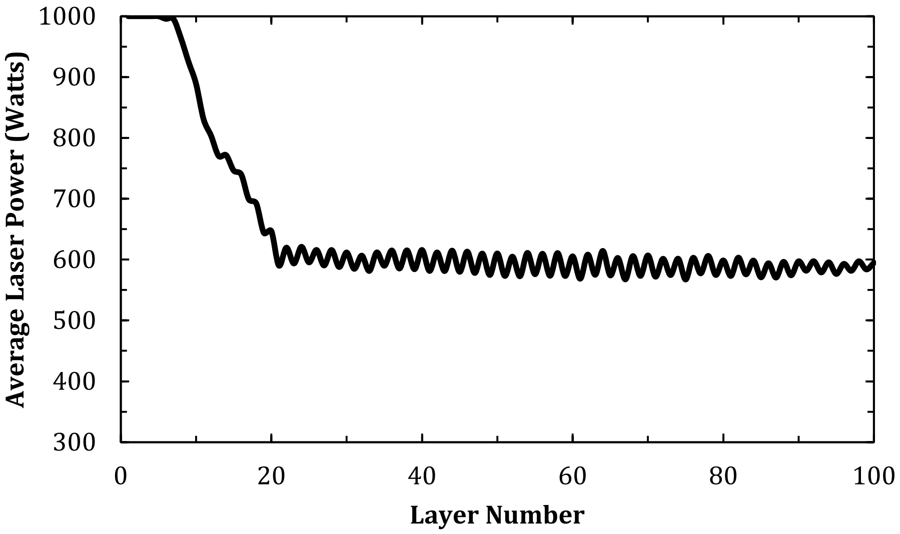

(b)

Figure 3.11. Plots of Average Laser Power per Layer vs. Layer Number for 430 SS deposits (Figure (a-d) represents 430 SS samples # 1-5 respectively) Note: Sample #3 is not included due to deposition failure

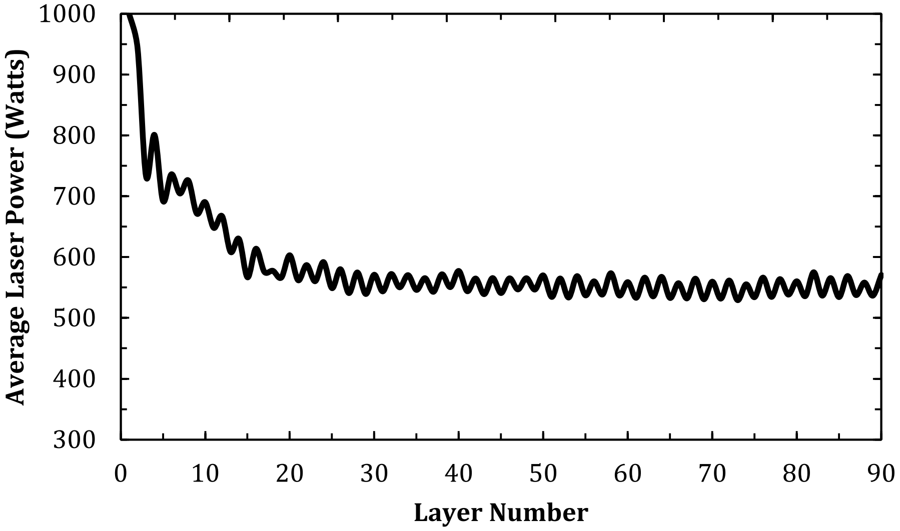

(c)

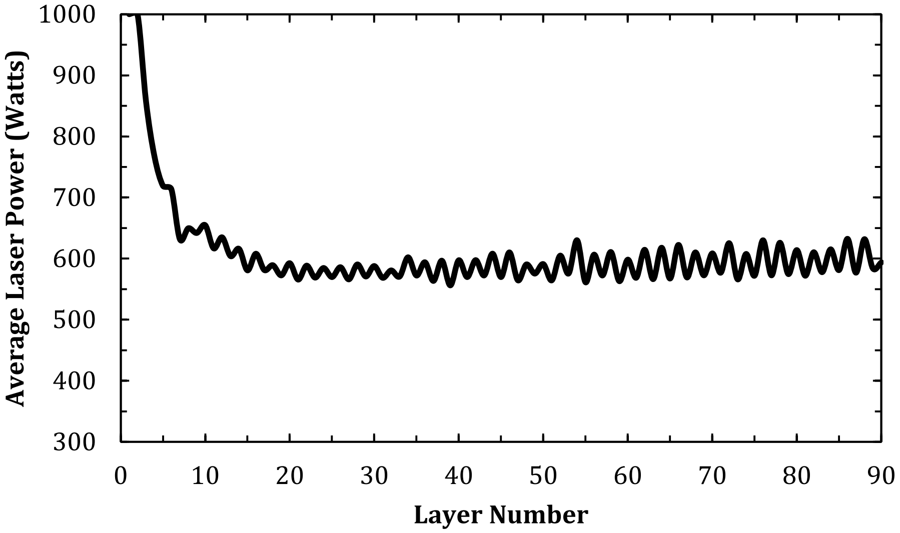

(d)

Figure 3.11. Plots of Average Laser Power per Layer vs. Layer Number for 430 SS deposits (Figure (a-d) represents 430 SS samples # 1-5 respectively) Note: Sample #3 is not included due to deposition failure (cont.)

Figure 3.12. Comparison of Pre-Alloyed (Sample #2) and Mixed Elemental Powder (Sample #4) 430 SS Deposits

3.2.1. EDS Analysis. To confirm that deposits using elemental powder mixes resulted in a homogeneous mixture, EDS line scans were used to examine composition. Figures 3.13 – 3.15 show the EDS line scan results for pre-alloyed and mixed elemental powder deposits from various locations in those deposits. As with 316 SS deposits, results indicate that there was no lack of mixing in mixed elemental powder deposits. The consistent number of counts for 430 SS deposits that were produced with mixed elemental powders leads to a conclusion that a homogeneous deposit was made. Due to the unsuccessful deposition of the parameters used for Sample #3, it was hard to say if a lack of mixing occurred. However, this result at least indicates that deposition quality would become an issue before a lack of mixing is observed. There is more scatter in the counts for Sample #4 than when compared to Sample #1 or Sample #5. Even though there is some fluctuation in Sample #4, most scatter occurs at individual scan points, which could be attributed to the EDS system as much as it could to sample quality. Overall, the results of EDS analysis indicates that homogeneous deposits using 430 SS elemental powder mixes were produced.

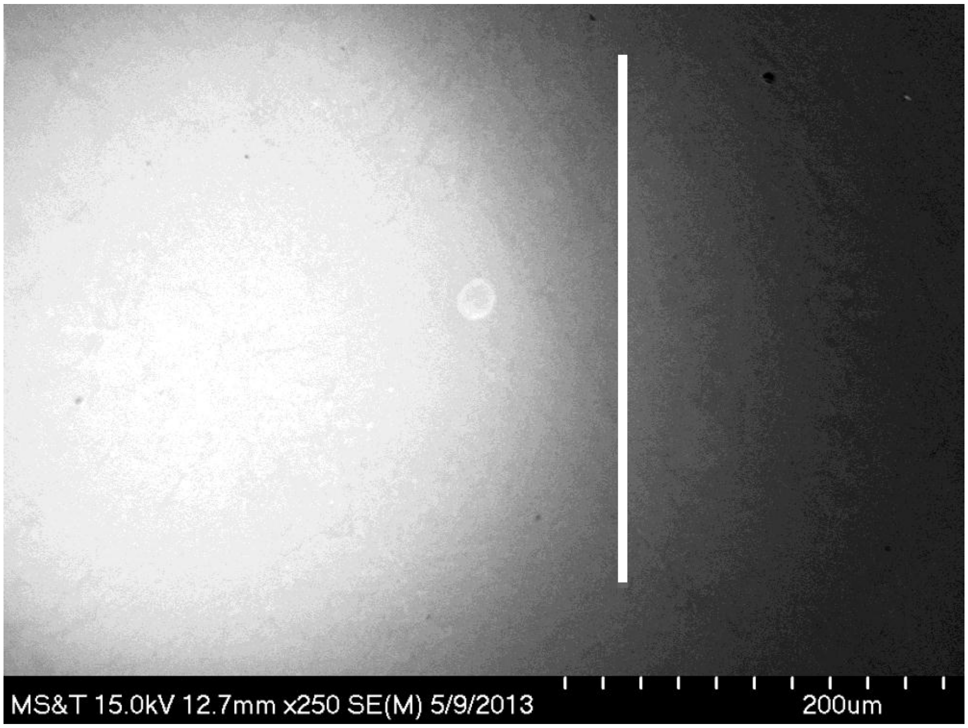

(a)

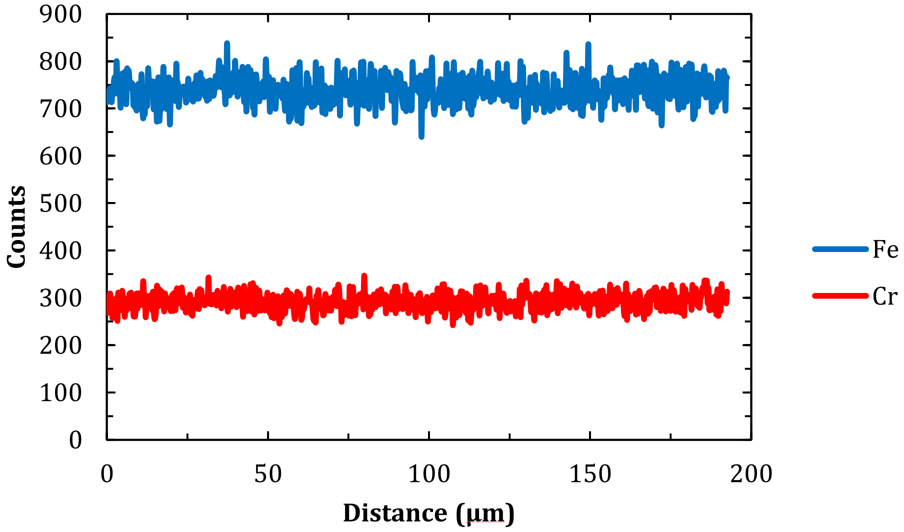

(b)

Figure 3.13. (a) EDS Line Scan Area and (b) Line Scan Results from 430 SS Sample #1

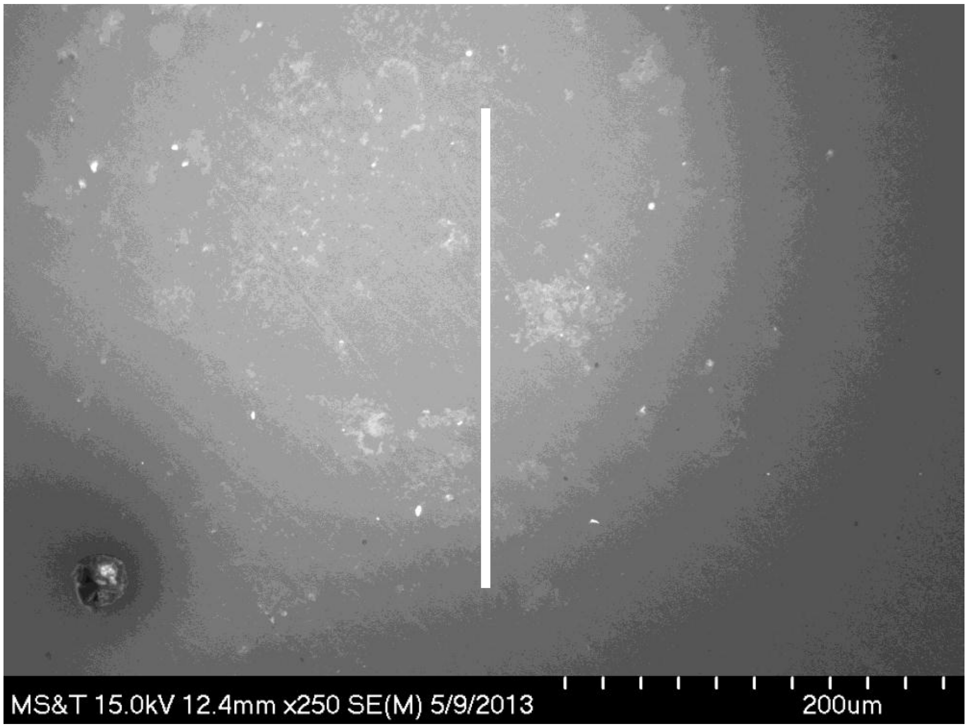

(a)

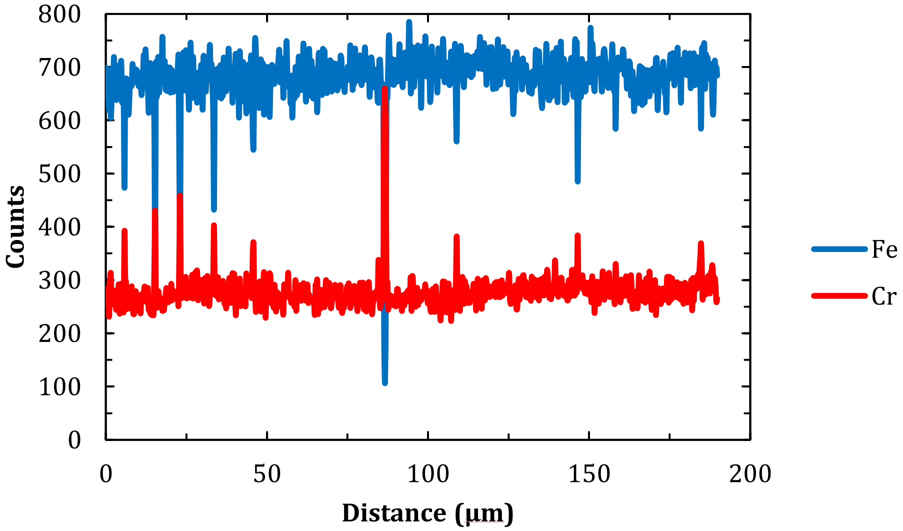

(b)

Figure 3.14. (a) EDS Line Scan Area and (b) Line Scan Results from 430 SS Sample #4

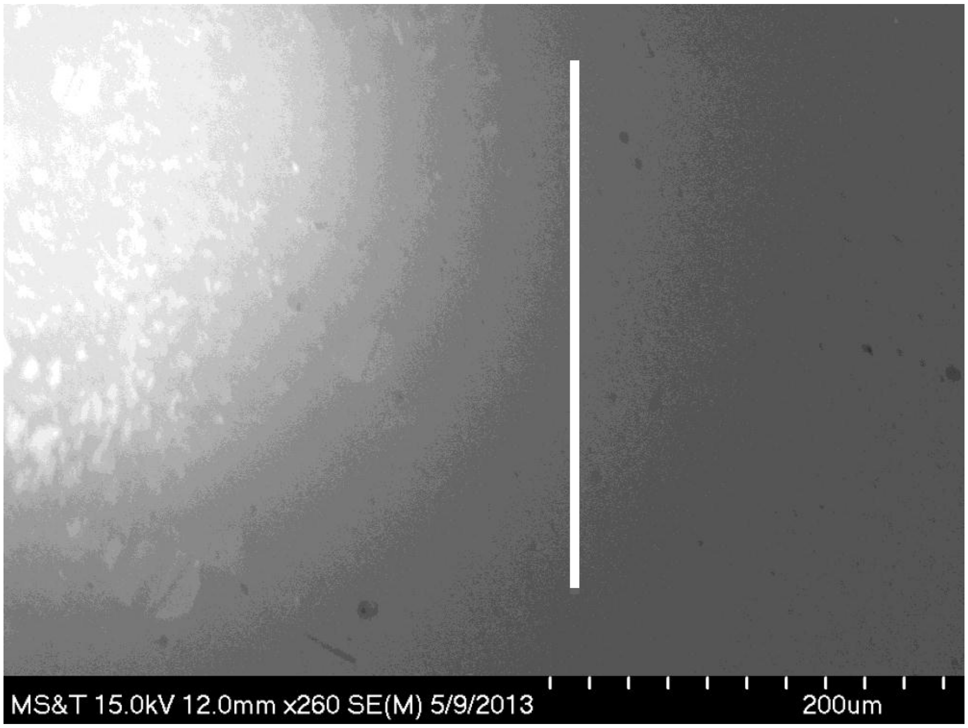

(a)

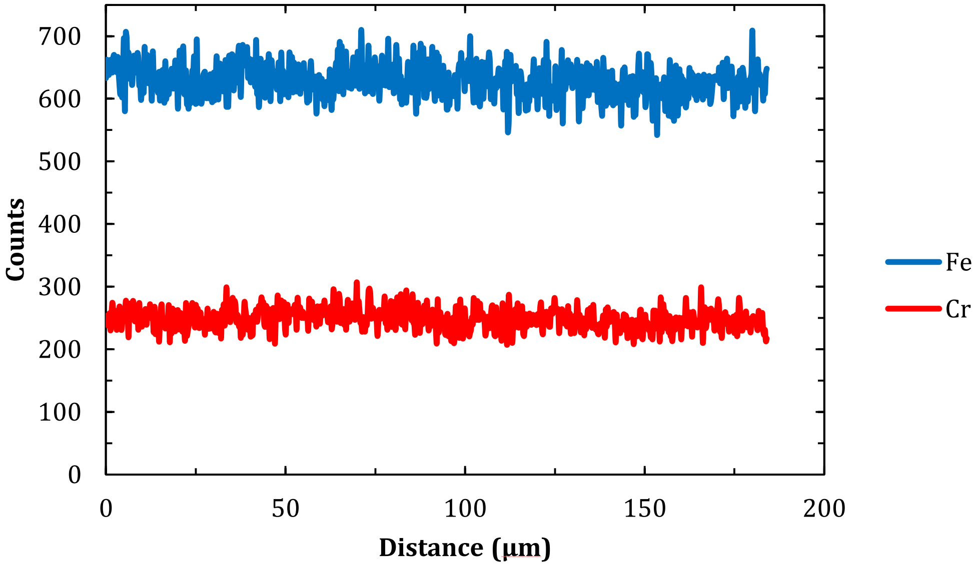

(b)

Figure 3.15. (a) EDS Line Scan Area and (b) Line Scan Results from 430 SS Sample #5

3.2.2. Microstructure Analysis. Deposits made using pre-alloyed and mixed elemental 430 SS powder were polished, etched, and prepared for microstructural analysis using an optical microscope. Figure 3.16 shows optical micrographs of (a-b) pre-alloyed 430 SS deposits and (c-d) mixed elemental powder deposits. Unlike the microstructures in 316 SS deposits, there is very clearly a difference in the structure between the two types of deposits. The pre-alloyed deposit microstructure mostly contains a primary ferrite matrix with some regions of martensite. However, some regions do contain almost entirely ferrite. It would also appear that the grain growth direction follows the build direction (bottom to top). Typically, a fully ferritic microstructure would be observed in 430 SS given the high concentration of chromium, which is a ferrite stabilizer. However, when fast cooling occurs, martensite can form [14]. The regions containing mostly of ferrite are expected in a 430 SS microstructure but the regions of high martensite concentration are less typical. Regardless of the structure present in the pre-alloyed deposits, this structure will serve as the comparison for the mixed elemental 430 SS deposits. Ideally, a similar microstructure would be seen to prove the concept of using mixed elemental powders in laser-based additive manufacturing.

The mixed elemental powder deposit microstructure consists of a fully ferritic microstructure where ferrite grain boundaries etch darkly [12]. This structure will form when no ferrite is transformed during cooling. At the base of the deposit the ferrite cells are smaller and more clustered. As deposit height is increased, the ferrite cells become thinner and have a more columnar shape. Throughout the deposit the ferrite grains grow from the bottom of the sample to the top of the sample (in the build direction). This effect is more prevalent at the top of the build. The ferrite grains in Figure 3.16 (c-d) do vary in color from grain to grain. This is typically an indication of composition variations in the deposit. However, the EDS line scan results indicated a homogeneous composition throughout the deposit. The variation in color is more likely a result of only minimal variations in composition from grain to grain resulting in different etching rates.

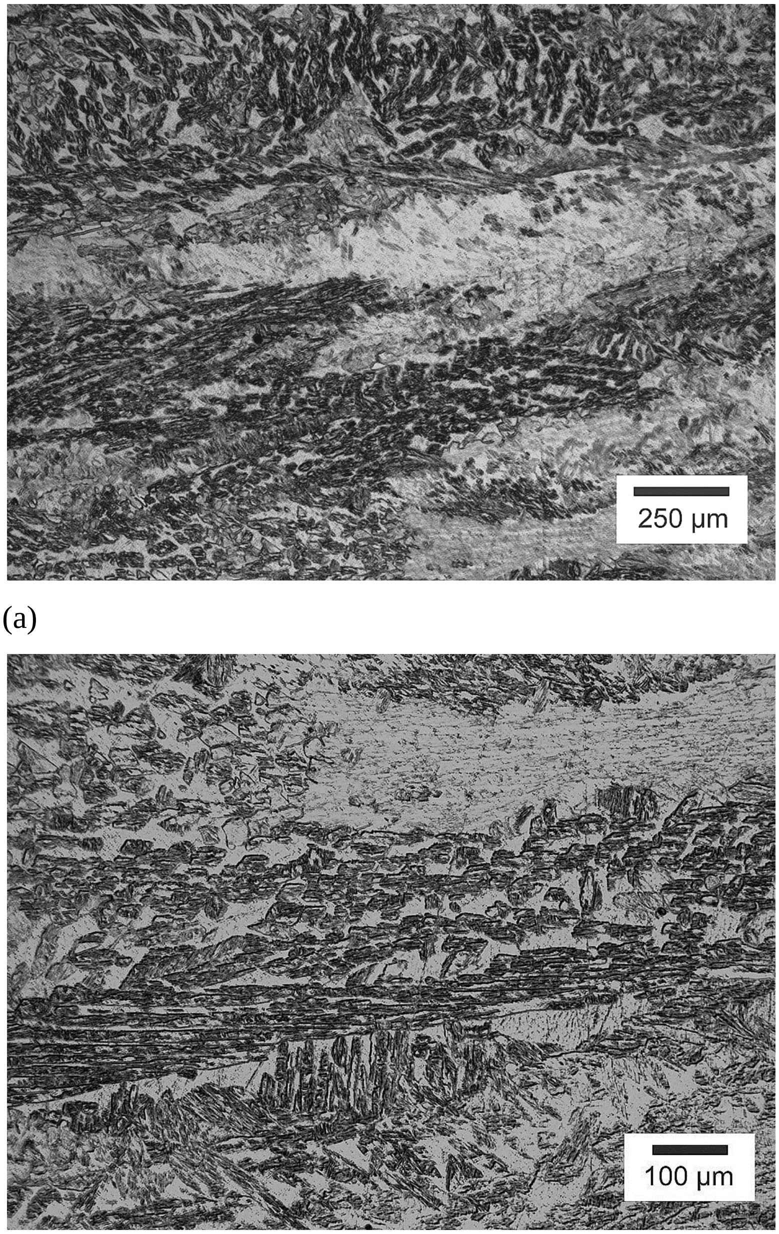

(a)

(b)

Figure 3.16. (a and b) Optical Micrograph of 430 SS Pre-Alloyed Powder Deposit and (c and d) Mixed Elemental Powder Deposit Microstructure

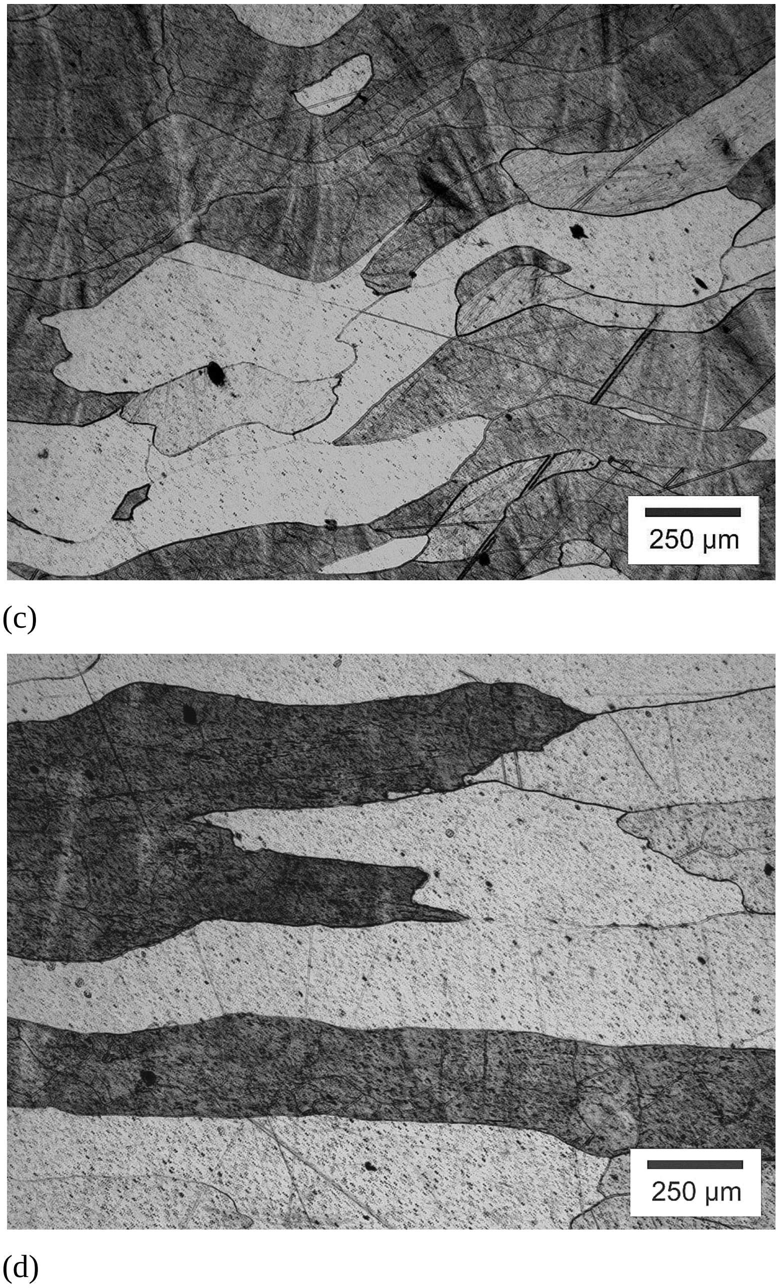

(c)

(d)

Figure 3.16. (a and b) Optical Micrograph of 430 SS Pre-Alloyed Powder Deposit and (c and d) Mixed Elemental Powder Deposit Microstructure (cont.)

To prove the concept of using mixed elemental powders in laser-based additive manufacturing, ideally similar microstructures would be observed in both pre-alloyed and mixed elemental powder deposits. In the case of 430 SS, deposits with the two types of powder exhibited differing microstructures. A further discussion on these differences can be found in Section 3.2.4.

3.2.3. Mechanical Properties. To examine mechanical properties of pre-alloyed and mixed elemental 430 SS deposits Vickers hardness measurements were performed. Figure 3.17 shows Vickers hardness measurements for both pre-alloyed and mixed elemental 430 SS deposits measured with (a) 500 g load and (b) 50 g load, both with a 5 second dwell time. Pre-alloyed deposits had a hardness of 356±46 VHN while mixed elemental powder deposits had a hardness of 150±4 VHN when measured with a 500 g load. When measured with a 50 g load, the matrix of pre-alloyed deposits exhibited a hardness of 275±122 VHN and the martensitic structure exhibited a hardness of 487±66 VHN. The lighter colored grains of the mixed elemental 430 SS deposits had a hardness of 162±9 VHN while the darker colored grains had a hardness of 168±8 VHN. The hardness values for mixed elemental powder deposits are consistent with results from literature; however, the pre-alloyed deposits exhibit a hardness that is much higher than expected [15].

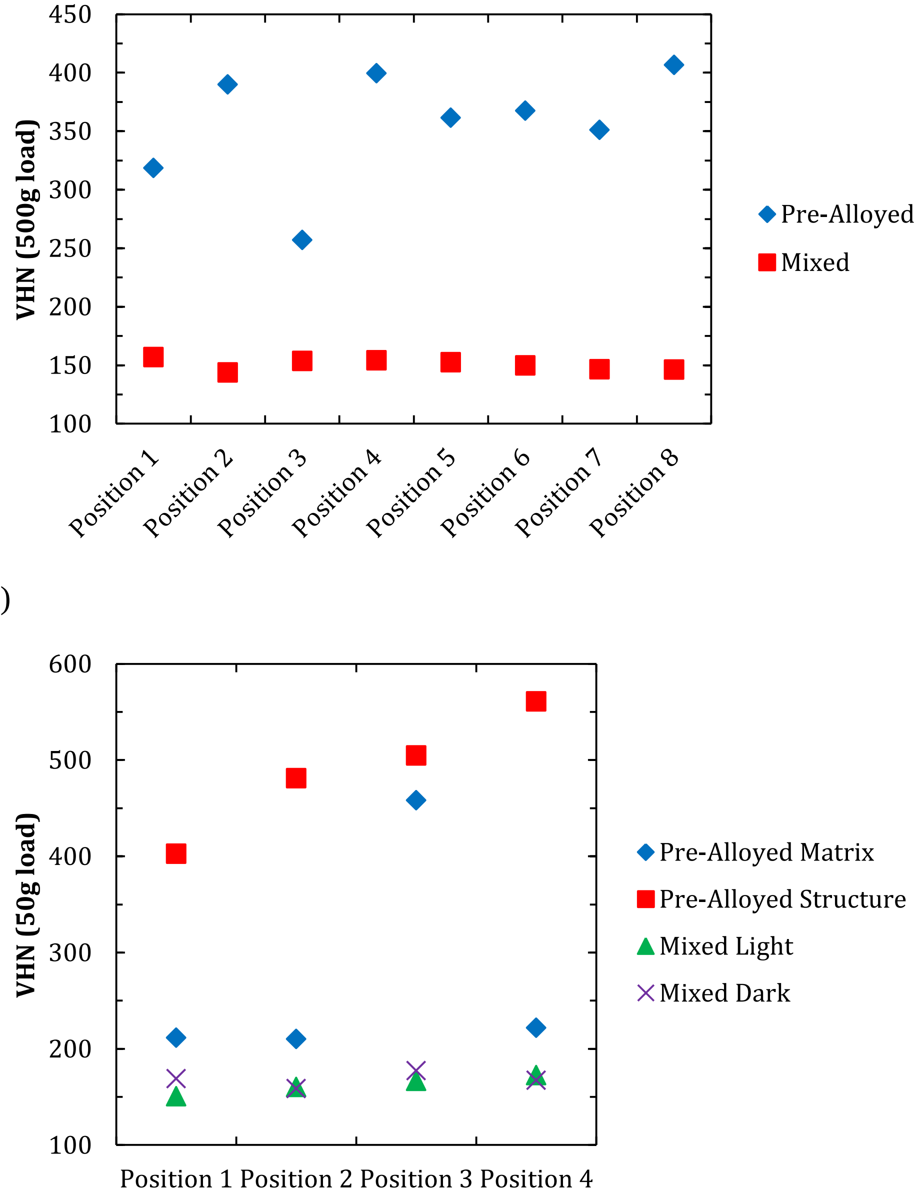

(a)

(b)

Figure 3.17. (a) Plot of Vickers Hardness vs. Position for Pre-Alloyed and Mixed Elemental Powder 430 SS Deposits Measured with a 500 g Load and (b) 50 g Load

Although the mixed elemental deposits showed consistent hardness values throughout the deposits, the values were significantly less than what was observed in the pre-alloyed deposits. To confirm if differences in temperature and cooling rates were leading to the observed differences in hardness measurements, both types of samples were subjected to a post-processing annealing treatment. According to ASTM standards, the samples were annealed at 770 °C for 1 hour and then allowed to air cool. Figure 3.18 shows hardness values in both types of deposits following the annealing treatment. Pre-alloyed deposits had a measured Vickers hardness (500 g load) of 210±6 VHN and mixed elemental powder deposits had a measured Vickers hardness of 130±2 VHN in the annealed state. As is expected, both types of deposits exhibited lower and more uniform hardness values throughout the deposits after being annealed. However, the pre-alloyed 430 SS deposits were still significantly harder than the mixed elemental powder deposits. These differences should not be present following an annealing treatment, assuming the materials had similar compositions. A further discussion on these differences can be found in Section 3.2.4.

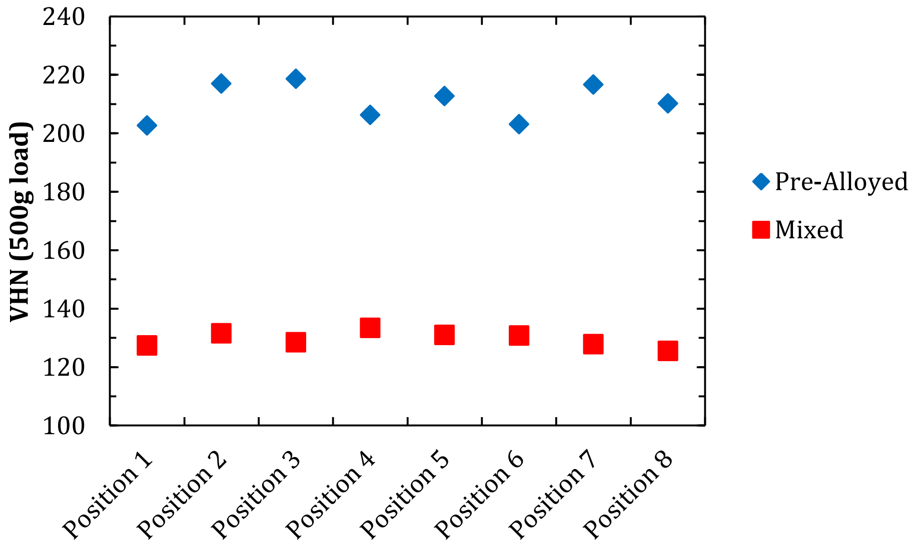

Figure 3.18. Plot of Vickers Hardness vs. Position for Pre-Alloyed and Mixed Elemental Powder 430 SS Deposits Following an Annealing Treatment of 770 °C for 1 Hour and an Air Cool

3.2.4. Additional Discussion. The differences in microstructure and mechanical properties of 430 SS pre-alloyed and mixed elemental powder deposits warrant further investigation. Without accurate temperature profiles for the deposits, it was presumed that the microstructure differences could be attributed to different cooling rates. The different cooling rates would also lead to differing hardness values in the as-deposited state. However, even after post-processing heat treatments the two samples exhibited different hardness values. A heat treatment would eliminate any changes in mechanical properties that were a result of cooling rate differences. Since this post processing still showed differences in the two types of samples, the composition of the two samples was examined. Although EDS Analysis was performed on both types of samples this was meant to be a qualitative and not quantitative analysis. Variations in composition would lead to differing microstructures as well as mechanical properties.

A sample each of a pre-alloyed deposit and a mixed elemental deposit were sent to a third-party testing agency for chemical analysis. Testing was performed by St. Louis Testing Laboratories using Optical Emission Spectroscopy (OES) following ASTM E1086-08. The results of the analysis can be seen in Table 3.3. The OES results show that overall, the two samples have similar compositions and both conform to AISI 430 chemical composition standards. The only major differences in composition are in the amounts of carbon, chromium, manganese, and nickel. The mixed elemental powder deposit (Sample #4) contains approximately 1.0 wt% more chromium than the pre-alloyed deposit (Sample #1). This 1.0 wt% is made up by approximately 0.5 wt% additions each of manganese and nickel in the pre-alloyed deposit. The pre-alloyed deposits also contain approximately 0.06 wt% carbon more than mixed elemental deposits. Individually, the differences in elements between the two types of deposits are likely not enough to have the observed impact on microstructure and mechanical properties. As a whole, these differences may have a larger impact and lead to slight changes in mechanical properties or microstructure.

Table 3.3. Third-Party Testing Results on 430 SS Deposits

Element	**Sample #1 (Pre-Alloyed) (wt %)**	**Sample #4 (Mixed) (wt %)**
Iron	Bal.	Bal.
Carbon	**0.07**	**<0.01**
Silicon	0.26	0.13
Sulfur	0.015	0.005
Manganese	**0.46**	**0.12**
Phosphorus	0.008	<0.001
Nickel	**0.42**	**0.02**
Chromium	**16.53**	**17.51**
Molybdenum	0.07	<0.01
Copper	0.09	0.04
Tungsten	<0.01	<0.01
Tin	<0.01	<0.01
Titanium	0.01	0.01
Columbium	<0.01	<0.01
Vanadium	<0.01	<0.01
Aluminum	<0.01	<0.01
Cobalt	0.03	0.01

Although, there may be some differences in chemical composition between the two types of samples, the fact remains that both conform to AISI 430 SS composition. Two materials conforming to this specification and processed in the same manner should not have the observed differences in microstructure or mechanical properties. Figure 3.19 shows an Fe-Cr phase diagram. From the Fe-Cr phase diagram, 430 SS (16-18 wt% Cr) would typically have a fully ferritic microstructure [16]. A region of austenite and ferrite is possible, however, this would require the chromium content to fall below 13.0 wt%. The increased carbon content in the pre-alloyed sample, although minimal, may have a large impact. This increased carbon content shifts this austenite + ferrite region to higher chromium content and also would result in the formation of martensite, which was present in the pre-alloyed sample [14]. Martensite is a much harder phase than ferrite and would explain why the "structure" (martensite) was so much harder than the "matrix" (ferrite) in the pre-alloyed sample.

To fully understand the differences between microstructure and mechanical properties in 430 SS pre-alloyed and mixed elemental powder deposits, further experiments may need to be performed. At a minimum, a new batch of mixed elemental 430 SS powder should be mixed and deposited. It's possible that repeating the experiment would lead to the expected results of fully ferritic microstructures and similar mechanical properties. However, if the same results are observed, further investigation into the experimental procedure and alloy compositions would be needed to determine the differences between the two types of samples.

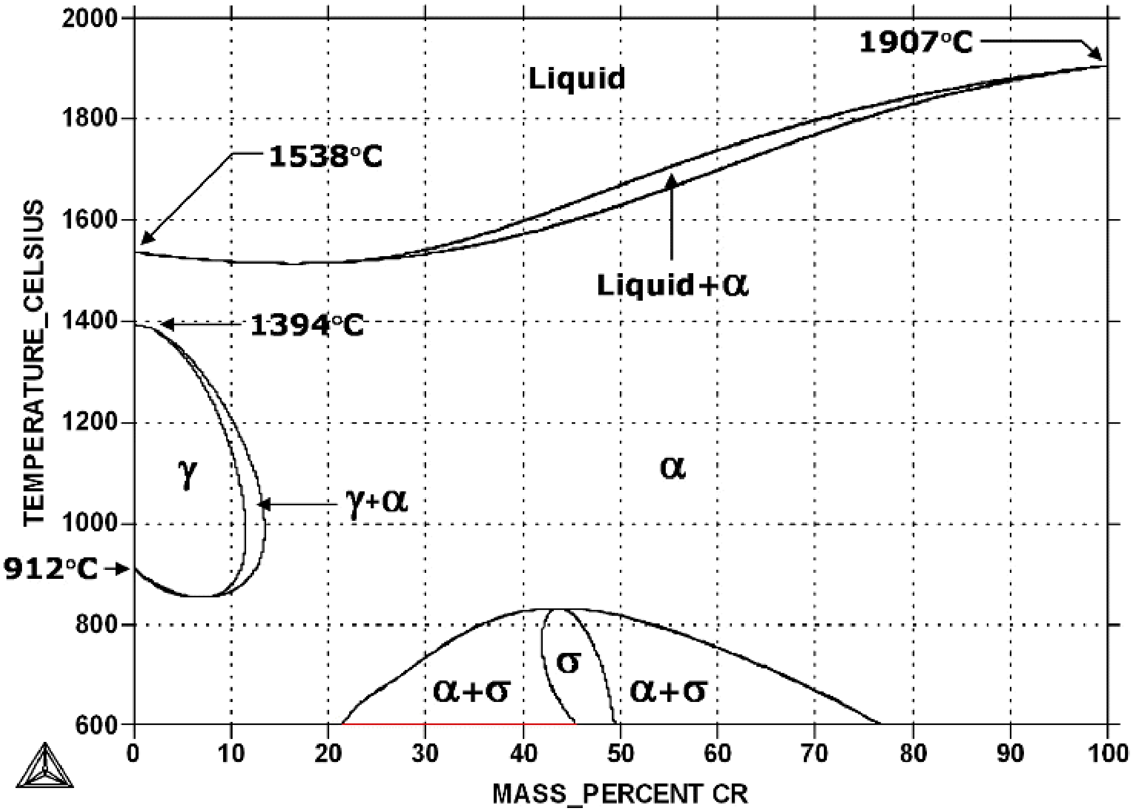

Figure 3.19. Fe-Cr Phase Diagram

3.3 TI-6AL-4V

Table 3.4 shows the process parameters used during the deposition of Ti-6Al-4V samples using both pre-alloyed powder and mixed elemental powder, along with the resulting dimensions of those deposits. Plots of laser power vs. time and average laser power per layer vs. layer can be seen in Figure 3.20 and 3.21 respectively. It should be noted that Samples #3-8 are missing from Table 3.4. The first deposits produced with mixed elemental powder contained significant levels of porosity. Adjustments were made to deposition parameters until the porosity present in the samples was minimized. After experimentation with Samples #3-8, it was found that layer thickness had the largest impact on the amount of porosity. Therefore, a layer thickness of 0.07 mm, instead of the 0.25 mm used in pre-alloyed deposits, was used for mixed elemental powder deposits. A longer discussion on the presence of porosity in these samples can be found in Section 3.3.2.

As with previous materials used in this study, the set-point used during deposition was adjusted in an effort to match the steady state laser power of pre-alloyed and mixed elemental powder deposits. From Figure 3.20 (a and e) and 3.21 (a and e), Sample #11 has the closest match to the pre-alloyed powder deposit. The physical dimensions of Sample #11 also closely resemble that of the pre-alloyed powder deposits. As mentioned previously, the layer thickness had to be adjusted for mixed elemental powder deposits to accommodate porosity issues. However, with a slight adjustment to the set-point, a deposit using mixed elemental powders can be produced with similar physical quality as a deposit produced using pre-alloyed powders.

Table 3.4. Process Parameters and Deposit Dimensions for Ti-6Al-4V

	Sample #1	**Sample #2**	**Sample #9**	**Sample #10**	**Sample #11**
Powder Type:	Pre-Alloyed	Pre-Alloyed	Mixed	Mixed	Mixed
Set-Point:	150	175	150	125	250
# of Layers:	70	70	200	200	200
Layer Thickness: (mm)	0.25	0.25	0.07	0.07	0.07
Travel Speed: (mm/s)	10	10	10	10	10
Powder Feed Rate: (RPM)	1.5	1.5	1.5	1.5	1.5
Height: (mm)	19.3	19	18.09	17.49	19.03
Width: (mm)	25.99	26.07	25.23	25.12	25.42
Thickness: (mm)	2.65	2.7	2.82	2.16	3.14

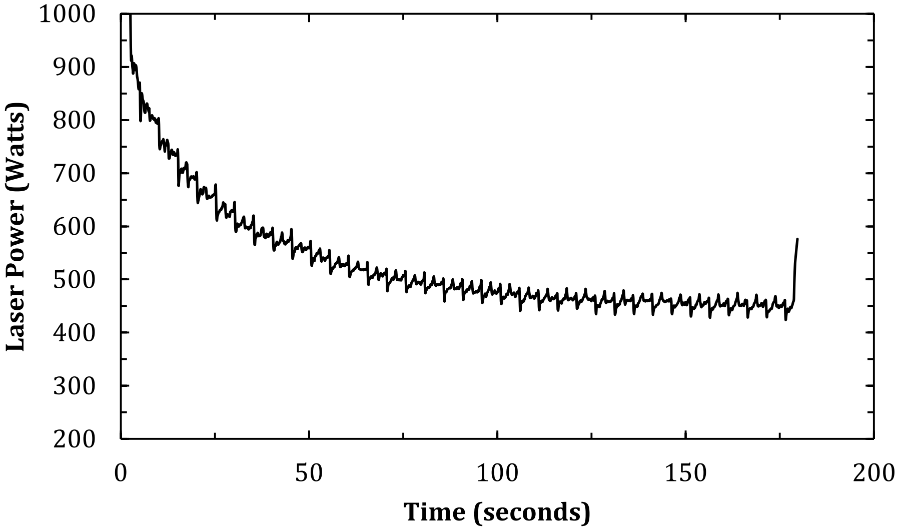

(a)

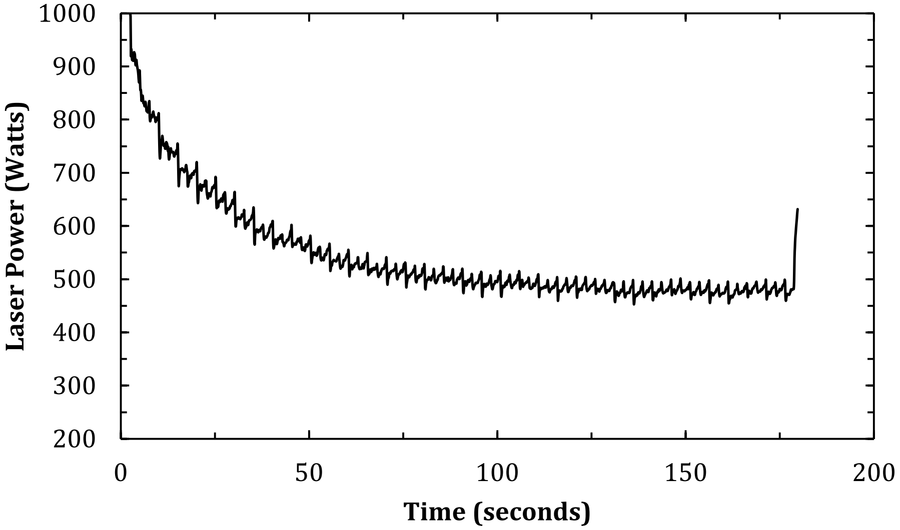

(b)

Figure 3.20. Plots of Laser Power vs. Time for Ti-6Al-4V Deposits (Figures (a-e) represents Ti-6Al-4V samples #1 & 2 and 9-11 respectively)

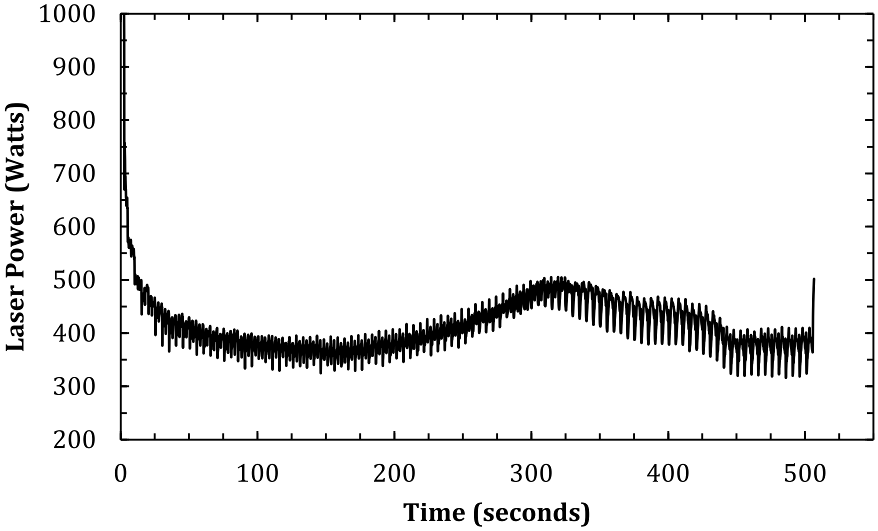

(c)

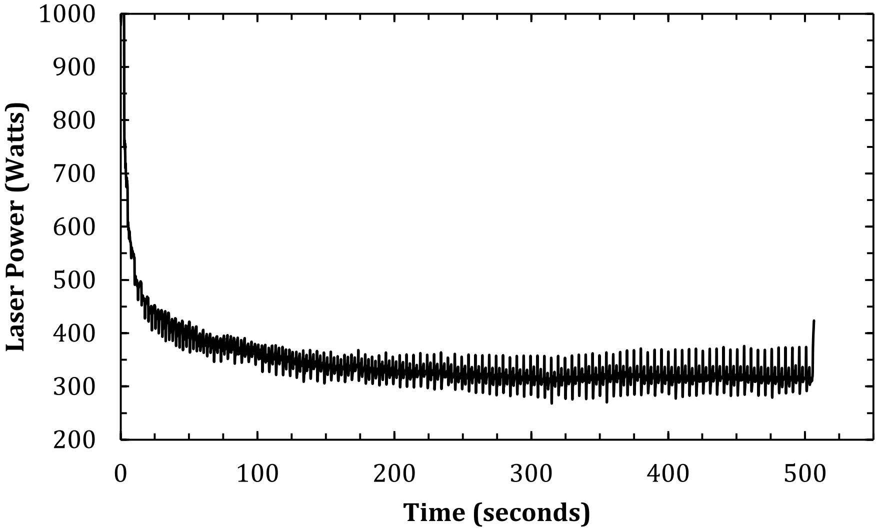

(d)

Figure 3.20. Plots of Laser Power vs. Time for Ti-6Al-4V Deposits (Figures (a-e) represents Ti-6Al-4V samples #1 & 2 and 9-11 respectively) (cont.)

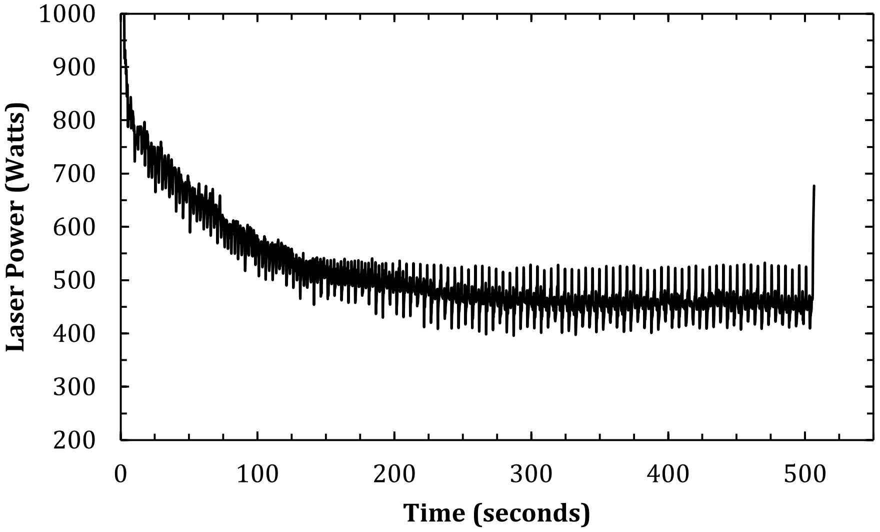

(e)

Figure 3.20. Plots of Laser Power vs. Time for Ti-6Al-4V Deposits (Figures (a-e) represents Ti-6Al-4V samples #1 & 2 and 9-11 respectively) (cont.)

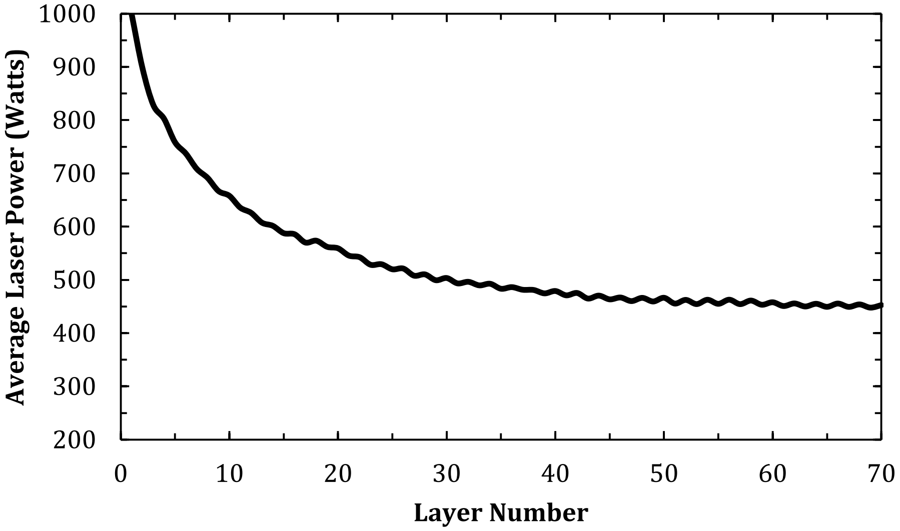

(a)

Figure 3.21. Plots of Average Laser Power per Layer vs. Layer for Ti-6Al-4V Deposits (Figure (a-e) represents Ti-6Al-4V samples #1 & 2 and 9-11 respectively)

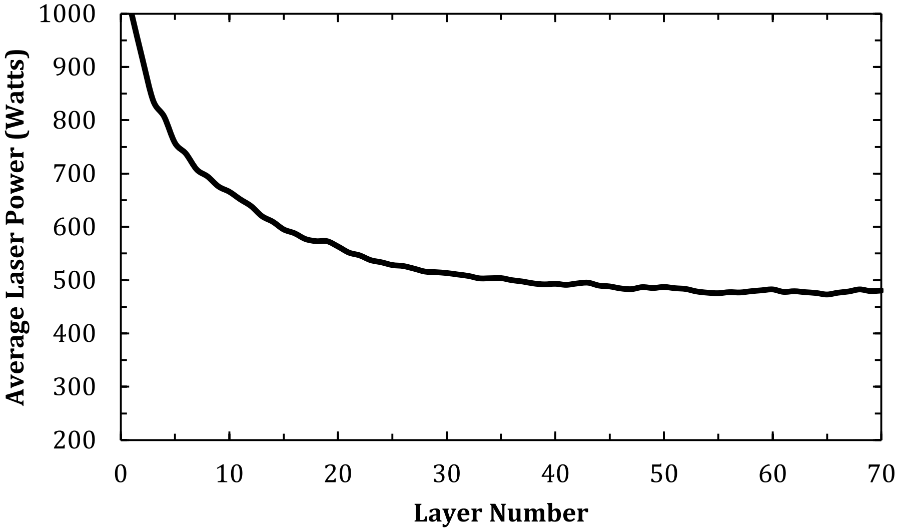

(b)

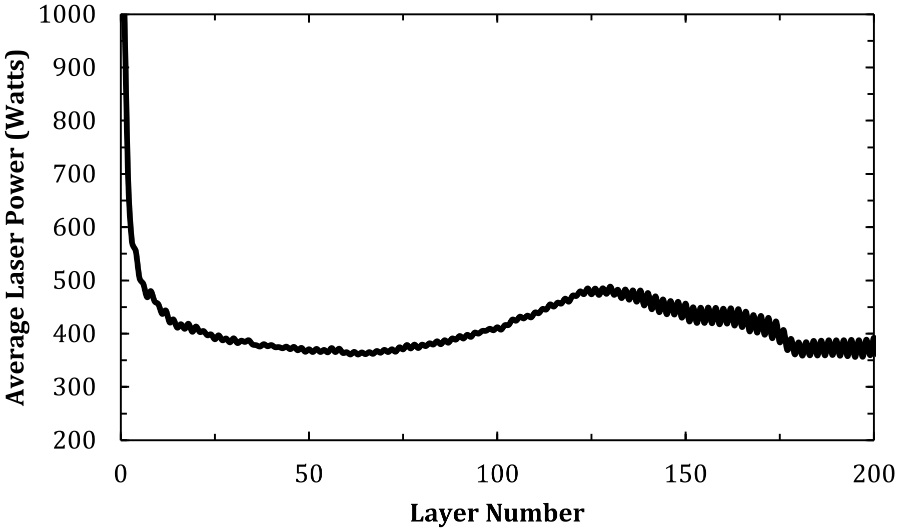

(c)

Figure 3.21. Plots of Average Laser Power per Layer vs. Layer for Ti-6Al-4V Deposits (Figure (a-e) represents Ti-6Al-4V samples #1 & 2 and 9-11 respectively) (cont.)

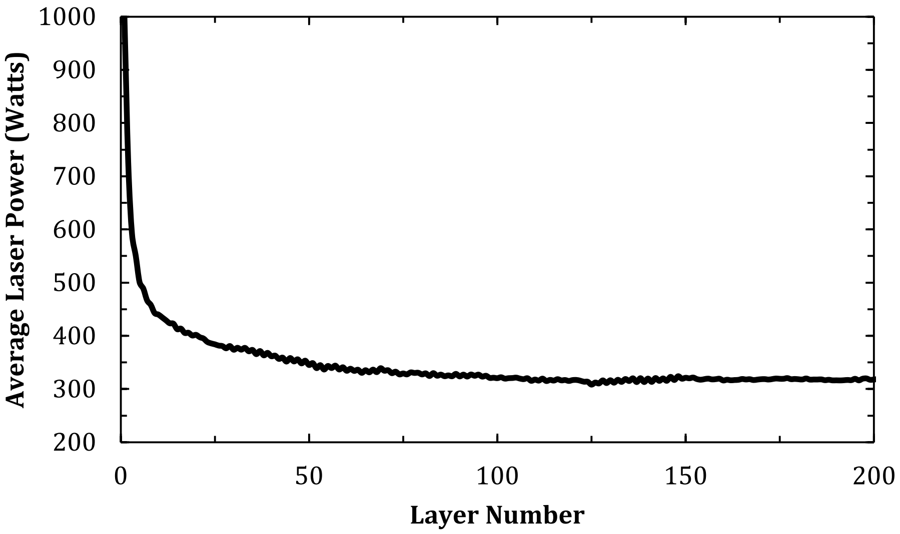

(d)

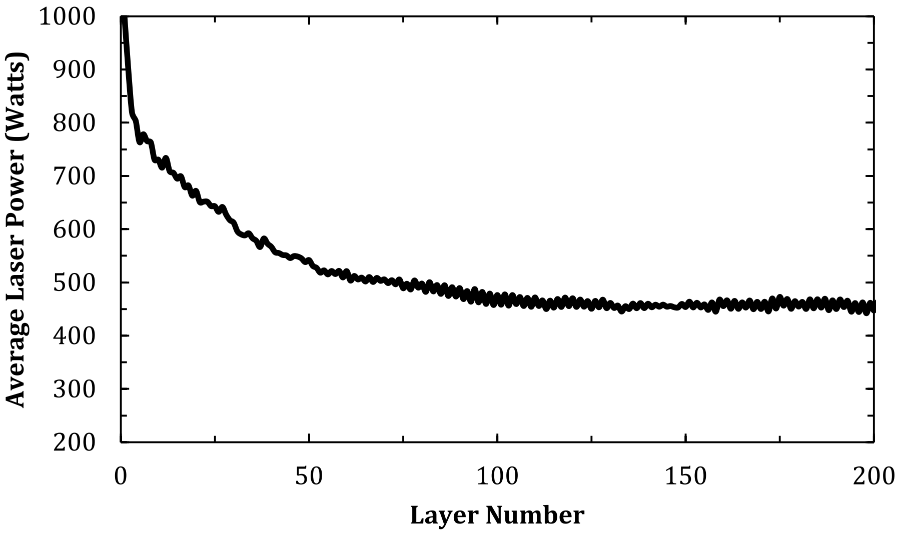

(e)

Figure 3.21. Plots of Average Laser Power per Layer vs. Layer for Ti-6Al-4V Deposits (Figure (a-e) represents Ti-6Al-4V samples #1 & 2 and 9-11 respectively) (cont.)

3.3.1. EDS Analysis. The initial step in determining the quality of deposits was to confirm that a homogeneous composition was present in both types of samples. Figures 3.22 and 3.23 shows the results of EDS line scans, which indicate consistent counts of all elements confirming a homogeneous composition. With the presence of porosity in mixed elemental deposits, there was concern that the pores could lead to an inconsistent composition. However, the EDS results show that this is not the case. Overall, the line scans have consistent counts throughout the duration of the scan. The results for Ti-6Al-4V deposits are perhaps even more consistent than the results observed in stainless steel deposits.

It appears from Figure 3.23 that the deposit produced using mixed elemental powders has a higher relative number of counts of vanadium than aluminum, unlike the pre-alloyed powder deposit (Figure 3.22). Although the line scans are used to confirm a homogeneous chemistry throughout the deposit, the number of counts is not necessarily an exact measurement of chemistry. This procedure was meant to be a qualitative analysis and not a quantitative analysis. To get an exact chemistry of the deposit, EDS with a standard or some other analysis technique should be performed. Given that careful measurements were used when weighing out powders, it is believed that the deposit should be the expected 90 wt% Ti, 6 wt% Al, and 4 wt%V. However, before being used in a manufacturing environment this should be confirmed.

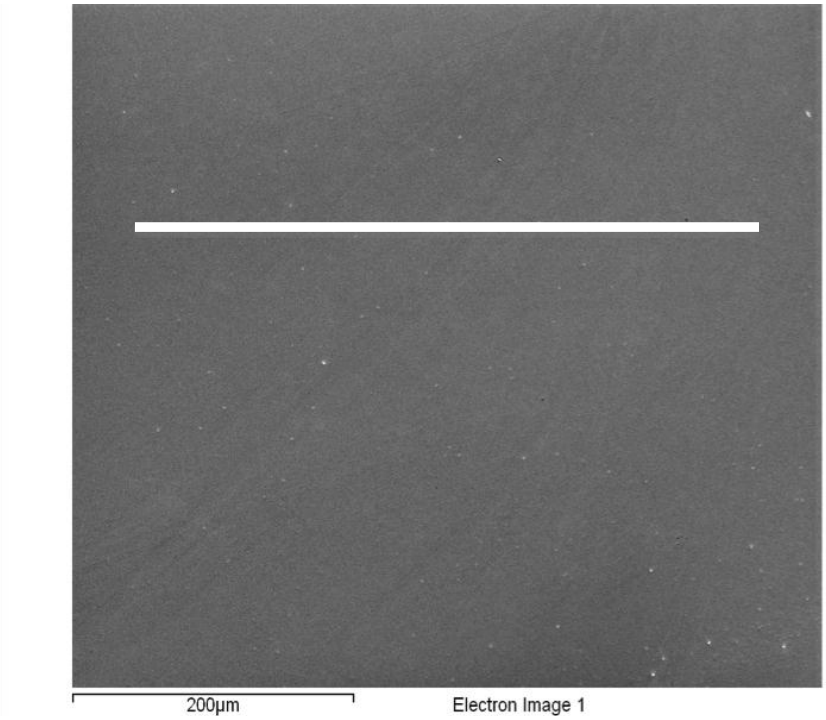

(a)

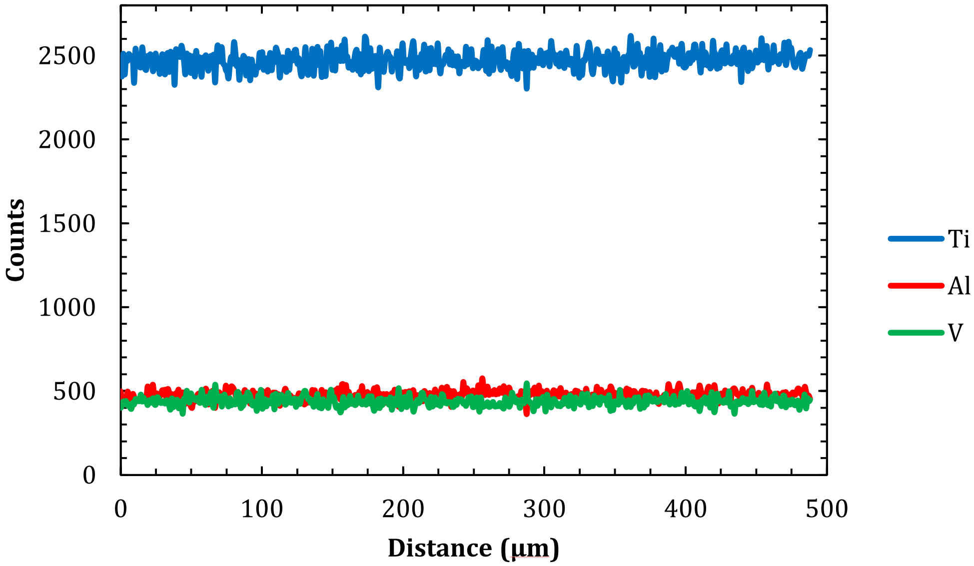

(b)

Figure 3.22. (a) EDS Line Scan Area and (b) Line Scan Results from Ti-6Al-4V Sample #2.

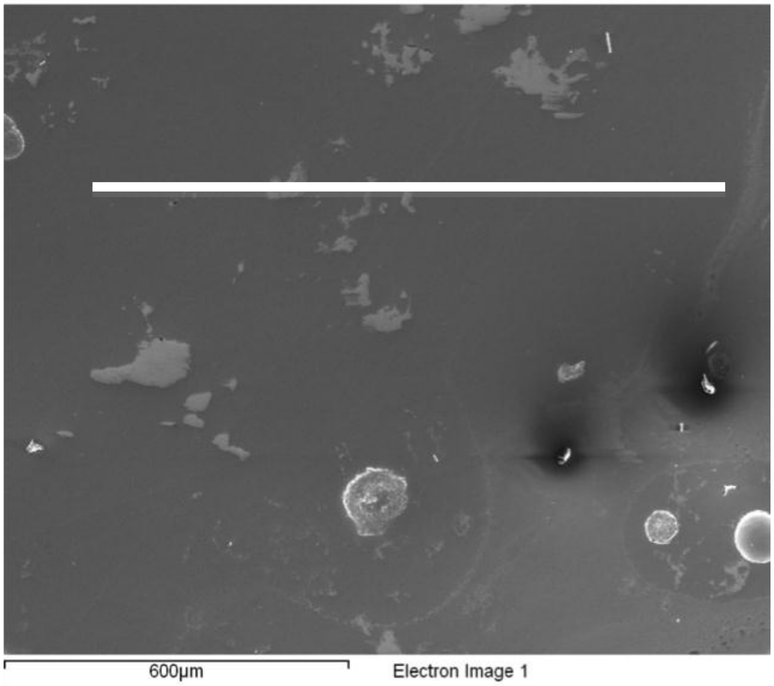

(a)

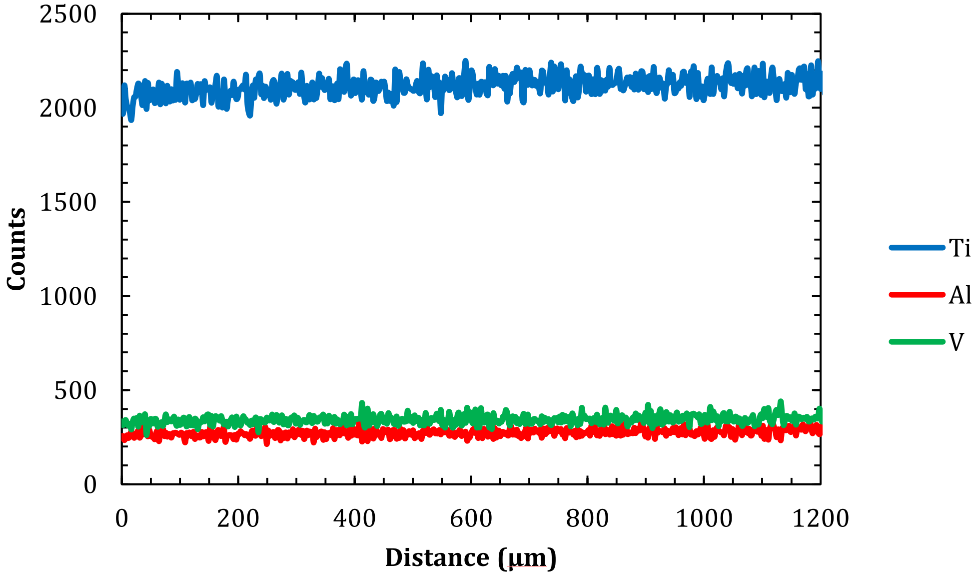

(b)

Figure 3.23. (a) EDS Line Scan Area and (b) Line Scan Results from Ti-6Al-4V Sample #11.

3.3.2. Presence of Porosity. One observation of Ti-6Al-4V deposits produced with mixed elemental powders was the presence of, in some cases, significant porosity. Pre-alloyed deposits of Ti-6Al-4V did not exhibit porosity and laser-based additive manufacturing should produce fully dense parts. To characterize the porosity in these samples, optical micrographs were taken at various positions in the deposit to capture the porosity. Then, using ImageJ analysis software, a particle analysis was done to determine the percentage of porosity as well as the average pore size. Figure 3.24 shows (a) an optical micrograph of the porosity observed in mixed elemental Ti-6Al-4V deposits along with (b) the resulting image for ImageJ particle analysis.

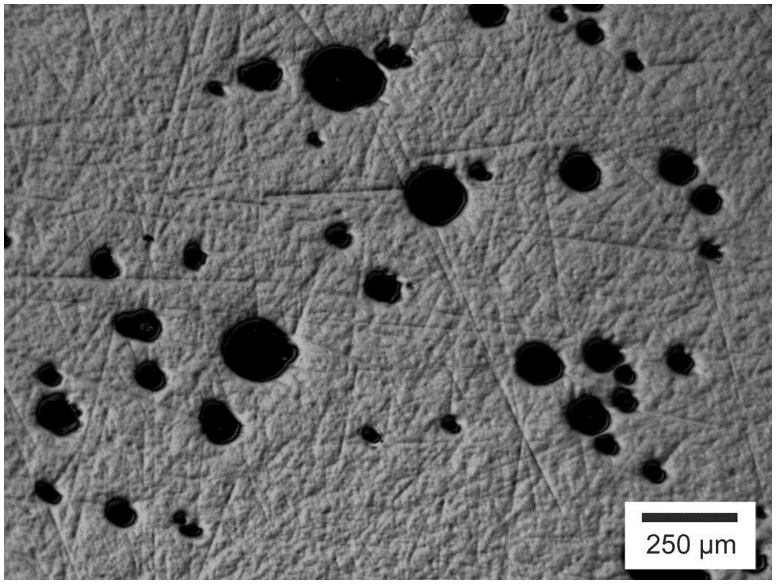

(a)

Figure 3.24. (a) Optical Micrograph of Porosity in Mixed Elemental Ti-6Al-4V Deposit and (b) Optical Micrograph after ImageJ Particle Analysis

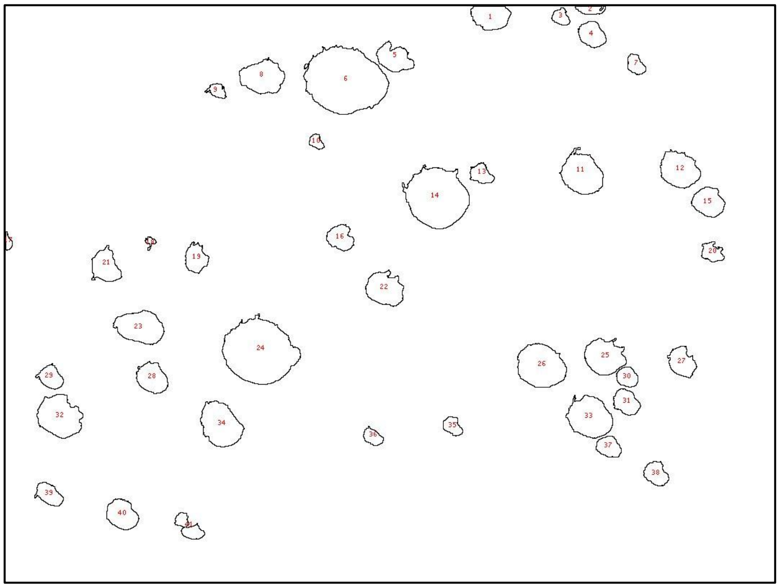

(b)

Figure 3.24. (a) Optical Micrograph of Porosity in Mixed Elemental Ti-6Al-4V Deposit and (b) Optical Micrograph after ImageJ Particle Analysis (cont.)

Figure 3.25 (a and b) shows the percentage of porosity and average pore size for the mixed elemental Ti-6Al-4V deposits determined from the ImageJ particle analysis. General trends indicate that the percentage of porosity in the sample was most severe at the bottom of the sample and decreased at the top of the sample. Ti-6Al-4V Sample #10, which also had the lowest set-point, showed the highest percentage of porosity ranging from 18% at the bottom of the sample to 12% at the top. Conversely, Ti-6Al-4V sample #11, which had the highest set-point, had the lowest percentage of porosity ranging from 8% at the bottom of the sample to 7.5% at the top. As the set-point on the system was increased, the overall percentage of porosity decreased but the average pore size tended to increase. This is likely a result of smaller pores coalescing to form larger pores and leads to the conclusion that a higher set-point resulting in a larger melt pool could reduce the presence of porosity in these samples.

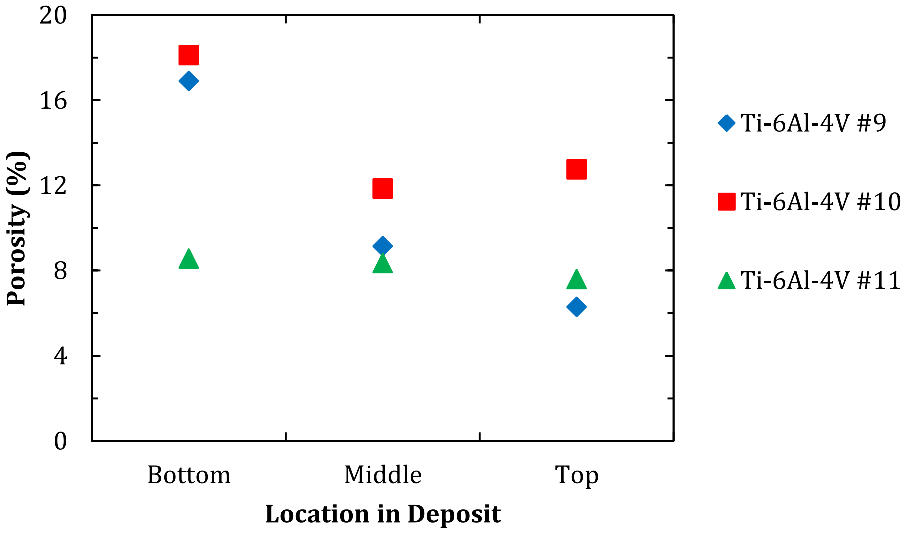

(a)

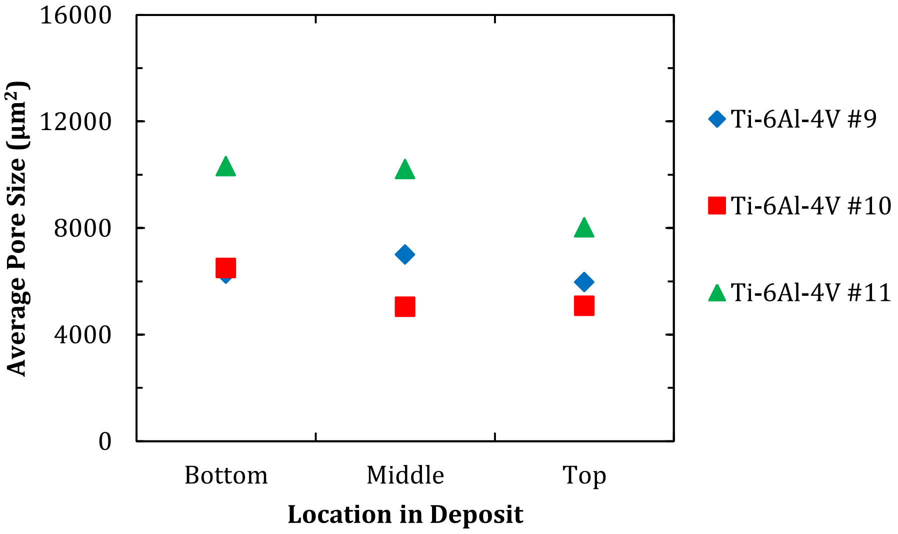

(b)

Figure 3.25. Plots of (a) Percentage Porosity and (b) Average Pore Size with Respect to Location in Deposit for Mixed Elemental Powder Ti-6Al-4V Deposits

Although Ti-6Al-4V deposits produced with elemental powder mixes had significant levels of porosity, a small region with minimal to no porosity was observed in these samples. Figure 3.26 shows a diagram of the laser deposition process and the location of this porosity free region. As the thin wall samples were built, the wall begins to block the flow of powder into the melt pool. This results in the edge of the deposit being re-melted at the end of each layer but no new material being deposited. The continuous re-melting without the addition of new material aids in the removal of porosity and creates the observed porosity free region. This observation, along with the conclusion that an increased set-point and smaller layer thickness reduces the percentage of porosity, led to the hypothesis that increased laser power could lead to the removal of the porosity that was present in mixed elemental Ti-6Al-4V deposits.

To examine this hypothesis, a deposit was produced with a constant 1 kW laser power throughout the deposit. A constant 1 kW of power is the maximum possible with the deposition system used in this study. Coupled with the smaller layer thickness, these process parameters should produce as much heat as possible in the sample in an attempt to remove the porosity. Although this method did reduce the percentage of porosity down to approximately 6%, porosity was still present in the sample. Therefore, achieving a high enough laser power to essentially remove the porosity from the deposit would not be possible with this system. Further more, building a thin wall without the use of the feedback sensor and running at a constant 1 kW of laser power throughout the build is not an ideal operating condition for this system. The wall produced was not uniform in shape and was of poor physical quality when compared to previous Ti-6Al-4V deposits. This theory would have had more merit if it had removed all porosity in the sample, however this was not the case.

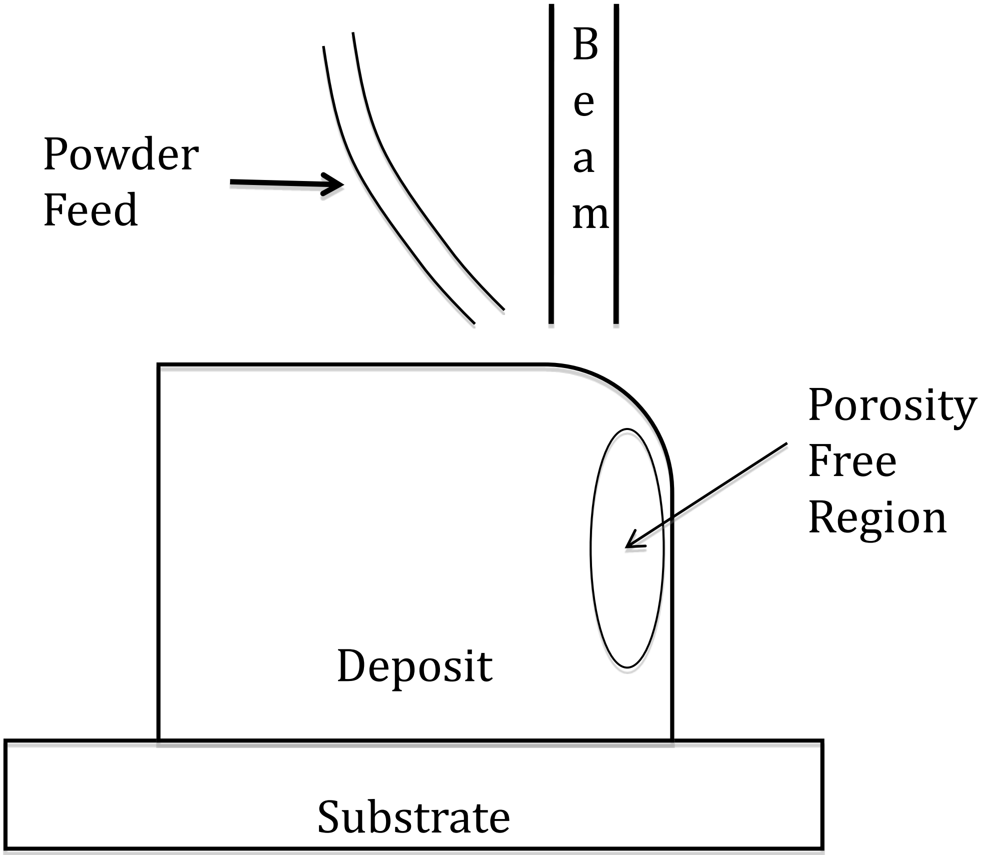

Figure 3.26. Schematic Diagram Depicting Porosity Free Region in Mixed Elemental Powder Ti-6Al-4V Deposits

An alternative method to remove the observed porosity in the Ti-6Al-4V samples produced with elemental powder mixes was desired. Examining the shape of the pores in the deposits, due to their round shape, it was likely that some form of gas was being released during the deposition process. The chemical composition of the elemental titanium powder did contain 0.1 wt% oxygen. However, the strong affinity of titanium to oxygen would tend to create a titanium oxide rather than out gassing the oxygen and forming pores.

Water vapor in the elemental powder mix was believed to be another possible cause of the porosity. The irregular shape of the elemental titanium powder may have made it more difficult for water vapor to escape the powder mix. In an effort to remove any trapped water vapor, the elemental titanium powder was heated before it was mixed with the Al/V master alloy. The elemental powder was heated in two different batches at

160 °C and 300 °C under an argon atmosphere for 40 minutes and then furnace cooled. After the powder was removed from the furnace it was placed in the glovebox where it was mixed with the Al/V master alloy. Deposits were then made using this powder mix, where the titanium had been heated, using the same deposition parameters as Sample #11. Those parameters can be seen in Table 3.4.

The results of these deposits indicate that heating the elemental powder before mixing does show merit. Figure 3.27 shows the plots of the porosity percentage and average pore size vs. location in the deposit for the two different temperatures of heated powder, as well as the un-heated powder for comparison. Heating the elemental titanium powder decreases the porosity percentage from approximately 8% to 3%. The titanium powder that was heated to 300 °C showed slight improvements when compared to the powder that was heated to 160 °C. However, this slight difference may be due to variations in the time it took to transfer the heated powder from the furnace to the glovebox. The reduction in porosity when the elemental powder was heated indicates that water vapor is a probable cause for the porosity. Ideally, all porosity would have been removed from the sample but this method, at a minimum, shows merit in improving sample quality.

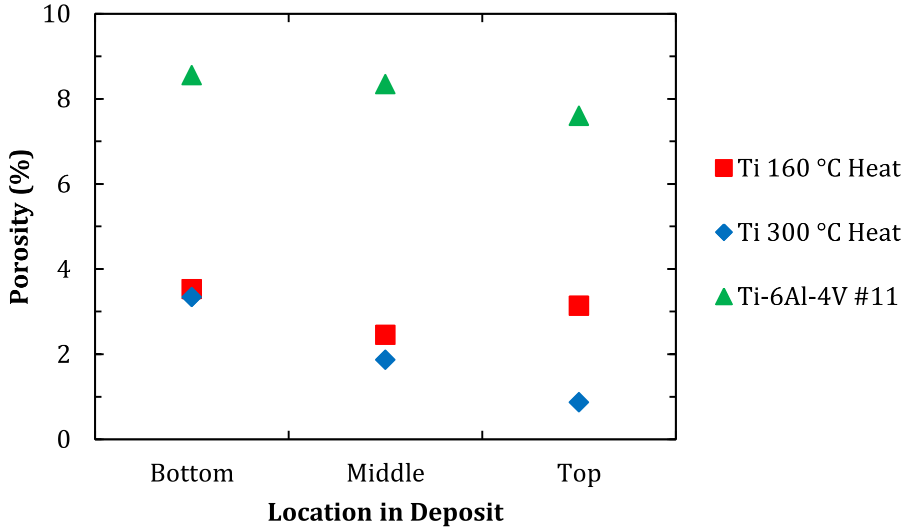

(a)

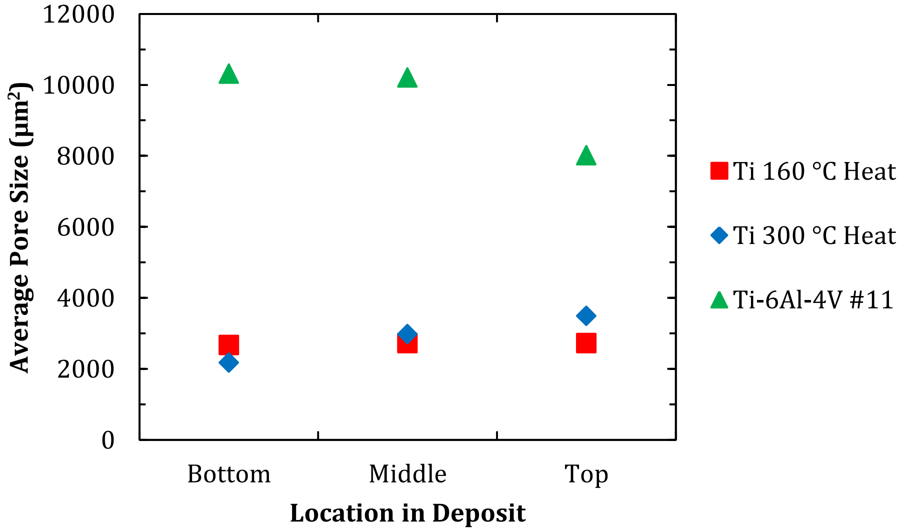

(b)

Figure 3.27. Plots of (a) Percentage Porosity and (b) Average Pore Size with Respect to Location in Deposit for Mixed Elemental Powder Ti-6Al-4V Deposits where Elemental Ti Powder had been Heated Prior to Mixing (Data points for the non-heated powder deposits are shown for comparison)

3.3.3. Microstructure Analysis. The microstructures of Ti-6Al-4V samples produced with pre-alloyed and mixed elemental powders can be seen in Figure 3.28 and 3.29 respectively. The microstructures of samples produced with both types of powder show similar structures and are consistent with results from literature [17, 18]. In the low magnification micrographs, columnar prior β grains are observed. The size and length of these grains shrinks in the mixed elemental deposits. This is likely a result of the level of porosity present in these samples. There is an observed variation in microstructure between prior β grains, but this observation is present in both types of samples.

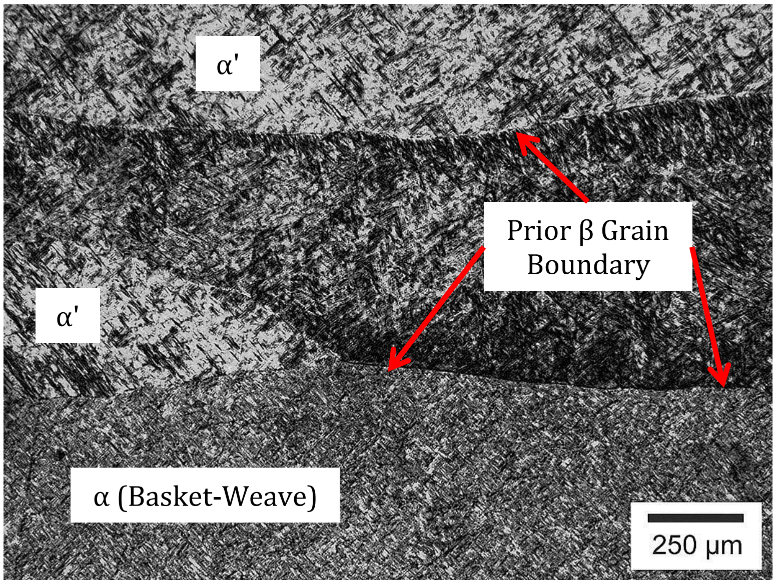

(a)

Figure 3.28. (a) Optical Micrograph of Ti-6Al-4V Pre-Alloyed Powder Deposit Microstructure at Low Magnification and (b) High Magnification

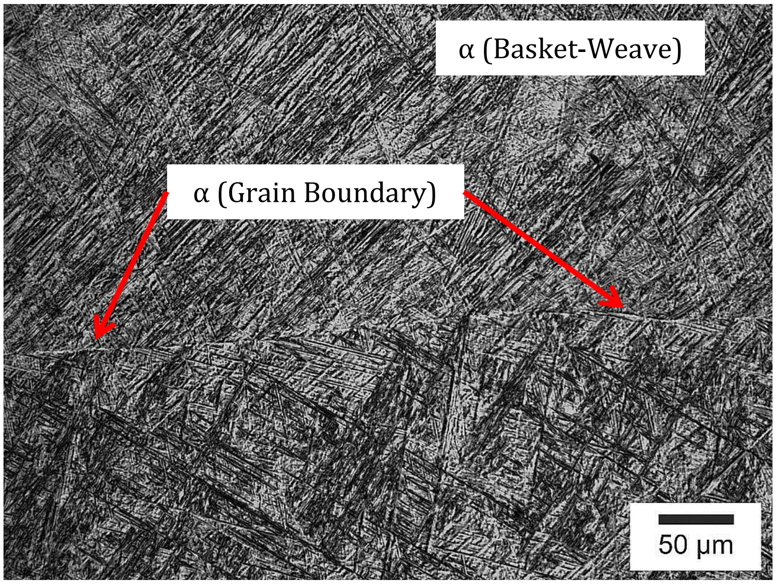

(b)

Figure 3.28. (cont.) (a) Optical Micrograph of Ti-6Al-4V Pre-Alloyed Powder Deposit Microstructure at Low Magnification and (b) High Magnification

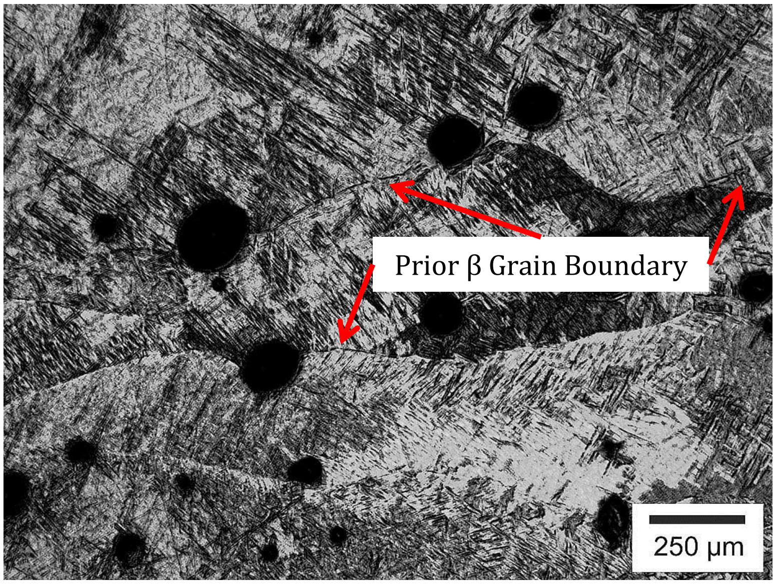

(a)

Figure 3.29. (a) Optical Micrograph of Ti-6Al-4V Mixed Elemental Powder Deposit Microstructure at Low Magnification and (b) High Magnification

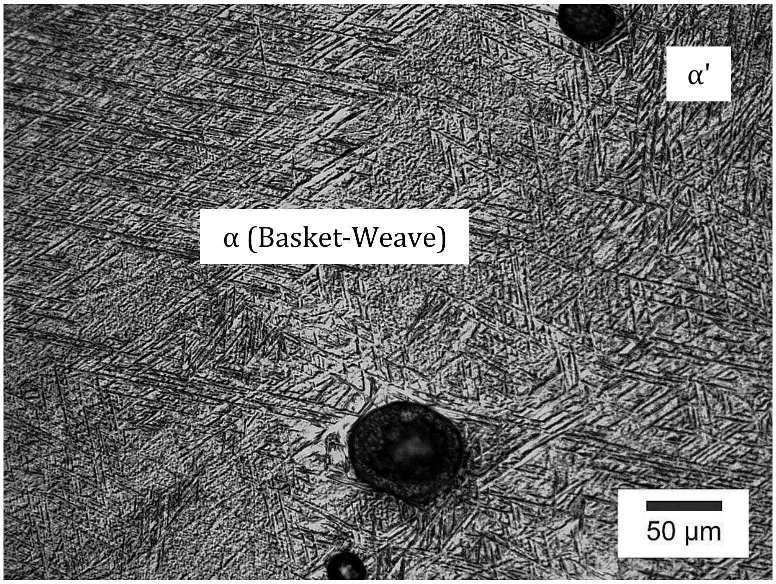

(b)

Figure 3.29. (cont.) (a) Optical Micrograph of Ti-6Al-4V Mixed Elemental Powder Deposit Microstructure at Low Magnification and (b) High Magnification

On a finer scale, the microstructures consist mainly of basket-weave α with regions of martensite α' in some areas. The martensitic α' structure forms when cooling rates are greater than 18 °C s^{-1} [19]. A higher quantity of α' was observed in the pre-alloyed samples indicating that cooling rates were higher. This also explains the increased α lath width in mixed elemental deposits due to decreased cooling rates. Although some minor differences are observed between the two types of samples, overall, the microstructures are similar. The presence of porosity in the mixed elemental powder deposits also impacts the resulting microstructure. Had all porosity been removed in mixed elemental powder deposits, it is likely that even better agreement in microstructure between the two types of samples would have been observed.

3.3.4. Mechanical Properties. Vickers microhardness values were used to compare the mechanical properties of laser deposited Ti-6Al-4V made with pre-alloyed powder and elemental powder mixes. Figure 3.30 (a) shows the measured microhardness values for pre-alloyed and mixed elemental deposits of Ti-6Al-4V when measured with a 500 g load and a 5 second dwell time. Pre-alloyed deposits had an average microhardness of 358±7 VHN while mixed elemental powder deposits had an average microhardness of 357±15. The mixed elemental powder deposits show a larger variation in microhardness throughout the deposit but excellent agreement is seen in the average microhardness value of deposits produced with both types of powder. These results are also consistent with values determined in previous studies [20, 21]. It should be noted that hardness values were only measured at Positions 1-4 for deposits made with elemental powder mixes.

As previously mentioned, Ti-6Al-4V deposits produced with mixed elemental powders exhibited significant levels of porosity. To avoid the influence of a pore on a hardness measurement, it was desired to take hardness measurements in a region with minimal porosity. In the case of these samples, a small region on the edge of the sample exhibited little to no porosity. This area was where microhardness testing was performed and not at the center of the sample as was done in other microhardness tests. Figure 3.30 (b) shows measured Vickers microhardness values for both types of deposits when measured with a 50 g load and a 5 second dwell time. Minimal variation in microhardness was observed between the retained β matrix and α lath structure. Pre-alloyed deposits had an average microhardness of 410±9 VHN when measured with a 50 g load and a 5 second dwell time and mixed elemental powder deposits had an average microhardness of 399±9 VHN when measured under the same conditions. These results indicate that consistent and comparable mechanical properties can be observed in Ti-6Al-4V laser deposits produced with both pre-alloyed powder and elemental powder mixes. This supports the idea than elemental powder mixes are a reliable alternative to pre-alloyed powder in laser-based additive manufacturing.

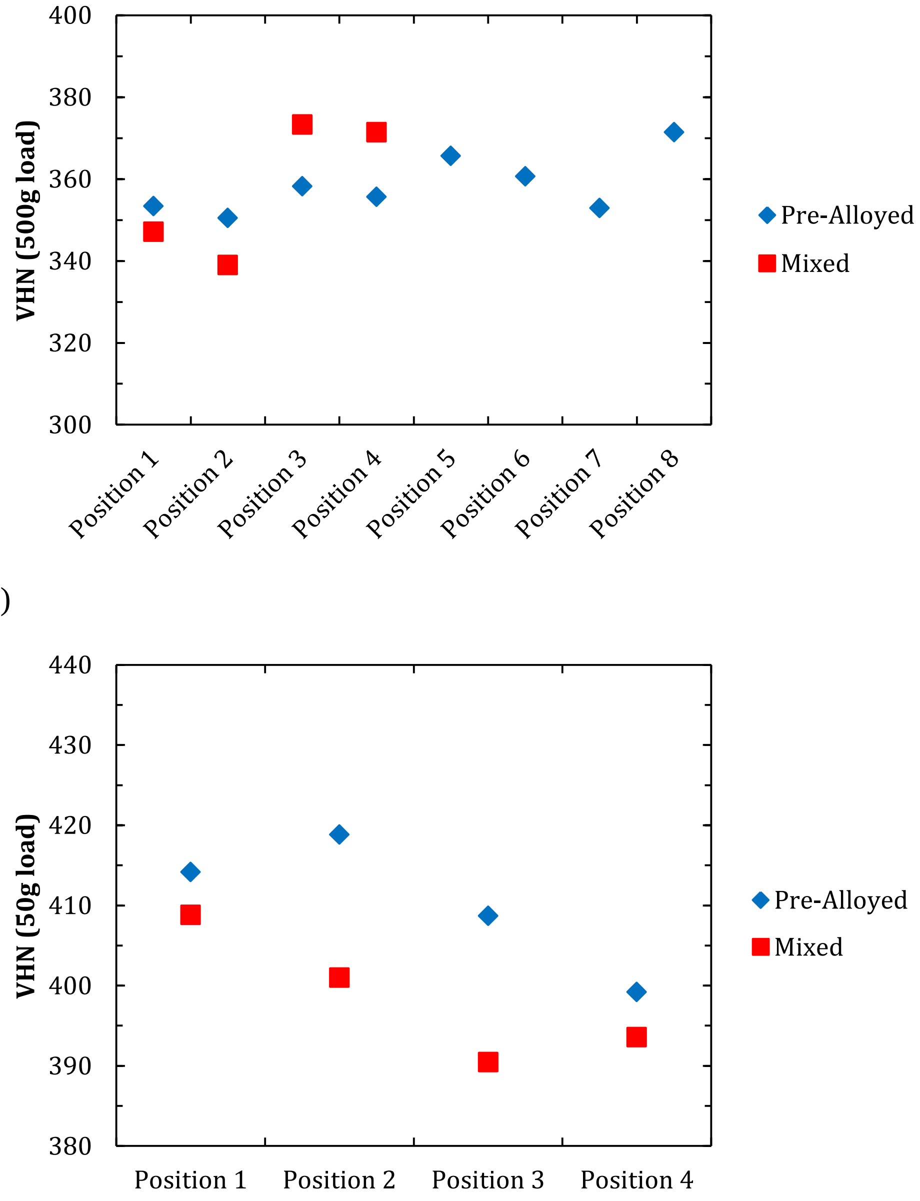

(a)

(b)

Figure 3.30. (a) Plot of Vickers Hardness vs. Position for Pre-Alloyed and Mixed Elemental Powder Ti-6Al-4V Deposits Measured with a 500 g Load and (b) 50 g Load

4. POTENTIAL ALLOY SYSTEMS

4.1. DETERMINATION OF ALLOY SYSTEMS

A study was performed to determine the potential number of alloys that could be produced using a mixed elemental powder technique. With a stock of elemental powders, it is feasible to produce several different alloys by varying the composition of the elemental powder mix. This method could be very advantageous to a company that relies on laser depositing components in several different alloys. Conventionally, a different pre-alloyed powder would have to be purchased for each alloy that is desired. This can become very costly when considering that a pre-alloyed powder may be purchased and only used once for a single customer. With an elemental powder mix technique a much smaller stock of powder could be purchased to produce an even larger number of alloys.

During this study, alloys in the Fe-Cr-Ni and Ti-Al-V systems were of main focus. It is very possible that additional alloys, other than the ones mentioned in this study, exist that would fit into the Fe-Cr-Ni or Ti-Al-V systems and be a great candidate to be used in a mixed elemental powder system. However, only certain types of alloys in these systems were examined. In this study, stainless steels were focused on within the Fe-Cr-Ni system where iron is the base metal and nickel and chromium make up the major alloying elements. Additionally, nickel-based superalloys and Inconel type alloys with higher nickel content were also examined. Within the Ti-Al-V system, alloys were chosen where titanium was the base metal and aluminum and vanadium were the major alloying elements.

It is also important to note that enthalpies of mixing were not considered in the selection of these alloys and only the alloy composition was examined. As mentioned previously, a negative enthalpy of mixing is crucial in the ability to successfully laser deposit an elemental powder mix. If the enthalpy of mixing of any of these alloys were determined to be positive or only slightly negative, the possibility of that alloy being produced through a mixed elemental powder method would significantly decrease. Enthalpy of mixing was not the focus of this study and therefore was not considered in the selection of alloys. However, it would be possible to calculate the enthalpy of mixing of any alloy proposed in the following sections and further examine its feasibility.

4.2. FE-CR-NI SYSTEM

Table 4.1, 4.2, and 4.3 [22] show potential austenitic, martensitic, and ferritic grades of stainless steel that could be produced based on an Fe-Cr-Ni system. A total of 13 potential austenitic stainless steel grades are achievable through a mixed elemental powder method. These selections were made based on the presence of chromium and nickel as core elements in the alloy with only additional minor alloying elements. Unless otherwise noted in Table 4.1, austenitic stainless steels will typically contain a maximum of 1.0 wt% silicon and 2.0 wt% manganese. These austenitic stainless steels also contain varying amounts of phosphorous and sulfur, which have a combined maximum total of less than 0.3 wt%. Austenitic stainless steels contain 16.0 – 25.0 wt% chromium and typically, high nickel content when compared to other stainless steels. Due to the high cost of nickel, cost becomes a limiting factor in the use of austenitic stainless steels over other categories of stainless steels. However, excellent mechanical properties, along with their corrosion resistance, make austenitic stainless steels a very useful material [23].

A listing of potential martensitic stainless steels to be produced through elemental powder mixes can be seen in Table 4.2. A total of 6 grades of martensitic stainless steel were selected as candidates. Unless otherwise noted, these martensitic stainless steels contain a maximum of 1.0 wt% manganese and silicon along with small amounts of phosphorous and sulfur. These grades are characterized by a typically low number of alloying elements, the main alloy being chromium. The low number of alloying elements is crucial in the ability to form a martensite structure within the microstructure [23]. Due to their strong, hard, and tough nature, martensitic stainless steels are commonly used in cutlery. However, martensitic stainless steels are the least corrosion resistant of the different categories of stainless steels and therefore also have the smallest volume of usage.

Ferritic stainless steels make up the last category of stainless steels examined in this study. Table 4.3 shows the potential ferritic stainless steel alloys that could be produced through an elemental powder mix using laser deposition. This group of stainless steels makes up the most corrosion and oxidation resistant alloys at the lowest cost in existence [23]. The cost of ferritic stainless steels compared to the cost of other stainless steels makes this group most attractive. The lack of nickel in a ferritic stainless steel compared to the higher nickel content in a 300 grade austenitic stainless steel makes them considerably less expensive. However, even without the presence of nickel, the properties of a ferritic stainless steel are comparable to those of an austenitic stainless steel. A total of 7 different grades of ferritic stainless steel can potentially be produced through a mixed elemental powder method.

Table 4.1. Potential Austenitic Stainless Steels

Type	C (wt%) max	Cr (wt %)	Ni (wt %)	Other (wt %)
301	0.15	16.0-18.0	6.0-8.0	…
302	0.15	17.0-19.0	8.0-10.0	…
303	0.15	17.0-19.0	8.0-10.0	2.0-3.0 Si
304	0.15	18.0-20.0	8.0-10.5	…
305	0.12	17.0-19.0	10.5-13.0	…
308	0.08	19.0-21.0	10.0-12.0	…
309	0.2	22.0-24.0	12.0-15.0	…
310	0.25	24.0-26.0	19.0-22.0	…
314	0.25	23.0-26.0	19.0-22.0	1.5-3.0 Si
316	0.08	16.0-18.0	10.0-14.0	2.0-3.0 Mo
317	0.08	18.0-20.0	11.0-15.0	3.0-4.0 Mo
330	0.08	17.0-20.0	34.0-37.0	0.75-1.5 Si
384	0.08	15.0-17.0	17.0-19.0	…

Table 4.2. Potential Martensitic Stainless Steels

Type	**C (wt%) max**	**Cr (wt %)**	**Ni (wt %)**	**Other (wt %)**
403	0.15	11.5-13.0	…	0.5 Si
410	0.15	11.5-13.5	…	…
414	0.15	11.5-13.5	1.25-2.50	…
416	0.15	12.0-14.0	…	1.25 Mn,
420	0.15 (min)	12.0-14.0	…	…
431	0.20	15.0-17.0	1.25-2.50	…

Table 4.3. Potential Ferritic Stainless Steels

Type	**C (wt%) max**	**Cr (wt %)**	**Ni (wt %)**	**Other (wt %)**
405	0.08	11.5-14.5	…	0.10-0.30 Al
409	0.08	10.5-11.75	…	0.75 max Ti
429	0.12	14.0-16.0	…	…
430	0.12	16.0-18.0	…	…
434	0.12	16.0-18.0	…	0.75-1.25 Mo
442	0.20	18.0-23.0	…	…
446	0.20	23.0-27.0	…	…

Although stainless steels consist mainly of iron, chromium, and nickel most grades of stainless steels are listed as containing additional elements. In many cases, these additional elements are trace elements such as carbon, phosphorous, sulfur, silicon, and manganese that total to be less than 5.0 wt% of the alloy. Most of these elements are the result of impurities during the steel making process that cannot be completely removed. On the other hand, some materials are added to increase the performance of the steel. In the case of manganese, it is often used to combat the detrimental behavior of sulfur by creating a less detrimental MnS phase within the steel. For an AISI designation of a stainless steel, the compositions of these elements are usually listed as a maximum allowable value within the stainless steel. With the use of an elemental powder mix, the impurities would not be present in the material and a purer grade of stainless steel could be produced.

In the case of some stainless steels, AISI designations call for additional alloying elements or a specific range of the trace elements previously mentioned. For example, 316 and 317 SS would require 2.0-4.0 wt. % molybdenum additions and 303, 304, and 330 SS would require specific amounts of silicon in the composition. These additional elements outside of the Fe-Cr-Ni system could potentially be obtained through a master alloy or as another pure elemental powder and then added to the Fe-Cr-Ni elemental powder mix. This would allow for the production of an accurate grade of stainless steel but still allow for the use of a mixed elemental powder method.

Ignoring the trace elements that are listed as maximum allowable content, if a company had a stock of elemental iron, chromium, nickel, and carbon; they could in theory, laser deposit 15 different grades of stainless steels. If aluminum, manganese, molybdenum, silicon, and titanium were added to the stock of elemental powders, that number would increase to 25 different grades of stainless steel. For a company involved in the laser additive manufacturing industry, the versatility provide from using elemental powder mixes could greatly increase their marketability to customers and consequently, their profits.

4.3 TI-AL-V SYSTEM

The second system examined in this study was the Ti-Al-V system. Each alloy selected in this system was classified as an Alpha/Near-Alpha, Beta/Near-Beta, or Alpha-Beta alloy. These classifications correspond to alloys, which contain mostly alpha, beta, or a mixture of alpha and beta respectively. Alpha alloys typically have good weldability characteristics, but are limited in strength since they are a single-phase material. With controlled additions of beta-stabilizing materials, a mixture of alpha and beta phases can be present below the beta transus. These two-phase titanium alloys are classified as alpha-beta alloys and can be considerably strengthened with appropriate heat treatments. Finally, alloys with large additions of beta-stabilizing materials can create a metastable beta microstructure and are therefore classified as beta alloys [24].

The Ti-Al-V system was further broken down into three different categories to examine possible alloy variations within the system. The first category examined was the 3-component system consisting solely of titanium, aluminum, and vanadium. Table 4.4 shows a listing of three potential Ti-Al-V alloys that could be produced through a mixed elemental powder method for use during laser deposition. The main alloy of focus in this group and also in this research is Ti-6Al-4V. As previously mentioned, Ti-6Al-4V is one of the most highly used titanium alloys making it an attractive alloy to be used in an elemental powder mix. This category shows that with a stock of just three elemental powders, potentially three different Ti-Al-V alloys could be laser deposited. Although this may not appear to be very beneficial, the cost associated with purchasing three elemental powders is likely much cheaper than purchasing three separate pre-alloyed powders.

Table 4.4. Possible Ti-Al-V Alloys

Type	**Ti (wt %)**	**Al (wt %)**	**V (wt %)**	**Classification**
Ti-6Al-4V	Bal.	6.0	4.0	Alpha-Beta
Ti-3Al-2.5V	Bal.	3.0	2.5	Alpha/Near-Alpha
Ti-16V-2.5Al	Bal.	2.5	16.0	Beta/Near-Beta

To attempt to increase the potential number of alloys in the Ti-Al-V system, two additional categories were created. This first of these categories was a 4-component Ti-Al-V-X system, where “X” is some additional alloying element. With the one additional alloying element, five additional alloys are added to the Ti-Al-V system. These alloys can be seen in Table 4.5 [24].

Table 4.5. Possible Ti-Al-V + Additional Element Alloys

Type	Ti (wt %)	Al (wt %)	V (wt %)	Other (wt %)	Classification
Ti-10V-3Al-2Fe	Bal.	3.0	10.0	2.0 Fe	Beta/Near-Beta
Ti-8V-5Fe-1Al	Bal.	1.0	8.0	5.0 Fe	Beta/Near-Beta
Ti-8Al-1Mo-1V	Bal.	8.0	1.0	1.0 Mo	Alpha/Near-Alpha
Ti-13V-11Cr-3Al	Bal.	3.0	13.0	11.0 Cr	Beta/Near-Beta
Ti-4Al-3Mo-1V	Bal.	4.0	1.0	3.0 Mo	Alpha-Beta

The final attempt to increase the number of potential alloys in the Ti-Al-V system was through replacing the vanadium with some different alloying element. The alloys fitting into this category can be seen in Table 4.6 [24]. Since vanadium is typically higher priced than some of the other alloying elements in the Ti-Al-V system, replacing it allowed for the addition of three potential alloys that may be of cheaper cost to produce.

Table 4.6. Possible Ti-Al + Additional Element Alloys

Type	Ti (wt %)	Al (wt %)	Other (wt %)	Classification
Ti-6.4Al-1.2Fe	Bal.	6.4	1.2 Fe	Alpha-Beta
Ti-5Al-2.5Sn	Bal.	5.0	2.5 Sn	Alpha/Near-Alpha
Ti-7Al-4Mo	Bal.	7.0	4.0 Mo	Alpha-Beta

With these three categories in the Ti-Al-V system, a total of 11 potential alloys could be laser deposited using a mixed elemental powder technique. These 11 alloys could be produced from a stock of only 7 different elemental powders. These options and versatility could prove to be invaluable to a company hoping to laser deposit Titanium alloys. If a company was only interested in depositing stainless steels and titanium alloys versatility would improve even further. With the coupling of the C-Fe-Cr-Ni and Ti-Al-V systems, 22 different alloys could potentially be deposited with only 7 elemental powders. If molybdenum was added to the stock of elemental powders, the number of alloys increases to 28. These options and versatility could not only save the company money from the costs of expensive pre-alloyed powder, but also more importantly, allow them to market to a whole new line of consumers.

4.4. NICKEL-BASED SUPERALLOYS AND INCONEL TYPE ALLOYS

Nickel-based superalloys and Inconel type alloys were the final group of alloys examined for use in a mixed elemental powder method. These alloys consist mainly of nickel, chromium, and iron making them a good fit for the Fe-Cr-Ni system. One of the important alloys in this group is Inconel 625. Inconel 625, is a nickel-based superalloy with uses in marine, chemical, and aerospace applications. The complex shape and design of many Inconel 625 parts makes production costs with typical machining methods very high. [25, 26]. These high production costs make laser-based additive manufacturing an appropriate process to produce Inconel 625 components. Inconel 718 is another nickel-based superalloy, often used in aircraft engines, of which components are produced using laser-based additive manufacturing [27, 28].

The high use of these alloys in laser-based additive manufacturing makes them valid candidates to be examined for use in a mixed elemental powder method. Table 4.7 lists the compositions of 625, 718, and other possible Inconel type alloys that could potentially be laser deposited using a mixed elemental powder method [29]. As can be seen in this table, the compositions of these alloys is much more complex than typical stainless steels. Although the composition may be complex, the potential to laser deposit these alloys with elemental powder mixes is still present. It was already shown that coupling the Ti-Al-V and Fe-Cr-Ni systems would be beneficial for potential alloys in the Ti-Al-V system. For nickel-based superalloys and Inconel type alloys, the coupling with the Ti-Al-V system would prove to be quite valuable since many of these alloys contain small additions of aluminum and titanium. However, even with the coupling of these two systems, there are several alloying elements that are still unaccounted for. Some of these alloys contain additions of molybdenum and niobium. These elements would need to be added outside of the Ti-Al-V or Fe-Cr-Ni systems. Other elements such as cobalt, carbon, manganese, silicon, and copper are minor alloying elements and would still need to be accounted for. Regardless of the complexity, these alloys could all potentially be used in a mixed elemental powder system.

Table 4.7. Possible Nickel-Based Super Alloys and Inconel Type Alloys

Alloy	**Composition, wt%(a)**											
	Ni	**Cr**	**Fe**	**Co**	**Mo**	**Nb**	**Ti**	**Al**	**C**	**Mn**	**Si**	**Other**
Nickel-Chromium-Iron Alloys												
Alloy 600	72.0 min(b)	14.0–17.0	6.0–10.0	…	…	…	…	…	0.15	1	0.5	0.50 Cu
Alloy 601	58.0–63.0	21.0–25.0	bal	…	…	…	…	1.0–1.7	0.1	1	0.5	1.0 Cu
Alloy 625	58.0 min	20.0–23.0	5	1	8.0–10.0	3.15–4.15(c)	0.4	0.4	0.1	0.5	0.5	…
Alloy 690	58.0 min	27.0–31.0	7.0–11.0	…	…	…	…	…	0.05	0.05	0.5	0.50 Cu
Alloy 718	50.0–55.0(b)	17.0–21.0	bal	1	2.80–3.30	4.75–5.50(c)	0.65–1.15	0.20–0.80	0.08	0.35	0.35	0.30 Cu
Alloy 751	70.0 min(b)	14.0–17.0	5.0–9.0	…	…	0.7–1.2(c)	2.0–2.6	…	0.1	1	0.5	0.50 Cu
Iron-Nickel Chromium Alloys												
Alloy 800	30.0–35.0	19.0–23.0	39.5 min	…	…	…	0.15–0.60	0.15–0.60	0.1	1.5	1	…
Alloy 825	38.0–46.0	19.5–23.5	22.0 min	…	2.5–3.5	…	0.6–1.2	0.2	0.05	1	0.5	…
Alloy 925	44	21	28	…	3	…	2.1	0.3	0.01	…	…	…
Controlled-Expansion Alloys												
Alloy 902	41.0–43.5(b)	4.9–5.75	bal	…	…	…	2.2–2.75	0.3–0.8	0.06	0.8	1	…

(a) Single values are maximum values unless otherwise indicated.

(b) Nickel plus Cobalt content.

(c) Niobium plus Tantalum content.

5. CONCLUSIONS

Results of this study confirm that elemental powder mixes can be used in LAM. A major concern with the use of elemental powder mixes is that adequate mixing of the powders is present to produce a homogeneous deposit. All deposits produced in this study with mixed elemental powders were examined with EDS line scans and all deposits had uniform compositions. Deposits of 316 SS produced with mixed elemental powders and pre-alloyed powders both exhibited a microstructure with austenite cells in a matrix of second-phase ferrite. Following a post processing heat treatment, pre-alloyed powder deposits and mixed elemental powder deposits had hardness values of 154±5 VHN and 152±9 respectively. Similar microstructures and mechanical properties make an Fe-17Cr-12Ni elemental powder mix a possible substitute to the conventional pre-alloyed 316 SS powder used in LAM.

Unlike 316 SS deposits, deposits produced with 430 SS did not exhibit similar mechanical properties or microstructure between the two types of powder. The microstructure of pre-alloyed powder deposits contained a ferrite matrix with regions of a martensitic structure, while the elemental powder mix deposits exhibited a fully ferritic microstructure with columnar ferrite grains. The different microstructures between the two types of deposits also lead to different hardness values in the as deposited state. However, even after a post-processing heat treatment, differing hardness values were observed. Pre-alloyed deposits exhibited a Vickers hardness of 210±6 VHN while mixed elemental powder deposits exhibited a Vickers hardness of 130±2 VHN following an annealing treatment at 770 °C for 1 hour. These large differences should not be observed even in a mixed elemental powder deposit. After further investigation of chemical composition, it is likely that the martensite present in the pre-alloyed deposit is attributing to the higher hardness values. To consider replacing 430 SS pre-alloyed powder with an Fe-17Cr elemental powder mix, additional experiments may need to be performed to fully understand why different microstructures and mechanical properties were being observed. By repeating the experiment again, the expected results may be observed indicating that an anomaly in the experimental procedure occurred. However, the results of this study indicate that deposits made of 430 SS and an Fe-17Cr elemental powder mix are not comparable.

Ti-6Al-4V deposits with pre-alloyed powder and elemental powder mixes did exhibit similar microstructures and mechanical properties. Microstructures consisted mainly of basket-weave α along with regions of a martensitic α' structure within prior β grains. The microstructure in the elemental powder mixes was also characterized by a larger α lath width, which indicates slower cooling rates were observed in these samples. Vickers hardness values also exhibited excellent agreement with pre-alloyed powder deposits and mixed elemental powder deposits have hardness values of 358±7 and 357±15 respectively. Although good agreement in mechanical properties and microstructure was observed, mixed elemental powder deposits contained high levels of porosity. LAM is capable of producing fully dense parts so this observation was unexpected. In an effort to remove porosity, elemental Titanium powder was heated before it was mixed with an Al/V master alloy powder to make a Ti-6Al-4V elemental powder mix. This procedure did lead to a reduction in porosity percentage, however, 1-4% porosity was still present. For a Ti-6Al-4V elemental powder mix to replace a pre-alloyed powder in a LAM environment, this remaining porosity would need to be removed. Even though there was agreement in mechanical properties and microstructure, a consumer would likely desire a fully dense part.

The alloys that were represented with elemental powder mixes in this study are alloys that are commonly deposited using LAM. Where elemental powder mixes can really benefit LAM, is through their use to develop new alloys. Many of the alloys currently being used in LAM were developed long before LAM technology was available and were designed for other manufacturing methods. Elemental powder mixes allow a user to quickly and easily modify the composition of a powder mix and therefore the resulting alloy. This makes research into developing new alloys specific to LAM much more achievable. Ultimately, new alloys with superior properties can be developed for LAM aided by the use of elemental powder mixes.

Inherently, there is some lack of control in the deposition system. During each deposit the amount of powder fed, laser power absorbed, peak temperatures, and cooling rates all vary slightly. Efforts are made to make sure these variations are minimal but ultimately there is some difference. When the fact that different powder shapes and size distributions are being compared, the impact of these variations is increased. In an ideal experimental setup, pre-alloyed and elemental powders would be purchased from the same manufacturer with the same shape and size distribution. The deposition system would be precisely controlled to feed the same amount of powder every time and the temperature profile of the deposit during deposition would be reproducible. At present time, LAM is still a relatively new technology and in a real world manufacturing environment it would be difficult to have precise control over this many experimental variables. However, the results of this study indicate that even with a lack of precise control of these variables, deposits produced with elemental powder mixes have advantages and can compete with pre-alloyed powder deposits.

APPENDIX

MICROSTRUCTURE SIMULATION

As a side project to this research, a simulation was desired to simulate the as-received microstructure of stainless steel and Ti-6Al-4V substrates for laser deposition. This simulation was just a small piece of a much larger simulation that would simulate the entire laser deposition process. The first task was to choose an appropriate computational method for the simulation. After a thorough literature review, a Monte Carlo type simulation was chosen as the method to complete this task [30-32]. Further investigation of Monte Carlo type microstructure simulations, lead to the discovery of the Mesoscale Microstructure Simulation Project (MMSP). MMSP is an open source code project developed by Carnegie Mellon University that serves as a starting point for many different types of microstructure simulations. The anisotropic Monte Carlo grain growth model was chosen as the starting point for this work.

Most Monte Carlo models for microstructure simulation, and the MMSP code specifically, all have one thing in common and that is that they are all variations of the Potts Model. The simulation begins by dividing the domain into many different lattice sites. Each site is then given a random spin or orientation Q_i where $1<Q_i<Q$ with Q being the maximum number of different spins or orientations. In the simulation in this work, each Q_i corresponds to a Grain ID of specific crystallographic orientation. This is where the main difference between the Potts Model and most Monte Carlo type models lies. The Potts Model conventionally limits each site to having spin 1 or spin 0, corresponding to an up and down spin at that lattice site. However, each grain in a microstructure has a different orientation and therefore, many different orientations are considered in a Monte Carlo model. This leads to the next step in the simulation where each lattice site is assigned a unique crystallographic orientation. Grain ID's are not initially given unique crystallographic orientations in the MMSP code, but these orientations were implemented in a similar fashion to previous work from the MMSP author [33]. This was done through the use of the three phi values seen in Equation (A.1).

$$\begin{aligned} \phi_1 &= 2\pi r_1 \\ \Phi_2 &= \cos^{-1}(1-2r_2) \\ \varphi_3 &= 2\pi r_3 \end{aligned} \tag{A.1}$$

Now that each lattice site has been given a random Grain ID with unique orientation, the Monte Carlo process can begin. A lattice site is chosen at random and the total energy of the system is calculated with that lattice sites' Grain ID. Next, the energy of the system is recalculated by changing the selected lattice sites' Grain ID to that of one of its neighboring lattice sites. This allows for the calculation of an energy change from the initial Grain ID to the neighboring Grain ID. The energy in the system is calculated using Equation (A.2), where E_0 is the energy from a reference state, N is the total number of lattice sites in the system, $\gamma(\theta_{ij})$ corresponds to a energy per unit area of a grain boundary with the disorientation angle θ_{ij}, and finally $\chi(i,j)$ represents the relationship between the Grain ID at site i and it's neighboring Grain ID at site j.

$$E = E_0 + \sum_{i=1}^{N}\sum_{j=1}^{N}\gamma(\theta_{ij})\chi(i,j) \tag{A.2}$$

Since the goal of the simulation is to grow grains into a representative microstructure, grain boundary migration is dependent on a reduction in energy. Therefore, if a change to a random neighboring Grain ID at the selected site leads to a reduction in total system energy ($\Delta E \leq 0$), that Grain ID will be selected based on a certain probability. This probability, P, can be described by the relation seen in Equation (A.3) and is dependent on grain boundary mobility and energy. In Equation (A.3) M_{max} and γ_{max} represent the maximum allowable grain boundary energy and mobility within the system for the given simulation.

$$P = \begin{cases} \dfrac{M(\theta_{ij})}{M_{max}}\dfrac{\gamma(\theta_{ij})}{\gamma_{max}} & \Delta E \leq 0 \\ \dfrac{M(\theta_{ij})}{M_{max}}\dfrac{\gamma(\theta_{ij})}{\gamma_{max}}\exp\left[-\dfrac{\Delta E}{E^{*}kT}\right] & \Delta E > 0 \end{cases} \tag{A.3}$$

Equation (A.2) and (A.3) introduce the idea of a disorientation angle. From the unique orientation given to each Grain ID by the three phi values in Equation (A.1), a misorientation angle is used to describe the rotation required to rotate a set crystal axes into coincidence with another crystal. The disorientation angle can then be defined as the smallest rotation angle from all symmetrically equivalent misorientations. By default, the MMSP project does not calculate misorientation and disorientation angles. However, a texture sub-routine written by the authors of the MMSP project can be appended to the code to perform this task. The misorientation and disorientation angles are necessary due to the use of Read-Shockley type grain boundary energy and mobility functions, which are dependent on these angles. The grain boundary energy and mobility functions can be seen in Equations (A.4) and (A.5), where θ and θ’ represent the disorientation angle and a maximum disorientation angle in the system respectively.

$$\gamma(\theta) = \begin{cases} \dfrac{\theta}{\theta'}\left[1 - \ln\left(\dfrac{\theta}{\theta'}\right)\right] & \theta \le \theta' \\ 1 & \theta > \theta' \end{cases} \tag{A.4}$$

$$M(\theta) = \begin{cases} \dfrac{\theta}{\theta'}\left[1 - \ln\left(\dfrac{\theta}{\theta'}\right)\right] & \theta \le \theta' \\ 1 & \theta > \theta' \end{cases} \tag{A.5}$$

The process described in Equations (A.2-A.5), the selection of a site and random and the change to a different Grain ID based on system energy and probability basically describes part of a single Monte Carlo time step (MCS). A single MCS is completed when the total number of random lattice sites selected is equal to the total number of lattice sites in the computation domain. After hundreds of MCS, Grain ID’s with favorable orientations emerge and a microstructure becomes apparent.

With accurate equations implemented in the Monte Carlo portion of the code, simulations could be performed that would produce representative substrate microstructures. Figure A.1 shows the resulting microstructure after 100 MCS on a 128 x 128 2D grid. This simulation is a good starting point, but improvements should be made.

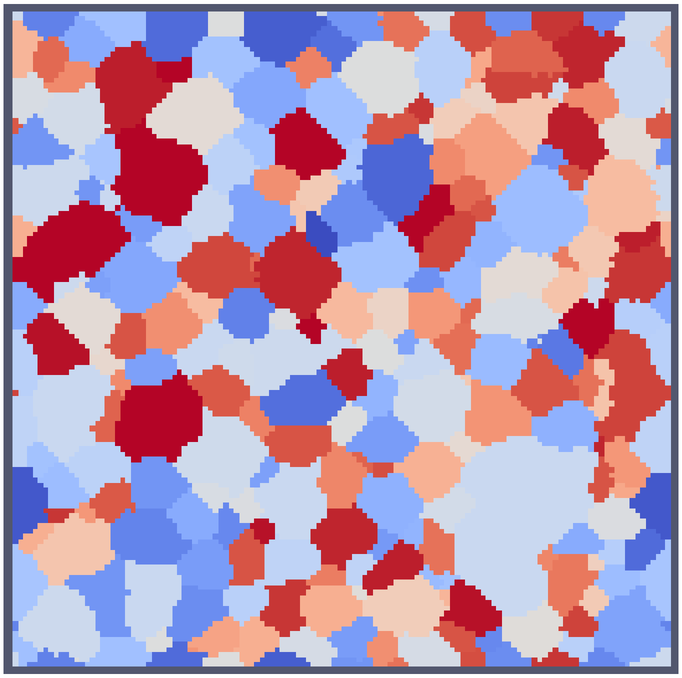

Figure A.1. 2D Microstructure Simulation on 128 x 128 Grid Ran for 100 MCS

From Figure A.1, it can be seen that most grain edges appear “blocky”. This is due to a lack of resolution in the simulation and is not how an actual microstructure would appear. By running the simulation on a larger grid and for more MCS, this issue can easily be resolved. A simulation on a larger grid ran for more MCS can be seen in Figure A.2 and it is observed that the grain edges become much clearer. When this simulation is compared to an actual stainless steel microstructure, seen in Figure A.3, excellent resemblance is observed. This confirms that the code is running and functioning as expected.

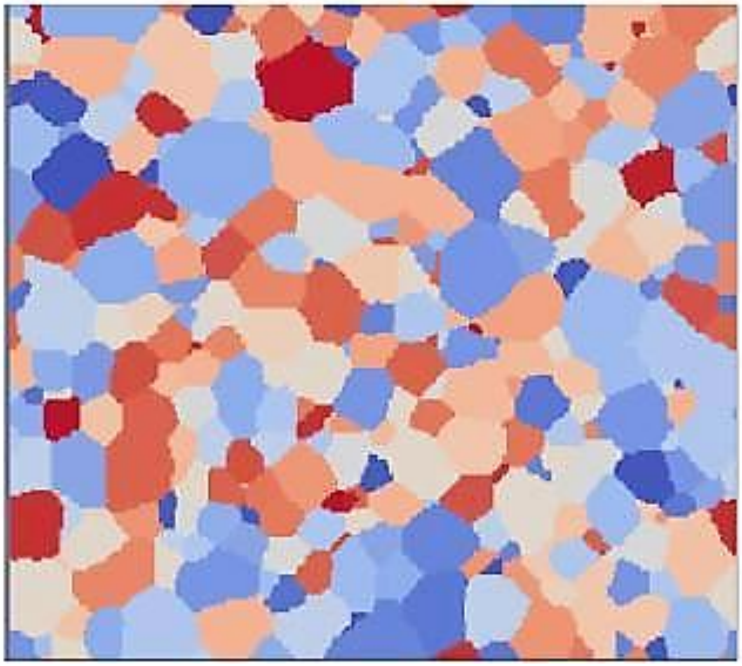

Figure A.2. Microstructure Simulation on 256 x 256 Grid Ran for 500 MCS

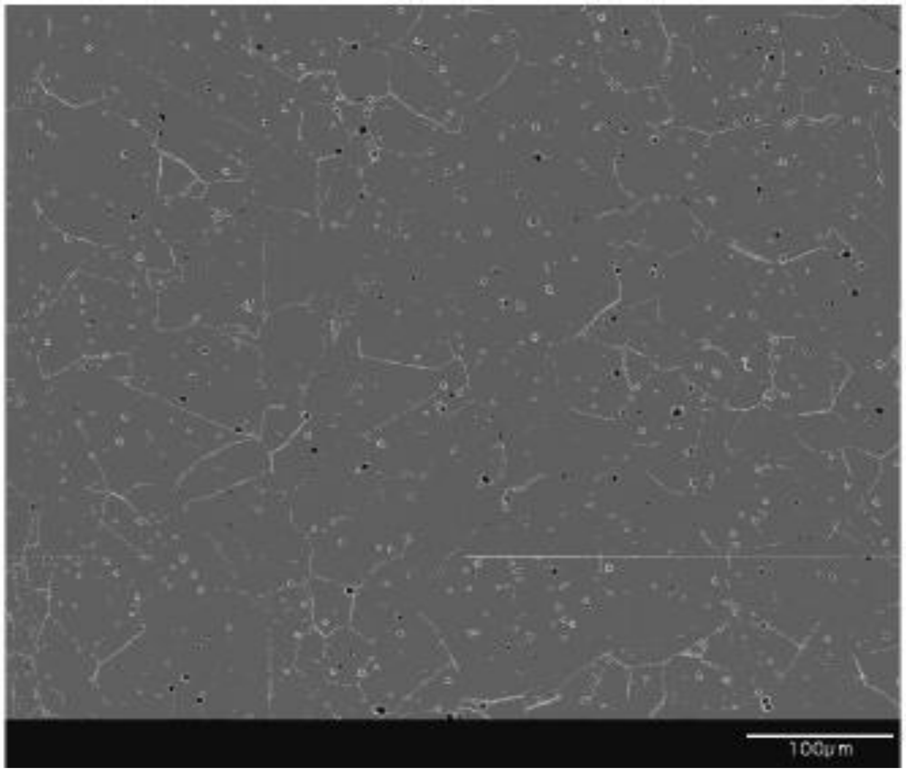

Figure A.3. Microstructure of 316 SS Substrate

The next issue lies with computation time. The simulation in Figure A.2 was determined to have approximately 150 grains but took 4 hours computational time to simulate on a single core. With a physical substrate size of 3 x 3 x 3 mm, roughly 216,000 grains would be present in the substrate if the average grain size were assumed to be 50 μm. This equates to approximately 3,600 grains present in a 2D slice of the substrate. If an average grain size of 100 μm is assumed, 27,000 grains would be in the substrate and 900 grains should be observed in a 2D slice. Obviously, these numbers are significantly larger than anything that had been simulated at this point.

The advantage of simulating a stainless steel microstructure is that most grains are equiaxed and there is little variation throughout the substrate. Potentially, this allows for smaller 2D simulations to be placed side-by-side creating a much larger simulation. This simplification is possible due to the mirror boundary conditions that are possible in the MMSP code. In reality, this is not how the actual substrate microstructure appears, but serves as a good simplification to the simulation and solves the issue of large computation times. Figure A.4 shows how smaller simulations could be “pieced” together to get a larger number of grains without increasing computational time.

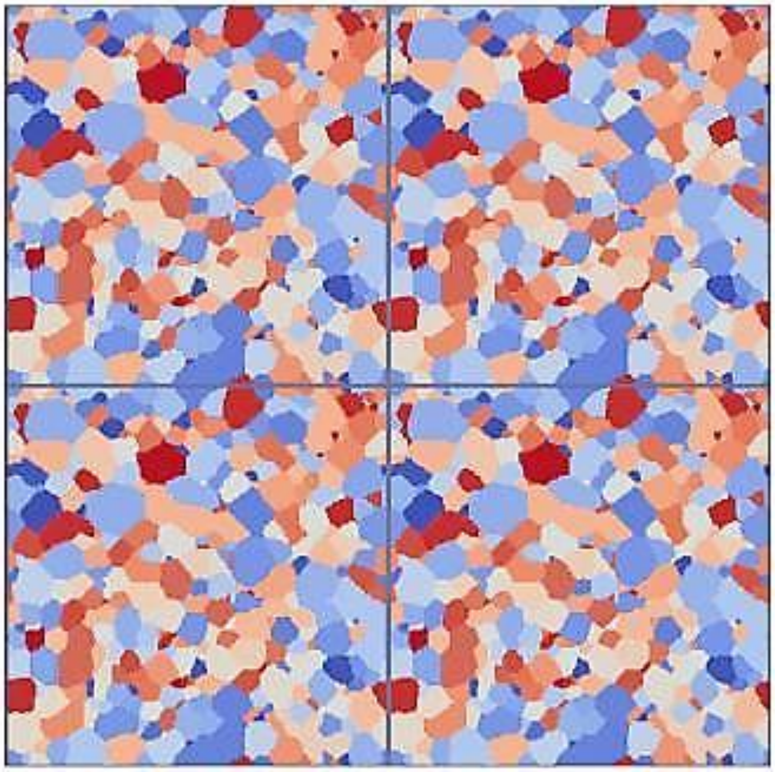

Figure A.4. Four 256 x 256 Simulations Stacked Together

Once the simulation of a stainless steel microstructure was completed, work began on trying to simulate the as-received microstructure of a Ti-6Al-4V substrate. Due to the two-phase nature of a Ti-6Al-4V microstructure, a simulation of that microstructure is much more complex than the simulation of a single-phase material like stainless steel. Holm et. al. and Zheng et. al. have done work using a Monte Carlo method to simulate grain growth in a two-phase material [34, 35]. Although they have shown this is possible, many modifications would be required to the stainless steel code and overall the code would be much more complex. Therefore, an attempt to simplify the simulation by only simulating one phase of the Ti-6Al-4V microstructure was examined. This would require adequate justification for this simplification though.

After looking at a Ti-6Al-4V phase diagram, it can easily be seen how this simplification can be justified. The important part of the Ti-6Al-4V, seen in Figure A.5, is the beta transus which occurs at 980 °C [36]. Above the beta-transus, the microstructure becomes entirely beta phase and no alpha phase is present. As previously mentioned, this microstructure simulation was a small part of a much larger simulation. The as-received substrate microstructure simulation would serve as an input for a solidification model. The solidification model only required the microstructure at a high temperature just before melting began. Therefore, any microstructure simulated between the beta-transus temperature (980 °C) and the melting temperature (1604-1660 °C) would consist only of beta phase Ti-6Al-4V and be a valid input for the solidification model.

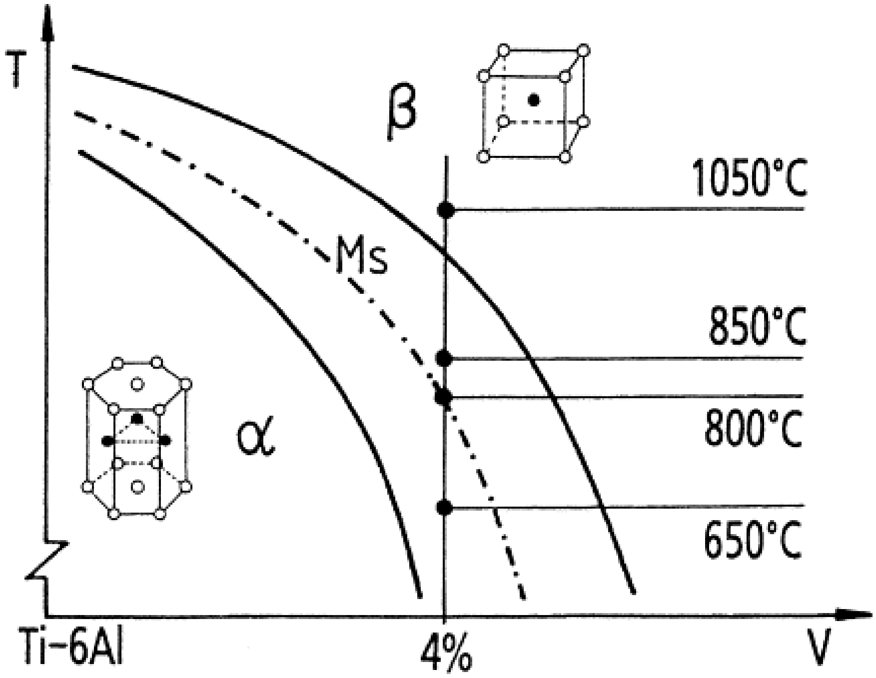

Figure A.5. Pseudo-Binary Equilibrium Phase Diagram for Ti-6Al-4V

To confirm the accuracy of the Ti-6Al-4V microstructure simulation, the prior-beta grain structure in the substrate material being represented must be determined. The easiest method to perform this is through the use of Electron Backscatter Diffraction (EBSD) and Orientation Image Mapping (OIM). Using a SEM to perform EBSD, orientation information about the grains in the substrate material will be collected and OIM software will make the grains and areas of similar orientations in the substrate visible. An example of using EBSD and OIM to construct prior-beta grains can be seen in Figure A.6 [37]. Areas in the microstructure having the same color indicate that all grains in that region have similar orientation. In Figure A.6 (a), an orientation tolerance of 2° is used and (b) a tolerance of 5° is used in Figure A.6 leading to larger areas of similar orientation. It should be noted that white and black lines in these images represent grain boundaries. These grains could contain either alpha or beta Ti-6Al-4V at room temperature but each area of similar orientation represents a prior-beta grain from when the material was above the beta-transus temperature. The microstructure simulation should ultimately represent the prior-beta grain structure of the intended Ti-6Al-4V substrate material. At this time, work is being done to determine the prior-beta grain structure in a Ti-6Al-4V substrate. Once this is completed, simulation parameters can be adjusted to match simulation output to experimental results.

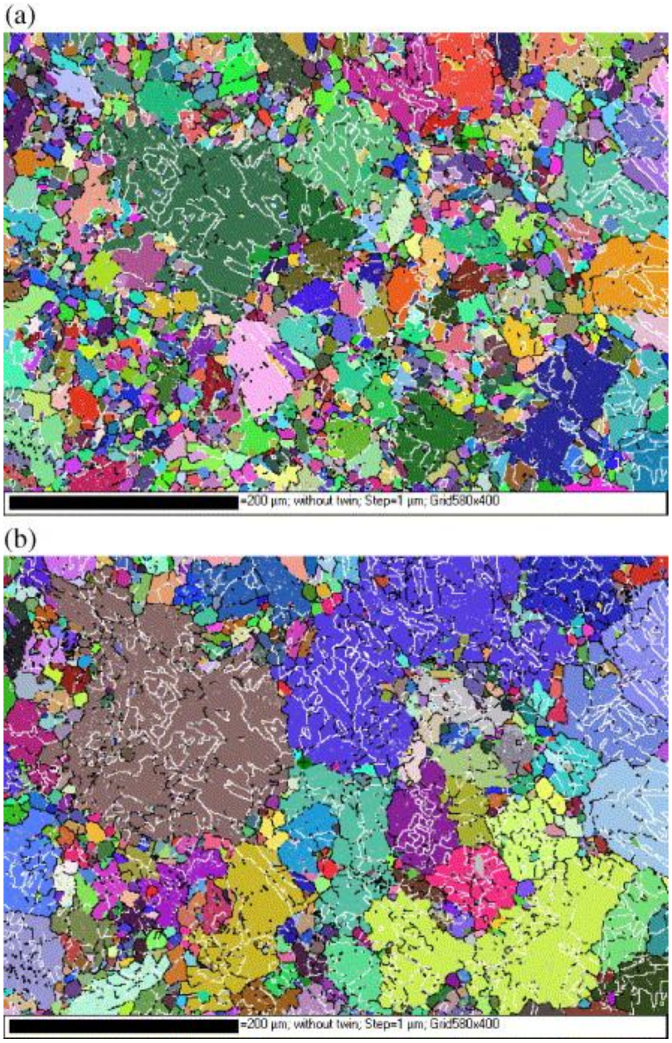

Figure A.6. OIM Image Showing Prior-Beta Grain Structure in Ti-6Al-4V. An Orientation Tolerance of 2° is Seen in (a) and a Tolerance of 5° is Seen in (b)

The final step of this work involves running the simulation in parallel on many cores. This is the most appropriate way to produce an accurate simulation of an as-received substrate microstructure and also optimize computational time. At this time, issues with the code not compiling in parallel have been solved. The MMSP code is stated as being MPI ready and will compile without modification in parallel. However, during this work, the code was unable to compile in MPI without modification. It is possible that this is due to different compilers or MPI versions being used than what the MMSP code was designed for. Whatever the issue, the code is now running in parallel and being sent to the University of Missouri – Columbia cluster to be performed on numerous cores. This will result in a simulation of an as-received stainless steel substrate microstructure.

BIBLIOGRAPHY

[1] “Materials Properties Handbook: Titanium Alloys”, 1993, ASM International, Materials Park, OH.

[2] G.A. Ravi, X.J. Hao, N. Wain, X. Mu, and M.M. Attallah, “Direct Laser Fabrication of Three Dimensional Components using SC420 Stainless Steel”, *Mater. Design*, 2013, vol. 47, pp. 731-736.

[3] J. Dutta Majumdar, A. Pinkerton, Z. Liu, I. Manna, and L. Li, “Microstructure Characterization and Process Optimization of Laser Assisted Rapid Fabrication of 316L Stainless Steel”, *Appl. Surf. Sci.*, 2005, vol. 247, pp. 320-327.

[4] J. Dutta Majumdar, A. Pinkerton, Z. Liu, I. Manna, and L. Li, “Mechanical and Electrochemical Properties of Multiple-Layer Diode Laser Cladding of 316L Stainless Steel”, *Appl. Surf. Sci.*, 2005, vol. 247, pp. 373-377.

[5] T. Takeda, W.M. Steen, and D.R.F. West, “Laser Cladding with Mixed Powder Feed”, International Congress on Applications of Lasers & Electro-Optics (ICALEO), 1984, vol. 44, pp. 151-158.

[6] W. Liu, and J.N. DuPont, “Fabrication of Functionally Graded TiC/Ti Composites by Laser Engineered Net Shaping”, *Scirpta Mater.*, 2003, vol. 48, pp. 1337-1342.

[7] R. Banerjee, P.C. Collins, A. Genc, and H.L. Fraser, “Direct Laser Deposition of In Situ Ti-6Al-4V-TiB Composites”, *Mater. Sci. Eng. A*, 2003, vol. 358, pp. 343-349.

[8] K.I. Schwendner, R. Banerjee, P.C. Collins, C.A. Brice, and H.L. Fraser, “Direct Laser Deposition of Alloys from Elemental Powder Blends”, *Scripta Mater.*, 2001, vol. 45, pp. 1123-1129.

[9] P.C. Collins, R. Banerjee, and H.L. Fraser, “The Influence of the Enthalpy of Mixing During the Laser Deposition of Complex Titanium Alloys Using Elemental Blends”, *Scripta Mater.*, 2003, vol. 48, pp. 1445-1450.

[10] A. Takeuchi and A. Inoue, “Calculations of Mixing Enthalpy and Mismatch Entropy for Ternary Amorphous Alloys”, *Mater. T. JIM.*, 2000, vol. 41, no. 11, pp. 1372-1378.

[11] A. Takeuchi and A. Inoue, “Classification of Bulk Metallic Glasses by Atomic Size Difference, Heat of Mixing and Period of Constituent Elements and Its Application to Characterization of the Main Alloying Element”, *Mater. T. JIM.*, 2005, vol. 46, no. 12, pp. 2817-2829.

[12] J.W. Elmer, S.M. Allen, and T.W. Eagar, "Microstructural Development during Solidification of Stainless Steel Alloys", *Metall. Trans. A*, 1989, vol. 20A, pp. 2117-2131.

[13] Tolosa, F. Garciandia, F. Zubiri, F. Zapirain, and A. Esnaola, "Study of Mechanical Properites of AISI 316 Stainless Steel Processed by 'Selective Laser Melting' Following Different Manufacturing Strategies", *Int. J. Adv. Manuf. Tech.*, 2010, vol. 51, pp. 639-647.

[14] J. Charles, J.D. Mithieux, P.O. Santacreu, and L. Peguet, "The Ferritic Stainless Steel Family: The Appropriate Answer to Nickel Volatility?", *Rev Metall-Paris,* 2009, vol. 106, pp. 124-139.

[15] M.O.H. Amuda, and S. Mridha, "Effect of Energy Input on Microstructure and Hardness of TIG Welded AISI 430 – Ferritic Stainless Steel", *Adv. Mater.*, 2011, vols. 264-265, pp. 390-396.

[16] "Iron-Chromium (Fe-Cr) Phase Diagram", Computational Thermodynamics Inc., http://www.calphad.com/iron-chromium.html

[17] E. Brandl, A. Schoberth, and C. Leyens, "Morphology, Microstructure, and Hardness of Titanium (Ti-6Al-4V) Blocks Deposited by Wire-Feed Additive Layer Manufacturing (ALM)", *Mat. Sci. Eng. A*, 2012, vol. 532, pp. 295-307.

[18] T. Hua, C. Jing, Z. Fengying, L. Xin, and H. Wiedong, "Microstructure and Mechanical Properties of Laser Solid Formed Ti-6Al-4V from Blended Elemental Powders", *Rare Metal Mat. Eng.,* 2009, vol. 38, no. 4, pp. 574-578.

[19] J. Sieniawski, W. Ziaja, K. Kubiak, and M. Motyka, "Microstructure and Mechanical Properties of High Strength Two-Phase Titanium Alloys", *Titanium Alloys – Advances in Properties Control*, InTech, 2013, pp. 71-80.

[20] S.H. Mok, G. Bi, J. Folkes, I. Pashby, and J. Segal, "Deposition of Ti-6Al-4V Using a High Power Diode Laser and Wire, Part II; Investigation on the Mechanical Properties", *Surf. Coat. Tech.*, 2008, vol. 202, pp. 4613-4619.

[21] M. Koike, P. Greer, K. Owen, G. Lilly, L.E. Murr, S.M. Gayton, E. Martinez, and T. Okabe, "Evaluation of Titanium Alloys Fabricated Using Rapid Prototyping Technologies – Electron Beam Melting and Laser Beam Melting", *Materials,* 2011, vol. 4, pp. 1776-1792.

[22] "ASM Specialty Handbook: Stainless Steels", J.R. Davis ed., 1994, ASM International, Materials Park, OH.

[23] "Stainless Steels for Design Engineers", M. F. McGuire, 2008, ASM International, Materials Park, OH.

[24] “Titanium Alloy Guide”, 2000, RTI International Metals, Inc., Pittsburgh, PA.

[25] G.P. Dinda, A.K. Dasgupta, and J. Mazumder, “Laser Aided Direct Metal Deposition of Inconel 625 Superalloy: Microstructural Evolution and Thermal Stability”, *Mater. Sci. Eng. A*, 2009, vol. 509, pp. 98-104.

[26] S. Gao, Y. Zhou, and M. Xi, “Investigation on Inconel 625 Alloy Thin-Walled Parts by Direct Laser Fabrication”, *Adv. Mater.*, 2011, vols. 189-193, pp. 3687-3691.

[27] H. Qi, M. Azer, and A. Deal, “Studies of Microtexture and Its Effect on Tensile and High-Cycle Fatigue Properties of Laser-Powder-Deposited Inconel 718”, *Metall. Mater. Trans. A*, 2012.

[28] F. Liu, X. Lin, H. Leng, J. Cao, Q. Liu, C. Huang, and W. Huang, “Microstructural Changes in a Laser Solid Forming Inconel 718 Superalloy Thin Wall in the Deposition Direction”, *Opt. Laser Technol.*, 2013, vol. 45, pp. 330-335.

[29] “ASM Specialty Handbook: Nickel, Cobalt, and Their Alloys”, J.R. Davis ed., 2000, ASM International, Materials Park, OH.

[30] R.S. Milller, G. Cao, and M. Grujicic, “Monte Carlo Simulation of Three-Dimensional Non-isothermal Grain-Microstructure Evolution: Application to LENS Rapid Fabrication”, *J. Mater. Synth. Proces.*, 2001, vol. 9, no. 6, pp. 329-345.

[31] M. Morhac and E. Morhacova, “Monte Carlo Simulations of Grain Growth in Polycrystalline Materials Using Potts Model”, *Applications of Monte Carlo Method in Science and Engineering*, InTech, 2011, pp. 563-580.

[32] A.D. Rollett and P. Manohar, “The Monte Carlo Method”, *Continuum Scale Simulation of Engineering Materials: Fundamentals – Microstructures – Process Applications*, compiled by D. Raabe, F. Roters, F. Barlat, and L.Q. Chen, John Wiley & Sons, Inc., 2004, part 4, pp. 76-113.

[33] J. Gruber, H.M. Miller, T.D. Hoffmann, G.S. Rohrer, and A.D. Rollett, “Misorientation Texture Development During Grain Growth. Part I: Simulation and Experiment”, *Acta. Mater.*, 2009, vol. 57, pp. 6102-6112.

[34] E.A. Holm, D.J. Srolovitz, and J.W. Cahn, “Microstructural Evolution in Two-Dimensional Two-Phase Polycrystals”, *Acta. Metall. Mater.*, 1993, vol. 41, no. 4, pp. 1119-1136.

[35] Y.G. Zheng, C. Lu, Y.W. Mai, Y.X. Gu, H.W. Zhang, and Z. Chen, “Monte Carlo Simulation of Grain Growth in Two-Phase Nanocrystalline Materials”, *Appl. Phys. Lett.*, 2006, vol. 88.

[36] Bimal K. Kad, Scott E. Schoenfeld, Matthew S. Burkins, “Through thickness dynamic impact response in textured Ti–6Al–4V plates”, *Mater. Sci. Eng. A*, 2002, vol. 322, no. 1-2, pp. 241-251.

[37] C. Cayron, B. Artaud, L. Briottet, “Reconstruction of parent grains from EBSD data”, *Mater. Charact.*, 2006, vol. 57, no. 4-5, pp. 386-401.

VITA

Rodney M. Clayton was born in Chicago, Illinois in 1989, the son of Michael and Jean Clayton. After completing his work at Plano High School, Plano, Illinois, he entered Monmouth College in Monmouth, Illinois. In May 2011 he completed a Bachelor of Arts in Physics.

In August 2011, he joined Missouri University of Science and Technology to begin work on his Masters in Materials Science & Engineering. While enrolled, he worked as a Graduate Research Assistant in the Laser Aided Manufacturing Processes Laboratory. His research was focused on modeling and the use of metallic powders in the laser deposition process. He completed the requirements for his degree in December 2013 and is now employed with Boardwalk Pipeline Partners, MLP, Houston, Texas as a Metallurgist.